Surface plasmons and hot electrons imaging with femtosecond pump-probe thermoreflectance

Olga Lozan

université de BORDEAUX

THÈSE PRÉSENTÉE

POUR OBTENIR LE GRADE DE

DOCTEUR DE

L'UNIVERSITÉ DE BORDEAUX

ÉCOLE DOCTORALE DES SCIENCES PHYSIQUES ET DE L'INGÉNIEUR

SPÉCIALITÉ: **Lasers, Matière et Nanosciences**

par **Olga Lozan**

Surface Plasmons and Hot Electrons Imaging with Femtosecond Pump-Probe Thermoreflectance

Sous la direction de : M. Stefan DILHAIRE

Soutenue le 26 Février 2015 devant le jury composé de:

M.	Fabrice VALLÉE	Directeur de recherche, Université Claude Bernard Lyon 1	Rapporteur
M.	Alexandre BOUHELIER	Directeur de recherche, Université de Bourgogne	Rapporteur
M.	Philippe LALANNE	Directeur de recherche, Université de Bordeaux	Examinateur
M.	Philippe BEN-ABDALLAH	Directeur de recherche, Université Paris-Sud	Examinateur
M.	Yannick DE WILDE	Directeur de recherche, Institut Langevin	Président
M.	Derryck T. REID	Professeur, Heriot-Watt University	Examinateur
M.	Stefan DILHAIRE	Professeur, Université de Bordeaux	Dir. de thèse

Thèse préparée à l'Université de Bordeaux
au Laboratoire Ondes et Matière d'Aquitaine (LOMA), UMR5798,
351 cours de la Libération, 33405 Talence cedex.

Surface plasmons and hot electrons imaging with femtosecond pump-probe thermoreflectance

Abstract

In this work we explored the ultrafast dynamics of photo-excited hot electrons in plasmonic structures. The particular interest of this field resides on the fact surface plasmons (SP), because of their unrivaled temporal and spatial characteristics, provide a technological route for ultrafast information processes at the nanoscale. In this context, this manuscript provides a comprehension and the harnessing of one of the major limitation of the SP-based technologies : absorption losses by Joule heating.

We exploit the fact that the mechanism of plasmon absorption in metals is followed by generation of hot electrons at femtosecond time scale, thus losses can be seen as a plasmon-to-hot-electron energy conversion. This energy conversion is measured with femtosecond pump-probe technique. Femtosecond SP pulses are launched and probed over hundred femtoseconds through the permittivity variations induced by the hot-electron gas and which accompany the SP propagation. The measured electron temperature profile is therefore an image of plasmon power density distribution (absorption) not broadened spatially and temporally by energy carrier diffusion.

As an important result we demonstrated the capability to link the electronic temperature measurement to the plasmonic absorption, revealing an anomalous light absorption for a sub-λ slit surroundings, in quantitative agreement with predictions of the power density distribution. In a second part we studied plasmon losses and their characteristics when they propagate on semi-infinite metal film. We determined the electronic thermal wave velocity and damping. In the last part we used a focusing taper-structure to adiabatically guide and focus the plasmon at the apex. Was demonstrated the generation of a nanoscale hot spot and put in evidence a delayed electron heating at the taper apex. Perspectives and the remaining open questions are also discussed.

Keywords : plasmonics, nanophotonics, surface plasmon polaritons, hot electrons, femtosecond pump-probe, absorption, electron temperature, nanofocusing.

Imagerie de plasmons de surface et d'électrons chauds par thermoréflectance pompe-sonde femtoseconde

Résumé

Ce travail est consacré à l'étude de la dynamique ultrarapide d'électrons chauds photo-excité dans des structures plasmonique. L'intérêt particulier de ce domaine réside dans le fait que les SPs, en raison de leurs caractéristiques spatio-temporelles spécifique, offrent un nouvel attrait technologique pour les processus de transport d'information ultra-rapide aux nano-échelles. Dans ce contexte, ce manuscrit offre une compréhension et une exploitation de l'une des principales limitations des technologies à base de SP : les pertes par effet Joule. Nous exploitons le fait que le mécanisme d'absorption des plasmons dans les métaux est suivi par la génération d'électrons chauds à l'échelle femtoseconde, ainsi les pertes peuvent être considrées comme une conversion d'énergie plasmon-électrons chauds. Cette conversion d'énergie est mesurée à l'aide d'une technique pompe-sonde laser femtoseconde. Nous lançons des impulsions SP que nous sondons sur des centaines de femtosecondes grace aux variations de permittivité diélectrique induites par le gaz d'électrons chaud accompagnant la propagation de SP. Le profil de température électronique est par conséquent une image de la distribution de densité de puissance de plasmon (absorption) non élargi spatialement et temporellement par diffusion de porteurs d'énergie. Nous avons pu démontrér la capacité de relier la mesure de temperature électronique à l'absorption du SP, révélant une absorption anormale autour d'une fente nanometrique. Les résultats expérimentaux sont en accord quantitatif avec les prédictions théoriques de la distribution de densité de puissance. Dans une seconde partie, nous avonsétudié les pertes plasmoniques et leurs caractéristiques lors de sa propagation sur un film métallique semi-infini. Nous avons détermineé la vitesse de l'onde thermique électronique et son atténuation. Dans la dernière partie, nous utilisons une structure en pointe pour guider adiabatiquement et focaliser le plasmon à l'extrémité. Nous avons démontré ainsi la génération d'un point chaud nanométrique et avons mis en évidence un retard dans l'échauffement des électrons à l'extrémité de la pointe. Les perspectives et les questions ouvertes sont également discutées.

Mots clé : plasmonique, nanophotonique, plasmon polariton de surface, électrons chaud, pompe-sonde femtoseconde, absorption, température électronique, nano-focalisation.

Acknowledgement

Three years back the professor and lecturer in the Applied Physics Departments at Moldova State University Cirlig Sergiu inspired me to embark on this amazing "journey" from Moldova to France, towards my PhD degree. And I accepted the challenge. During this long and eventful journey I benefited from the guidance, support and sincere effort of many people and I want to take advantage of this opportunity to thank these persons in writing.

First of all, I would like to thank the jury members Fabrice Vallée, Alexandre Bouhelier, Philippe Ben-Abdallah, Yannick De Wilde, Derryck T.Reid and Philippe Lalanne for accepting to be in my committee. I appreciate the valuable time they have spent for reading carefully the thesis manuscript. Especially I thank both the referees (Alexandre Bouhelier and Fabrice Vallée) for reviewing my thesis and writing reports.

I am deeply grateful to my supervisor Stefan Dilhaire for his guidance, support, encouragement, and belief in me over the past three years. He has provided guidance at crucial moments of my work while also allowing me to work independently most of the time. He has as well taught me how to speak to be heard, to present science to be understood. In his lab I had the opportunity to work with the leading edge experimental equipment and to develop skills and competences in using them. Furthermore I would like to express my gratitude also to Philippe Lalanne, the collaboration with him brought the main results of my thesis. His innovative ideas and constructive criticisms have considerably propelled my work and I was as well greatly inspired by his dedication to research. Both Stefan and Philippe played a vital role in guiding me along the way, following my progress, listening my ideas and providing feedback.

I would also like to thank our collaborators who contributed considerably to this work, namely Mathias Perrin, for providing theoretical model calculations,

and Buntha Ea-Kim for sample fabrication respectively.

Thanks are also addressed to all the other group members: Jean-Michel Rampnoux, Stephane Grauby, Wilfrid Claeys, Gilles Pernot, Quentin D'Acremont and ex-student of the group Calbris Gaëtan for their ideas, advice, support and companionship. Especially Gaëtan, whom I have disturbed many times at the beginning of my PhD with experiment-related problems. He was always distantly helping me out with all my difficulties.

I would also like to mention my friends Alexandru and Iana, Sam, Marion, Bin, Alex, Charles, Arghya, with whom I shared many pleasant moments here in Bordeaux. I am extremely grateful to have met Chiara as I found a very good friend in her. I am also lucky to have shared the office during the last three years with Bryan Kuropatwa. All this time I benefited from his good humor, wise advice, green plants in the office and genuine maple syrup.

Finally, I would like to thank my parents and Dima for always being there for me. This thesis would be impossible without their understanding, support, and sacrifice over the years...

Olga Lozan
Université de Bordeaux
February, 2015

Résumé

Le domaine de la plasmonique comprend la science et l'ingénierie de l'interaction optique avec des nanostructures. La possibilité d'obtenir l'augmentation et le confinement de champs optiques à l'échelle nanométrique, près des nano-objets conçus à propos, a été le moteur, au cours des dernières années, pour l'étude approfondie d'une grande variété de phénomènes plasmoniques. Suite à ces études, le domaine riche et dynamique de la plasmonique couvre maintenant différentes disciplines, ce qui suggère des applications émergentes dans la chimie, la science des matériaux, la biologie, la médecine et l'ingénierie.

La plasmonique concerne l'étude de l'interaction entre le champ électromagnétique et les électrons dans un métal. Les électrons libres dans les métaux peuvent être excités par la composante électrique de la lumière. Il en résulte des oscillations collectives des électrons, qu'on appelle plasmons. Toutefois, en raison de la dissipation ohmique, les pertes dans l'oscillation de plasmon sont inévitables, ce qui représente un facteur limitant pour la plupart des dispositifs plasmoniques. D'autre part, l'absorption de la lumière peut être renforcée considérablement dans le métal par des motifs métalliques bien conçus pour l'excitation des plasmons de surface.

L'intérêt particulier de la plasmonique réside dans le fait qu'elle représente le lien entre deux échelles de longueur différentes, permettant le confinement de la lumière dans des régions plus petites que la limite de diffraction. Un facteur limitant important pour le développement et la mise en œuvre des dispositifs plasmoniques est représenté par les pertes subies par les plasmons. Ainsi, l'objectif de cette thèse a été de mesurer ces pertes dans des surfaces métalliques ou des dispositifs plasmoniques plus petits que la longueur d'onde de la lumière. La décroissance initiale des plasmons de surface dans les métaux se produit principalement par déphasage, ce qui conduit à la décroissance d'un plasmon de surface en gaz d'électrons libres. Ce processus rapide, qui est principalement respons-

able de la décohérence des oscillations collectives des électrons, empêche une augmentation importante du champ local et limite la durée de vie des plasmons à quelques dizaines de femtosecondes, selon le métalet la gammespectrale.

La mesure de la chaleur dissipée dans les structures plasmoniques est d'une importance primordiale, mais représente également une tâche ardue. En effet, les techniques à haute résolution spatiale utilisées pour mesurer la chaleur dissipée par les plasmons révèlent un profil temporal et spatial de la source de chaleur locale qui est élargi en raison de la diffusion (du transport) des phonons dans le métal.

L'absorption de l'énergie des plasmons dans les métaux est médiée par les électrons chauds. Les plasmons de surface et les électrons chauds interagissent dans les métaux dans des temps de quelques dizaines de femtosecondes. Il est ainsi possible de détecter, à l'échelle de la femtoseconde, les variations de température électronique suite à la propagation des plasmons. A cette échelle de temps tous les processus de diffusion (des électrons et des phonons) n'ont pas encore commencé et peuvent donc être négligés. Par conséquent, le profil de température est l'image parfaite de la distribution de densité de puissance (d'absorption) induite par les pertes plasmoniques.

Dans cette thèse, nous avons proposé l'utilisation d'une technique pompe-sonde femtoseconde, capable de mesurer la variation de la température électronique avec une résolution temporelle de la femtoseconde. Les pertes peuvent être interprétées comme le résultat de la conversion de l'énergie plasmonique en électrons chauds. Cette conversion d'énergie est mesurée en lançant des impulsions femtosecondes de plasmons de surface et en mesurant les variations de la permittivité induites par le gaz d'électrons chauds. Ces variations, qui sont enregistrées pendant quelques centaines de femtosecondes après que le plasmon a été lancé, révèlent l'image de la source de chaleur locale avec un faible élargissement.

D'abord, nous avons démontré la capacité de relier la mesure de la température électronique à l'absorption des plasmons sur un objet canonique. Ce dernier est une fente nanométrique unique éclairée par l'impulsion pompe qui est utilisée pour lancer les plasmons. Les résultats que nous avons obtenus sur un tel objet sont en parfait accord avec les prédictions de la distribution de la densité de puissance à proximité d'une fente unique. Ces résultats révèlent un profil d'absorption de lumière anormale. C'est la première fois, à notre connaissance,

que la densité de puissance plasmonique est mesurée dans des surfaces métalliques nanométriques.

Cependant, les fentes uniques montrent une faible efficacité de génération des plasmons. Afin d'étudier les pertes des plasmons et leurs caractéristiques lorsqu'ils se propagent dans des films métalliques semi-infinis, nous avons alors opté pour des réseaux métalliques nanométriques comme lanceurs des plasmons, ce qui nous a permis d'obtenir un meilleur rapport signal à bruit. Nous avons été capables de mesurer la vitesse de l'onde thermique électronique et son amortissement. Cet amortissement a pu être observé à travers la réponse transitoire électronique dans les premières centaines des femtosecondes. Nous avons démontré pour la première fois qu'il est possible d'imager et de filmer la propagation des plasmons à un taux de 25 Tera images par seconde grâce aux électrons chauds générés par les pertes plasmoniques.

Dans la dernière partie de ce travail de thèse, nous avons utilisé un réseau pour lancer les plasmons dans une structure métallique en pointe. Les plasmons sont ensuite guidés de manière adiabatique et focalisés à l'extrémité de la pointe. Nous avons suivi la propagation des plasmons par la mesure des pertes point par point et nous avons imagé le processus de focalisation des plasmons.

Ce mémoire s'articule en cinq chapitres. Nous commençons par rappeler, dans le premier chapitre, les propriétés des plasmons de surface et des électrons chauds. Nous expliquons également de manière détaillée comment les variations de température des électrons chauds dans les métaux nobles peuvent causer un changement de la réflectivité optique.

Dans le chapitre 2 nous décrivons la méthode thermoréflectance pompe-sonde appliquée à la mesure de la température électronique à l'échelle de la femtoseconde, ainsi que le montage expérimental employé tout au long de cette thèse.

Le chapitre 3 est consacré à la description de l'absorption des plasmons de surface à proximité des fentes uniques nanometriques dans des films métalliques.

Le chapitre 4 aborde l'évaluation de la longueur de propagation et de la vitesse de groupe des plasmons de surface. L'étude de la dynamique des électrons chauds excités par des plasmons propagatifs dans un film métallique semi-infini est aussi présentée.

Le dernier chapitre traite le processus de nano-focalisation adiabatique des plasmons avec un guide métallique en pointe. On y démontre la génération d'un

point chaud à l'extrémité de la pointe. La thermalisation interne plus lente des électrons dans la région du point chaud, qui a été mise en évidence lors de cette étude, est attribuée à une réduction de la vitesse de groupe des plasmons de surface.

Contents

Introduction

The field of plasmonics encompasses the science and engineering of optical interaction with nanostructures. Prospects of subwavelength confinement and enhancement of optical fields near properly designed nanoscale objects has been a motivation to extensively investigate a variety of plasmonic optical phenomena in recent years. As a result of these investigations, the dynamic and vibrant field of plasmonics now spans various disciplines, suggesting exciting applications in chemistry, materials science, biology, medicine, and engineering.

Plasmonics concerns the study of the interaction between electromagnetic field and the electrons in a metal. Free electrons in metals can be excited by the electric component of light to have collective oscillations. However, due to the Ohmic dissipation, losses are inevitable for the plasmon oscillation, which is usually detrimental to most plasmonic devices. Meanwhile, the absorption of light can be enhanced greatly in the metal by properly designed metal patterns for surface plasmons excitation.

The particular interest in this field resides on the fact that plasmonics builds a bridge between two different length scales by confining light in subwavelength regions. For the further development and implementation of plasmonic devices, an important limiting factor are the losses which the plasmon undergoes. Thus, the focus of this thesis is to measure these losses in metallic sub-wavelength surfaces (or plasmonic devices), this work was performed in close collaboration with the group of Philippe Lalanne at LP2N (IOGS).

The initial decay of surface plasmons in metals occurs mainly via dephasing, which leads to the decay of a surface plasmon into free electron gas. It is this rapid process that is primarily responsible for the decoherence of the collective electron oscillations, prevents the realization of drastic local field enhancements and limits the plasmonic lifetimes to a few tens of femtoseconds, depending on the metal and spectral range.

The measurement of the heat dissipated in plasmonic structures is of fundamental importance, but it is also a daunting task. The existent high-resolution techniques for measuring the dissipated plasmon heat [1] reveal a temporally- and spatially-broadened profile of the local heat source because of the phonon diffusion transport in the metal. The mechanism of plasmon energy absorption in metals is mediated by hot electrons. The surface plasmons and hot electrons interact in metals over a time scale of a few tens of femtoseconds. In this time range, we detect electronic temperature variation accompanying the plasmon propagation. In such a time scale all diffusion processes (electrons and phonons) have not started yet and can be neglected. The temperature profile is therefore the perfect image of the power density distribution (absorption) induced by the plasmon losses.

In this thesis we propose to take advantage of femtosecond pump-probe technique, capable of measuring electronic temperature variation with femtosecond time resolution. Losses can be seen as a plasmon-to-hot-electron energy conversion. This energy conversion is measured by launching femtosecond surface plasmon pulses and by probing the permittivity variations induced by the hot-electron gas. The variations are recorded over few hundred femtoseconds after the plasmon was launched. They reveal the image of the local heating source with a weak broadening.

We first demonstrate the capability to relate the electronic temperature measurement to the plasmonic absorption on a canonical object. This later is a single slit shined by a pump pulse used to launch plasmons. Our measurement where in excellent agreement with predictions of the power density distribution in the slit surroundings, revealing an anomalous light absorption [2]. It was the first time, to our knowledge, that plasmonic power density was revealed in sub-wavelength metal surfaces.

Single slits, however, still showed very poor efficiency for plasmon launching. Thus, we employed gratings as plasmon-launchers, to improve the signal to noise ratio, to study plasmon losses and their characteristics when they propagate in semi-infinite metal films. We demonstrate we were able to determine the electronic thermal wave velocity and damping. We observed this damping through the electronic transient response in the very first hundred femtoseconds. We demonstrated the capability to image and to film the plasmon propagation at

a rate of 25 Tera image per second thanks to the hot electrons excited by plasmonic losses. In the last part we used a grating to launch a plasmon in a focusing metallic structure. The plasmon was then adiabatically guided and focused at the end of a taper-structure. We followed the propagation measuring the losses point by point and imaging the focusing.

The thesis is organised as follows. The first chapter presents a short overview of both surface plasmons and hot electrons properties. We also present a detailed explanation of how the hot electron temperature dynamics in noble metals can cause the change of optical reflectivity. Chapter 2 describes the thermoreflectance pump-probe method applied to electronic temperature measurement at femtosecond time scale, as well as the general experimental set-up employed throughout this thesis. Chapter 3 reveals the surface plasmon absorption around subwavelength structures in metal films. Chapter 4 concerns the evaluation of surface plasmon propagation length, group velocity and a study of the plasmon-excited hot electrons dynamics in free space propagation. The last chapter deals with adiabatic plasmon nanofocusing with a laterally tapered metal waveguide. Is demonstrated the generation of a hot spot at the taper apex. A slower electron thermalization process in the hot spot region is revealed, which is associated with surface plasmon group velocity reduction.

CHAPTER 1

Plasmons and hot electrons

It is still a challenge to measure the plasmon-induced heating in metals. We have chosen to measure this heating in metallic media thanks to their dissipation, which cause strong electronic temperature variation at femtosecond time scale.

As we always use a laser pulse for plasmon generation and a second pulse for temperature measurement, we first start by describing both physical properties dealing with plasmonic excitation and electronic properties allowing us temperature measurement with thermoreflectance.

We start by presenting plasmons, we specially focus on surface plasmon properties related to the coupling of an electromagnetic wave and an electron gaz. We detect plasmons through the temperature rise accompanying their dissipation. For that we describe electronic properties of noble metals enabling electronic temperature measurement by reflectivity changes. Thus we introduce the notion of hot electrons, when these later (excited by a plasmon wave) are in equilibrium with the rest of the gas but not with the lattice. The use of a two temperature model illustrate the different characteristic time involved in the relaxation processes

Contents

1.1 Introduction

People have been captivated by the glow of shiny metals since ancient times. Gold and silver were valued by many cultures and used for ornaments, jewelry, and the production of coins. Polished silver surfaces were also used as mirrors while gold was used to make stained glass, most famously known for the windows of many cathedrals in Europe and, much earlier, as the base glass of the well-known Lycurgus cup [3]. An understanding of the physics behind these phenomena came much later, in the 19th and 20th centuries, when scientists came up with a theoretical description of the optics of metals and attributed these unique properties to *plasmons*.

Surface plasmons (SP) are collective oscillation of surface charges on a metal surface, and are classified into two types, localized surface plasmons (LSP) and surface plasmon polaritons (SPP). The LSP are localized in narrow volumes of nano-structures or particles, and SPP are transverse magnetic (TM) mode electromagnetic wave propagating at a metal/dielectric interface, which is evanescently confined in the perpendicular direction [4]. The unique properties of surface plasmons, which will be discussed in this chapter, has rapidly attracted the interest of the scientific community. SPs can produce strong electromagnetic field at a localized area and are utilized for bio-sensors [5] and solar cells [6]. SPP can be confined into a narrow area beyond the diffraction limit of light and has potential applications in optical circuits and optical computing. The recently developed field, *Plasmonics* [7–9], is rapidly growing and is mostly concerned with the control of optical radiation on the subwavelength scale.

Throughout this work, we employ the pump-probe thermoreflectance method to measure the plasmon absorption and the induced temperature increase of the *hot electrons*. Since the dielectric function ϵ is the quantity which links the microscopic physics of electronic transitions in the metal with the macroscopically observable optical reflectivity, we will focus in this chapter on understanding the notion of *hot electrons*, and how a change due to electron dynamics in the sample can cause a change in reflectivity.

1.2 Physics of Plasmons

1.2.1 Basic properties of metals. Volume plasmons

Since most of the physics regarding the interaction of light with metal structures is hidden in the frequency dependence of the metal complex permittivity, we will next discuss the microscopic origin of the dielectric permittivity and the subsequent fundamental optical properties of metals. One of the most simple, but nevertheless very useful models to describe the response of metals exposed to an electromagnetic field was proposed by Paul Drude [10,11] at the beginning of the 20th century [1].

In the so-called free-electron model, Drude assumed a metal to be described as a collection of ions, that are fixed in space, and a gas of free conduction electrons that interact with themselves and with the ions through the Coulomb force. The interacting system of ions and electrons is basically a plasma where the ions are much more inert than the electrons. When the plasma interacts with an electromagnetic field, the electrons execute a forced oscillation relative to the ions. The amplitude and phase of the longitudinal density fluctuations -***plasma oscillations***- relative to that of the driving electromagnetic field, depends on the frequency of the electromagnetic field relative to the eigen oscillation frequency of the plasma, the so-called *plasma frequency* ω_p:

$$\omega_p^2 = \frac{ne^2}{\epsilon_0 m_{\text{eff}}}, \tag{1.1}$$

which follows directly from a simple harmonic oscillator description of the response of the electrons [7]. Here n is the electron density, e and m_{eff} are the charge and effective mass of the electron. The quantum of this oscillation is called a ***plasmon***, or, since the electrons are oscillating in the metal volume, a bulk or ***volume plasmon***. For gold and silver[2], $\omega_p \approx 10^{16}$ rad/s.

[1] Drude's model was further extended by Hendrik Lorentz five years later. In 1933 Arnold Sommerfeld and Hans Bethe expanded the classical Lorentz-Drude model and eliminated some problems in the description by accounting for the Pauli principle of quantum mechanics and replacing the Maxwell-Boltzmann with the Fermi-Dirac distribution (consult [12] for more details).

[2] The specific value of ω_p for most metals lies in the ultraviolet region, which is the reason why they are shiny and glittering in the visible spectrum

The plasma oscillation is damped, for instance, due to the scattering of the electrons on impurities, lattice defects, etc. Phenomenologically, this is taken into account by introducing a damping constant γ, and in the Drude model the relative dielectric function is expressed as:

$$\epsilon_{Drude}(\omega) = 1 - \frac{\omega_p^2}{\omega(\omega + i\gamma)}. \tag{1.2}$$

Regarding the above equation, it is insightful to study some limiting cases. In particular, if we neglect the damping of the plasma oscillations γ for the moment, the Drude dielectric function simplifies to:

$$\epsilon_{Drude}(\omega) = 1 - \frac{\omega_p^2}{\omega^2}, \tag{1.3}$$

and we can distinguish two frequency regions:

- If ω is smaller than ω_p, ϵ_{Drude} becomes negative and the refractive index $n = \sqrt{\epsilon}_{Drude}$ is imaginary. An imaginary refractive index implies that an electromagnetic wave cannot propagate inside the medium. A light wave with $\omega < \omega_p$ is thus reflected, because the electrons in the metal screen the light.

- If ω is larger than ω_p, ϵ_{Drude} is positive and the corresponding refractive index $n = \sqrt{\epsilon_{Drude}}$ is a real quantity, which implies that the light wave gets transmitted (the metal becomes transparent). This can be also interpreted by considering that for $\omega > \omega_p$, the electrons in the metal are too slow and cannot respond fast enough to screen the field. Consequently, volume plasmons can be excited and propagate through the metal volume.

Over a wide frequency range (from the infrared (IR) region to the visible), the Drude model and this treatment of a free conduction electron gas may give quite accurate results for the optical properties of noble metals. But in the ultraviolet (UV)-visible range, since higher-energy photons are employed, *interband transitions* can take place, where bound electrons from lower lying bands can also be promoted to the conduction band [8, 13]. Thus, in this case, the Drude model becomes inaccurate for the visible regime as indicated in Fig. 1.1. In this figure, dielectric permittivities calculated under the Drude model are presented

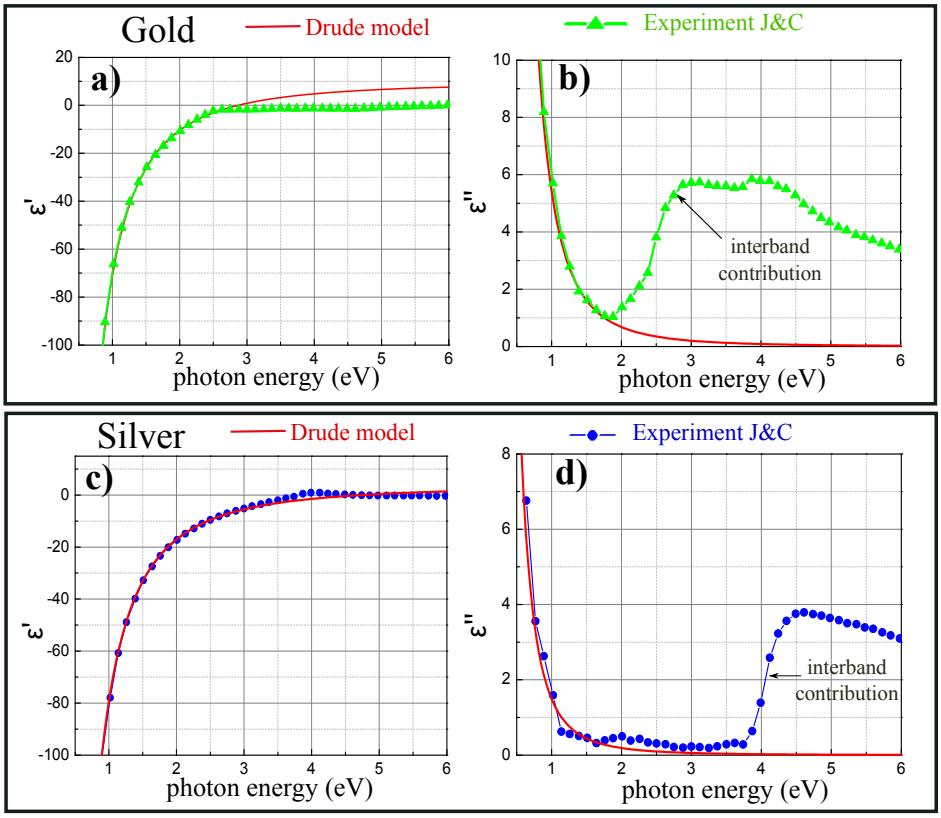

Figure 1.1: *Dielectric function of gold and silver: Experimental values versus model.* ***(a)-(b)*** *Real and imaginary part of dielectric function of gold. Experimental data-green triangles- taken from [14], compared to calculated values (red line) using the quasi-free electron or Drude model with the Au parameters:* ω_p = 9 eV, γ = 67 meV, ϵ_∞ = 9.84. ***(c)-(d)****Real and imaginary part of dielectric function of silver. Experimental data (blue circles) compared to Drude model (red line) for the Ag parameters:* ω_p = 9.1 eV, γ = 18 meV, ϵ_∞ = 3.7*, see also [15].*

for two representative metals Au and Ag, and in particular, compared with those obtained experimentally by Johnson and Christy [14]. Regarding the calculated Drude-dielectric permittivity in Fig. 1.1, a constant offset ϵ_∞ to Eq. (1.2) has been introduced, which accounts for the integrated effect of all higher energy interband transitions not considered in the present model. While the real part $\epsilon'(\omega)$ reproduce well the Drude model curve, the imaginary part $\epsilon''(\omega)$ shows some discrepancies between theory and experiment, which originate from supplementary excited bound electrons (interband contribution). These interband electron transitions will be discussed in detail in a later section.

Also from Fig. 1.1 we can conclude that from IR to visible spectral regime the real part of the dielectric function is negative $\epsilon'(\omega) < 0$ and the incident electromagnetic radiation is back reflected by the plasma, penetrating into the metal only over a distance of the order of the skin depth, which is about 20 nm for gold at $\lambda = 0.8\,\mu$m. In the UV range, i.e., above the plasma frequency, $\epsilon'(\omega)$ is positive and the metal is transparent for incident electromagnetic radiation.

1.2.2 Electromagnetic waves at interfaces: Surface plasmons

1.2.2.1 What is a surface plasmon?

In 1957, Ritchie [16] theoretically showed that, when a metal is in the form of a thin film, a second type of plasma resonance can occur at $\omega = \omega_p/\sqrt{2}$. Here the charge oscillations take place at the top and bottom *interfaces* of the metal film. This prediction was confirmed in an experiment by Powell and Swan [17]. These collective oscillations of the electron gas on the interface between a metal[3] and a dielectric are known as the ***surface plasmons*** (SPs). Theoretically, surface plasmons simply arise as a purely 2D solution of Maxwell's equations that propagate as a *transverse magnetic wave* along the metal-dielectric interface. As a result, SPs have mixed electromagnetic-wave and surface-charge character, as illustrated in Fig. 1.2(a).

1.2.2.2 Surface plasmon dispersion

In order to understand the physical properties of SPs we have to apply Maxwell's equations to the flat interface between a metal and a dielectric and obtain the SP dispersion relation. The dispersion of the surface plasmon, i.e., the dependence of the SP frequency ω on its wave number k_{SP} shows how the properties of the surface plasmon change in various frequency ranges, and determines the value of both the phase and group velocities.

By following Ref. [7], we consider a planar interface between two media. We choose the interface to coincide with the plane $z = 0$ of a Cartesian coordinate

[3] It has also been shown [18, 19] that also doped graphene may serve as an unique two-dimensional plasmonic material with certain advantages compared to metals (lower losses and much longer plasmon lifetimes).

system (see Fig. 1.2(a)). One medium, the metal, is characterized by a general complex frequency-dependent dielectric function $\epsilon_1(\omega) = \epsilon_m$ at $z < 0$, whereas the dielectric function of the other medium (dielectric) $\epsilon_2(\omega) = \epsilon_d$ for the dielectric at $z > 0$ is assumed to be real.

We are looking for homogeneous[4] solutions of Maxwell's equations that are localized at the interface. Mathematically, it is the solution of the wave equation:

$$\nabla \times \nabla \times \mathbf{E}(\mathbf{r},\omega) - \frac{\omega^2}{c^2}\epsilon(\mathbf{r},\omega)\mathbf{E}(\mathbf{r},\omega) = 0, \tag{1.4}$$

with $\epsilon(\mathbf{r},\omega) = \epsilon_1(\omega)$ for $z < 0$ and $\epsilon(\mathbf{r},\omega) = \epsilon_2(\omega)$ for $z > 0$. The wave equation now has to be solved separately in each region of constant ϵ and the corresponding boundary conditions tell us how to match the two solutions at the interface. In general, Maxwell's equations allow two sets of self-consistent solutions with different polarizations: **TM** (transverse magnetic or p-polarized) and **TE** (transverse electric or s-polarized) modes. However, it is sufficient to consider only TM-polarized waves in both media because *no solution exists for the case of TE-polarization* (see Ref. [8] for example). Therefore, we neglect TE modes and write down the solution of Eq. (1.4) for the TM waves as:

$$\mathbf{E}_j = \begin{pmatrix} E_{x_j} \\ 0 \\ E_{z_j} \end{pmatrix} e^{ik_x x - i\omega t} e^{ik_{z_j} z}, \tag{1.5}$$

where $j \in \{1,2\}$ denotes the two media. The component k_x of the wave vector parallel to the interface is conserved, thus the index j indicating the medium is unnecessary there and we obtain the following relation which holds for the wave vector components:

$$k_x^2 + k_{z_j}^2 = \epsilon_j k^2, \;\; j \in \{1,2\}. \tag{1.6}$$

Here $k = 2\pi/\lambda$, with λ being the vacuum wavelength. Exploiting the fact that the displacement fields in both half spaces have to be source free, i.e., $\nabla \cdot \mathbf{D} = 0$ (Gauss' law), leads to:

$$k_x E_{x_j} + k_{z_j} E_{z_j} = 0, \;\; j \in \{1,2\}. \tag{1.7}$$

[4] A homogeneous solution is an eigenmode of the system, i.e., a solution that exists without external excitation.

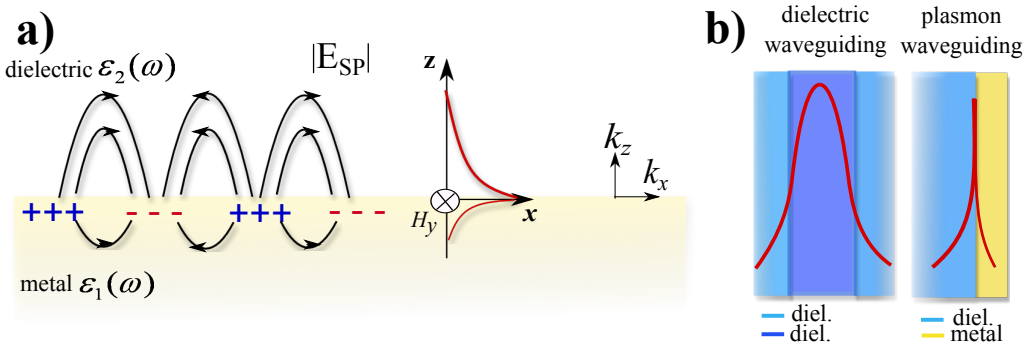

Figure 1.2: ***(a)*** *Schematic representation of the charges and the electromagnetic field of SPs propagating on a surface in the* ***x*** *direction. On the right is shown the exponential dependence of the field E_z. The magnetic field is represented by H_y, in the* ***y*** *direction, of this TM-polarized wave.* ***(b)*** *In contrast to dielectric waveguides, the SPPs waveguiding is characterized by evanescent fields along both interfaces.*

The above equations Eq. (1.6) and Eq. (1.7) establish conditions that define the fields in each of the two media. However, we still have to match the fields at the interface using boundary conditions, which requires continuity of the parallel component of **E** and the perpendicular component of **D**. These lead to another set of equations which read as:

$$\begin{aligned} E_{x_1} - E_{x_2} &= 0, \\ \epsilon_1 E_{z_1} - \epsilon_2 E_{z_2} &= 0. \end{aligned} \tag{1.8}$$

Equations (1.6), (1.7) and (1.8) form a homogeneous system of four equations for the four unknown field components. This system of equations has a solution if the respective determinant vanishes. This happens either for $k_x = 0$, which does not describe excitations propagating along the interface, or otherwise for:

$$\epsilon_1 k_{z_2} - \epsilon_2 k_{z_1} = 0. \tag{1.9}$$

Combining Eq. (1.6) and Eq. (1.9) we obtain a dispersion relation, i.e., a relation between the wave vector along the propagation direction and the angular frequency ω:

$$k_x^2 = \frac{\epsilon_1 \epsilon_2}{\epsilon_1 + \epsilon_2} k^2 = \frac{\epsilon_1 \epsilon_2}{\epsilon_1 + \epsilon_2} \frac{\omega^2}{c^2}. \tag{1.10}$$

We also obtain an expression for the normal component of the wavevector:

$$k_{z_j}^2 = \frac{\epsilon_j^2}{\epsilon_1 + \epsilon_2} \frac{\omega^2}{c^2}, \; j \in \{1, 2\}. \tag{1.11}$$

The relations Eq. (1.10) and Eq. (1.11) are the central equations which govern most of the surface plasmon properties. Therefore, by analyzing this set of equations, we obtain the conditions which have to be fulfilled for a surface mode to exist. First, we are looking for solutions that are propagating along the surface, i.e., we require a real k_x. Analyzing Eq. (1.10) this can be fulfilled if the sum and the product of the dielectric functions are either both positive or both negative. Second, in order to obtain a "bound" solution, we require that the normal components of the wave vector k_{z_j} should be imaginary in both media, giving rise to exponentially decaying solutions. This can only be achieved if the sum in the denominator of Eq. (1.10) is negative. From this we conclude that the conditions for an interface mode to exist are the following[5]:

$$\begin{aligned} \epsilon_1(\omega)\epsilon_2(\omega) < 0, \\ \epsilon_1(\omega) + \epsilon_2(\omega) < 0, \end{aligned} \tag{1.12}$$

which means that one of the dielectric functions must be negative with an absolute value exceeding that of the other. In other words, the requirement for the interface mode to exist is that the interface should be "active", i.e., the real parts of the dielectric functions $\epsilon'(\omega)$ of the media on either side of the interface have opposite signs. As we have demonstrated in the previous section with Fig. 1.1, metals (especially noble metals such as gold and silver), fulfill this requirement, as they have a large negative real part of the dielectric constant along with a small imaginary part. Therefore, at the interface between a noble metal and a dielectric, such as glass or air, localized modes at the metal-dielectric interface can exist.

The resulting imaginary k_{z_j} corresponds to exponentially decaying (so called *evanescent*) waves. This characteristic nature of the surface plasmons resides in an extreme confinement of fields on both sides, which make them good candidates

[5]For simplicity, we assume that the imaginary parts of the complex dielectric functions are small compared with the real parts such that they may be neglected. A more detailed discussion that justifies this assumption see [7] .

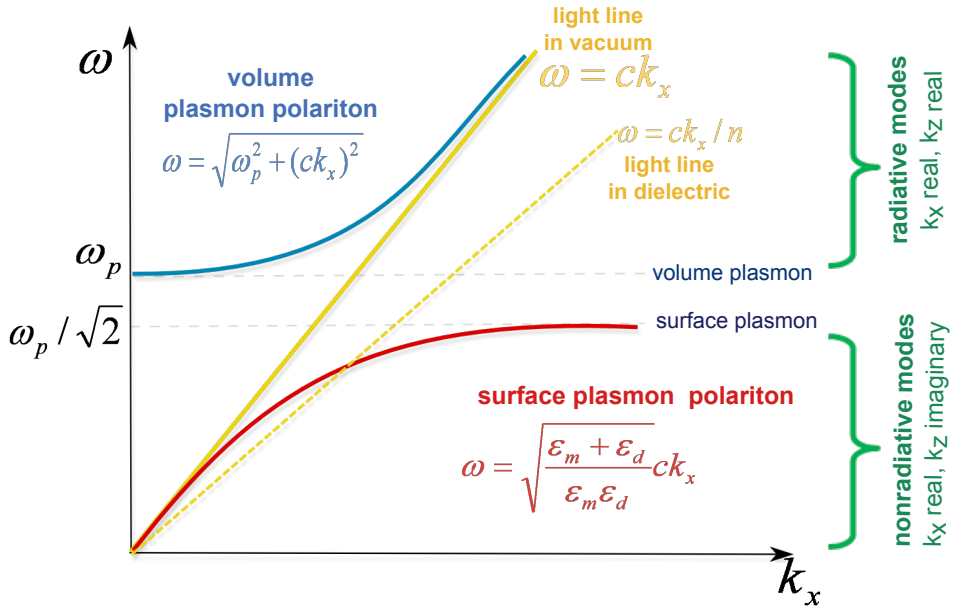

Figure 1.3: *The dispersion relation of nonradiative SPs for a metal/air interface (red line). The solid blue line results from using a Drude-type dielectric function for the case of free electrons, where ω_p is the plasma oscillation frequency. The dotted line at $\omega = \omega_p/\sqrt{2}$ presents the limit when SP becomes a localized excitation. Since the dispersion line of plasmons (red line, without damping; blue line for free electrons) does not cross the light cone (yellow line) at any point, it is not possible to excite a surface plasmon at a metal/air interface with a light wave. However, the light cone can be tilted (dotted yellow line) if we change from free space to a dielectric medium.*

for waveguiding. In contrast to conventional dielectric waveguides [Fig. 1.2(b)], in both the dielectric and the metal SPs are evanescent.

The dispersion relation [Eq. (1.10)] is presented in Fig. 1.3. The solid blue line is the dispersion of free electrons according to the Drude model, while the solid red line represents the dispersion of SPs (without damping). This energy branch corresponds to a true interface wave, the ***surface plasmon polariton*** (SPP). The annex ***polariton*** is used to highlight the intimate coupling between the charge density wave on the metal surface (surface plasmon) with the light field in the dielectric medium (photon). At low frequencies the SP on the metal/vacuum interface has a photon-like nature, i.e., its phase velocity is very close to the speed of light: it extends mainly in the vacuum rather than in the metal. At optical frequencies the dispersion curve $\omega(k_x)$ starts to bend over, which results in a decrease of the SPP group velocity $v_g = \partial\omega/\partial k_x$ and higher damping. In the

limit that $\omega \to \omega_p/\sqrt{2}$ the SPP becomes a localized excitation, since $v_g \to 0$.

Since the red line of the surface plasmon polariton does not cross the light line (solid yellow line) at any point, a direct excitation of surface plasmons with an electromagnetic wave is not possible (the momentum of light is always too small). Nevertheless surface plasmon polaritons can be excited, of course, one just has to provide the missing momentum contribution.

1.2.2.3 Surface plasmon length scales

Surface plasmon polariton wavelength. Using the results of the previous section, we will continue by discussing the characteristic length scales that are important for surface plasmon based photonics. For this we recall that we consider the metal to have a complex dielectric function: $\epsilon_1 = \epsilon_1' + i\epsilon_1''$ while the adjacent dielectric medium has negligible losses, i.e., ϵ_2 is real. We then naturally obtain for Eq. (1.10) a complex parallel wavevector: $k_x = k_x' + ik_x''$. The real part k_x' determines the SPP wavelength, while the imaginary k_x'' accounts for the damping of the SPP as it propagates along the interface. Under the assumption that $|\epsilon_1''| << |\epsilon_1'|$, we obtain the SPP wavelength:

$$\lambda_{\mathrm{SPP}} = \frac{2\pi}{k_x'} \approx \sqrt{\frac{\epsilon_1' + \epsilon_2}{\epsilon_1'\epsilon_2}} \cdot \lambda_0, \tag{1.13}$$

where λ_0 is the wavelength of the excitation light in vacuum. Using $\epsilon_2 = 1$ and the dielectric functions of gold ($\epsilon_1 = -11.6 + 1.2i$) at a wavelength of $\lambda = 633\,\mathrm{nm}$ [14], we obtain $\lambda_{SPP} = 605\,\mathrm{nm}$. As the value of the square root in Eq. (1.13) is always smaller than 1, λ_{SPP} is always slightly less than the free space wavelength λ_0. Again, the fact that $\lambda_{\mathrm{SPP}} < \lambda_0$ reflects the bound nature of SPP modes on a planar surface.

Surface plasmon propagation length. An important property of the surface plasmon is that it is attenuated during propagation basically due to dissipation in the metal - the electrons are inelastically scattered. If a surface plasmon propagates along a smooth surface, its intensity decreases as $e^{-2k_x''x}$ [4], where $k_x = k_x' + ik_x''$. The length $L_{\mathrm{SPP}} = 1/2k_x''$ after which the intensity is reduced to 1/e times its initial value (in the x direction), is defined as the *propagation length.*

For gold and silver, L_{SPP} ranges from millimeters in the mid-infrared range to less than a micron in the blue part of the visible spectrum, and sets the upper limit for the size of any photonic circuit based on SPPs.

We use the previously mentioned data for the dielectric function at $\lambda = 633\,\mathrm{nm}$, to calculate that for the relatively absorbing gold the propagation length of SPPs on a gold/air interface of $L_{\mathrm{SPP}} \approx 10\,\mu\mathrm{m}$. However for the silver, which has lower losses, at the same wavelength ($\epsilon_2 = -18.2 + 0.5i$ from [14]) the propagation length is increased to $L_{\mathrm{SPP}} \approx 60\,\mu\mathrm{m}$. Thus, silver is a better plasmonic candidate than gold, as it shows a lower SPP attenuation. At the same time, gold doesn't oxidize in air, which makes it easy to study surface plasmons on the gold/air interface while silver layers are susceptible to chemical attack in air. Thus, in terms of fabrication, silver degrades relatively quickly and the thickness threshold for uniform, continuous films is around 12-23 nm [20, 21]. For this reason, all the studies of plasmons herein are performed on gold structures. That being said, conceptual explanations though focus on Au, are widely applicable to other noble metals.

When the metal is shaped as a thin film on top of a dielectric, surface plasmons can propagate along both interfaces of that film, and, if it is sufficiently thin, i.e., $\approx 50\,\mathrm{nm}$, the SPPs can couple. For a symmetrically-embedded metal film, the interaction between the evanescent SPP fields in the metal gives rise to symmetric and asymmetric modes which have very different propagation lengths [8]. The asymmetric mode can propagate for a much longer distance than its symmetric counterpart, and its propagation length is considerably larger than that of a plasmon on a semi-infinite interface. The SPPs with long propagation lengths are called *long-range* surface plasmons [22, 23].

In the present thesis, however, the focus is on surface plasmons propagating along a *single* interface.

SPP penetration depth The SP is also characterized by a decay of the electromagnetic field in the direction normal to the surface, on either side of the interface. This decay is characterized by the complex wave vector k_z and Eq. (1.11). If an electromagnetic wave impinges on a metal surface it can only penetrate the solid up to a certain material dependent depth. This so called ***penetration depth*** is defined as the distance, where the exponentially decreasing evanescent

field falls to $1/e$ times its intitial value [4]. The decay length of the SPP electric fields away from the interface can be obtained from Eq. (1.11):

$$\begin{aligned} L_{z_j} &= \frac{1}{|k_{z_j}|}, \\ L_{z_1} &= \frac{\lambda_0}{2\pi}\left|\frac{\epsilon_1' + \epsilon_2}{\epsilon_1'^2}\right|^{1/2} \quad L_{z_2} = \frac{\lambda_0}{2\pi}\left|\frac{\epsilon_1' + \epsilon_2}{\epsilon_2^2}\right|^{1/2}. \end{aligned} \tag{1.14}$$

Using the same parameters for silver and gold as before (i.e., the dielectric functions at $\lambda = 633\,\text{nm}$) we obtain for the evanescent decay length pairs (L_{z_1}, L_{z_2}) of the electric fields (23 nm, 421 nm) and (28 nm, 328 nm), respectively. In this way, the decay length of the plasmon field in the dielectric material, L_{z_2}, is typically of the order of half the wavelength of light involved and dictates the maximum height of any individual structures that might be used to control SPPs. The decay length in the metal, L_{z_1}, determines the minimum feature size that can be used. Usually this is between one and two orders of magnitude smaller than the wavelength involved, thus highlighting the need for good control of fabrication at the nanometer scale.

1.2.2.4 Surface plasmon excitation

As we have presented in Fig. 1.3, the value of the SPP wave number k_{SPP} is larger than that of light in free space k_0. Consequently, there is a wavevector mismatch between the surface plasmon and free-space radiation, and it is therefore not possible to directly excite the SPP by shining light on a smooth metal surface.

Various schemes have been used to add the missing momentum to the incident photon (see Fig. 1.4). Prism coupling schemes, shown in Fig. 1.4(a-c), as proposed by Kretschmann and Otto [24, 25], are still widely used, especially in surface-plasmon spectroscopy [26, 27]. These schemes require careful angular tuning of the setup for coupling to the surface plasmons. A scanning near-field optical microscope (SNOM) tip [Fig. 1.4(d)] is also a widely-used powerful tool for both local excitation and probing of the surface plasmons [28]. Finally, a surface feature like a protrusion, grating, or surface roughness can be employed to couple and de-couple SPPs [Fig. 1.4(e-f)]. For all excitation schemes the polarization of the incident radiation has to be set for an optimal excitation of surface

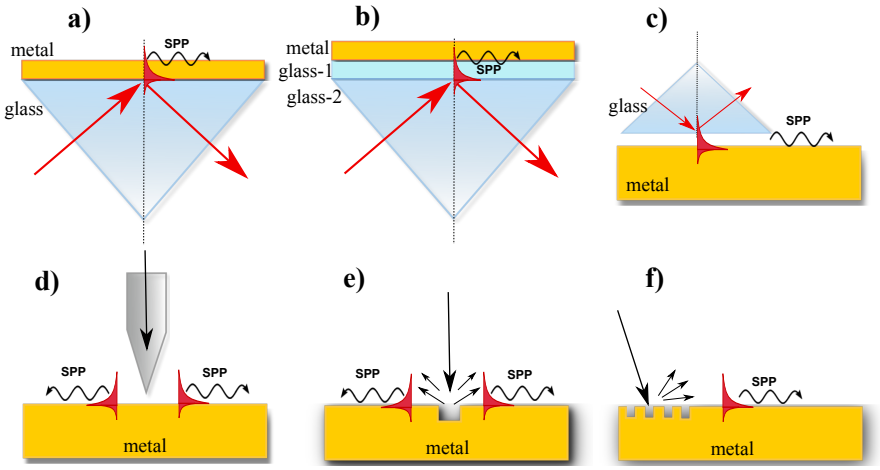

Figure 1.4: *Surface plasmon excitation schemes:* ***(a)****Kretschmann configuration;* ***(b)*** *double-layer Kretschmann configuration;* ***(c)*** *Otto configuration;* ***(d)*** *excitation with a SNOM probe;* ***(e)*** *light diffraction on a single surface feature;* ***(f)*** *excitation by means of a diffraction grating.*

plasmon.

In this work, where we use slit and grating structures to launch SPPs, the incident light has to be **TM**-polarized, perpendicular to the slit/grating axis.

1.2.3 Localized surface plasmons

In general, we have seen that plasmons arise from an interplay of electron density oscillations and the exciting electromagnetic fields. In this sense, we should make distinction between ***surface plasmon polaritons*** (SPP), i.e., propagating (evanescent) modes at the interface of a metal and a dielectric, and their localized counterpart at the surface of metallic particles, so called particle plasmon or ***localized surface plasmons*** (LSP). The SPPs *propagate* on essentially extended interfaces (length scale much larger than the optical wavelength), while LSPs are associated with metal objects or protrusions whose spatial dimension is assumed to be smaller than the wavelength of light [12, 29]. If an electromagnetic wave impinges on a metallic nanoparticle, the electron gas gets polarized (polarization charges at the surface) and the resulting restoring force again forms a plasmonic oscillation. The metallic particle thus acts like an oscillator and the corresponding resonance behavior determines the optical properties. The latter are responsible, e.g., for the optical properties of the Lycurgus cup mentioned

earlier.

Since we solely discuss surface plasmon polaritons in this work, we will always refer to them in the rest of this thesis.

1.2.4 Plasmon detection

The processes of generation, propagation, confinement of surface plasmons are at the heart of plasmonics. The progress and achievements in this field depends to a large extent on our ability to visualize surface plasmons in their different forms. In this thesis, the pump-probe thermoreflectance approach is applied for the first time to indirectly image the SPP-induced absorption in nanostructured surfaces. Thus, in order to understand the studies made so far and to realize the importance of our work with respect to them, we have summarized in Table 1.1 the main schemes employed for plasmon imaging and the way how they are used to reveal SPs field distribution (both SPPs and LSPs). The interested reader can find a review of all plasmon imaging techniques, their principal characteristics, advantages, and limitations, with discussions and references taken from the literature in a dedicated book chapter in Ref. [30].

We would like to add the above list a new imaging technique based on the plasmon absorption in the metal and excitation of hot electrons in the metal. This technique is able to reveal new knowledge and understanding of both SPPs and electron properties, while advancing their manipulation within nanophotonic devices. In the next section the notion of *hot electrons*, and what physical information they deliver, will be discussed .

1.3 Physics of hot electrons

1.3.1 Dielectric function of noble metals

As we have stated in the beginning of the chapter, most of the physics behind the interaction of light with metal structures is taken into account in the frequency dependence of the metal's complex dielectric function.

The electron dynamics inside metals is also described by the same dielectric function, and in case of a transient change of it, the *spectral* and *temporal* vari-

Table 1.1: ***Plasmon imaging techniques***

Imaging technique	**Make use of:**	**Reference**
Near-field microscopy (NSOM)	- evanescent SP field confined at the metal/dielectric interface	[31–35]
Leakage radiation microscopy (LRM)	-leaked SPs through thin metal into the substrate	[36–39]
Fluorescence microscopy	-molecule fluorescence excited by SPs	[40–42]
Dark-field microscopy	-scattered photons by particle plasmons	[43, 44]
Cathodoluminescence	-SP to photon conversion	[45, 46]
Nonlinear confocal microscopy	-SP induced non-linear phenomena (e.g., Two Photon Luminescence)	[47, 48]
Photo-electron microscopy	-SP induced non-linear enhancement of electron emission	[49, 50]
Electron Energy Loss Spectroscopy EELS	-losses in the electron energy due to SPs	[51, 52]
Photochemical imaging	-SP as launchers of photochemical reactions	[53, 54]

ations of $\epsilon(\omega, t)$ are given by the change of the occupied electronic energy states. The electronic energy states are determined by the electron band structure of the corresponding material. Thus, we need to address the noble metals in terms of their band structure.

Noble metals, in particular Au, Ag and Cu, have similar band structures, which include a set of five valence bands with low dispersion, called d-bands (composed of electron levels originating from the atoms' d-orbitals), and a half-filled sp-band called the conduction band. All the electron bands are therefore either filled or empty, except for the conduction band which is filled up to the Fermi level E_F [6].

[6]Strictly speaking this is only true at zero electronic temperature T_e, but remains an excellent approximation at higher temperatures in metals for which $k_B T_e << E_F$.

A calculated electronic band structure of gold taken from Ref. [55] is presented in Fig. 1.5(a). The d-bands are located a few eV below the Fermi level. The sp-band crosses the latter near the X, L, and Γ points of the Brillouin zone (BZ). For gold, the contribution of electronic transitions in the neighborhood of the L point dominates (marked region in Fig. 1.5(a), with a zoom of this region in Fig. 1.5(c)). Locally, in a given direction of the reciprocal (momentum) space, the band structure near the L point displays the characteristics of quasi-free electron behavior (parabolic band), with a dispersion law of the form $E(k) = \hbar^2 k^2 / 2m_{\text{eff}}$.

Most of the electronic properties involve only a small number of the electron bands, and often even involve only the conduction band states near the Fermi energy. This is the case for the interactions of the conduction electrons, such as electron-electron and electron-phonon interactions, and for the optical response in the IR to visible spectral range. However, the response of the noble metals to an electromagnetic excitation in the UV- visible range cannot be solely described in terms of the behavior of the quasi-free conduction electrons (sp-band), but must include the influence of bound electrons in the d-bands. As we have discussed before and shown in section 1.2.1, the Drude model is a good approximation only in the near-IR up to visible spectral range. By analyzing Fig. 1.5(b), which exemplifies the calculated electron density of states in Au, we can say that for light wavelengths above 2 eV, electrons can be promoted from d-bands below the Fermi energy to the states above.

Based on this, we could state that in a metal, light-matter interactions involve two main electronic mechanisms which explain the optical response:

1. **Intraband contribution:** This is due to quasi-free electrons of density n in the conduction band and is associated with optical transitions within the same band, or ***intraband transitions***. The contribution of the quasi-free electrons to the dielectric function can be described classically via the Drude model and ϵ_{Drude} (Eq. (1.2), Ref. [12]).

2. **Interband contribution:** This contribution is related to optical transitions between two electronic bands, or ***interband transitions*** (from filled bands to states in the conduction band, or from the latter to empty bands of higher energy). By virtue of the Pauli exclusion principle, a d-band electron can only be excited into an unoccupied state of the conduction band,

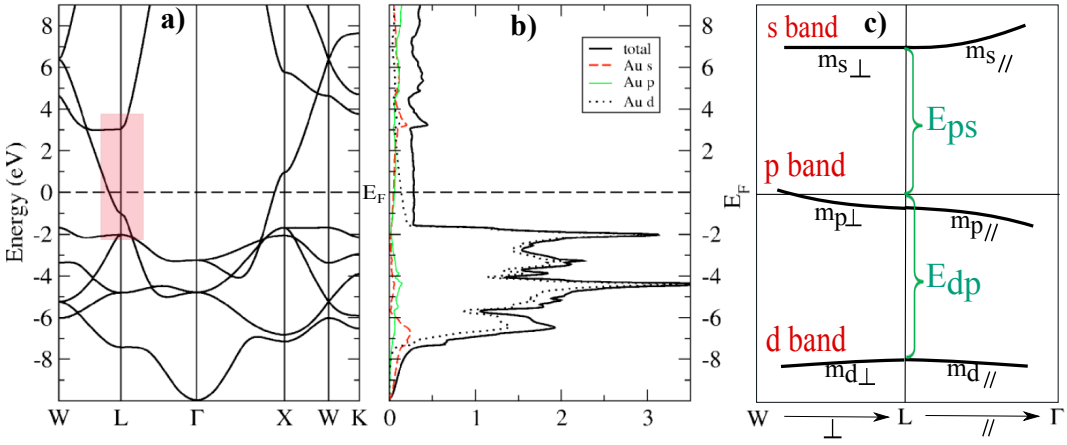

Figure 1.5: *Calculated Electronic band-structure* ***(a)*** *and density of states* ***(b)*** *plots for gold, taken from [55]. Above* 2 eV *(i.e. light wavelengths shorter than* 620 nm *)electrons can be promoted from the d-bands below the Fermi energy to states above, which leads to strong plasmon damping and the absorption of bluish light yielding the golden color.* ***(c)*** *Model for the band structure of gold near the L point of the Brillouin zone, marked in* ***(a)****, and close to the Fermi level. The parameters arising in the calculation of the dielectric function are indicated.*

i.e., above the Fermi energy E_F. Thus, there is a minimal photon energy for which the interband transition can occur, corresponding to the excitation of an electron from the top of the valence band to the Fermi level E_F situated in the conduction band. This defines an energy threshold below which the imaginary part of the interband contribution to the dielectric function is zero. Whereas this threshold falls in the UV range for silver (3.9 eV) [56], it lies in the visible range for gold and copper (at around 2.4 and 2.1 eV, respectively) [56, 57]. Unlike the intraband transitions, the interband contribution to the dielectric function of the noble metals cannot be calculated classically. One must then evaluate the sum over all possible transitions from an occupied state of the valence band to a free state in the conduction band. A detailed model of the band structure of the metal is then required [58–60]. This problem was addressed and solved in the 1970s by Rosei and coworkers [59–63] .

Therefore, the total dielectric function ϵ_m of noble metals can be written as the sum of two contributions, one due to electron transitions in the conduction

band (described by Drude model, ϵ_{Drude}) and the other arising from transitions from the d-bands to the conduction band (interband transitions, ϵ_{ib}):

$$\epsilon_m = \epsilon_{Drude} + \epsilon_{ib}. \tag{1.15}$$

For some metals (e.g., the alkali metals), interband transitions occur at high frequencies and only lead to a small correction to the real part of ϵ_m in the optical domain. In the noble metals, however, they are much more important and are essentially due to transitions between the d-bands and the sp conduction band.

Therefore, the interband term dominates the optical response in the visible and ultraviolet regions, whereas the intraband term is more important in the red and IR regions.

1.3.2 Interband (d-band to Fermi level) transitions and their role in electronic temperature measurement

In this work we employ femtosecond pump-probe thermoreflectance to study the plasmon- induced absorption. From a microscopic point of view, the aim of the thermoreflectance experiment is to perturb the electronic distribution around the Fermi level and induce changes in ϵ' and ϵ'', thereby changing material's reflectivity R. Thus, most of the thesis is concerned with exploiting the change in reflectance ΔR associated with the change in the temperature of a metal, specifically the electronic temperature.

In particular, we focus on exploiting the prominent thermomodulation feature [64] near 2.4 eV associated with d-band to Fermi level transitions in Au. We are interested in these transitions for two major reasons:

1. Since the variation of the dielectric function feature is due to the changes in the occupancy of electronic states near E_{F}, its magnitude is directly related to the temperature change of the electron gas. Due to this, in femtosecond pump-probe thermoreflectance (discussed in the next chapter), the metal's change in dielectric function serves as a good indicator of the temporal variations of the electronic temperature.

2. Its occurrence near 2.4 eV, in the visible spectrum range, places it near the

wavelength of the available femtosecond lasers, which is fortunate indeed, since one can thereby resolve the time behavior of ΔT_e, on the of order of 100 fs and less.

Because of the importance of this transition, it is indispensable to have a picture of how changes in electronic temperature can cause changes in the dielectric function around the d-band to E_{F} transition energy.

1.3.2.1 Simplified model calculation

A simple model for understanding experimental measurements of electron heating may be constructed by considering the interband transition from ***flat d-bands*** to the states the above Fermi level. The distribution of the occupied states is assumed to be described by Fermi-Dirac statistics at a well-defined electron temperature and we suppose that the change of the material response follows the changes of electron temperature T_{e}.

The physical mechanism responsible for the feature is as follows. The role of the ultrashort laser pulse is to induce a change in the electron distribution. Before the light pulse arrives, the electronic states are either mostly occupied or mostly empty (except within an energy of $k_{\mathrm{B}}T_e$ relative to the Fermi level). After the perturbation, the temperature of the electron gas increases and the heating induces changes in the distribution of occupied electronic states near Fermi level [65]. Thus, the tails of the Fermi distribution spread further out in energy (so-called **Fermi level smearing** [66]), emptying states below and filling states above the Fermi level (see Fig. 1.6(a)). The sample is probed by measuring its reflectivity change as a function of photon energy. If the Fermi level lies slightly above the optically probed states, the effect of heating is to cause an increase in absorption, since heating increases the number of states for absorption. On the other hand, if the Fermi level lies slightly below the optically probed states, decreased absorption will occur since Fermi level smearing decreases the number of states available for optical transitions. Scanning of the probing light in energy around the d-band to Fermi level transition reveals a“derivative like” feature for the absorption shown in Fig. 1.6(a).

For relatively large electron temperature changes, the smearing of the electron

distribution is given by:

$$\Delta f = f(E, T_{e1}) - f(E, T_{e0}), \tag{1.16}$$

where f is the Fermi distribution. Probing at a given energy $\hbar\omega$, the related electron energy can be expressed as $E = E_d + \hbar\omega$, with E_d being the energy of the d-band. Thus, the Fermi distribution function is expressed as

$$f(E, T_e) = \left(1 + e^{\frac{E-E_F}{k_B T_e}}\right)^{-1}, \tag{1.17}$$

These heating induced changes of the electronic states directly affect the absorption of photons with energies $\hbar\omega$ which corresponds to the transition of electrons from the top of the d-band (energy E_d) to the Fermi level (E_F). When the conduction-electron temperature increases during the heating pulse, the Fermi distribution of occupied states decreases slightly for $\hbar\omega < E_F - E_d$. That is, $df/dT_e < 0$ and more d-band electrons are promoted into the conduction band by the absorption of probe photons at these energies. This results in a *decrease* in the reflectivity (increase in absorption) for $\hbar\omega < E_\mathrm{F} - E_\mathrm{d}$. At the same time however, there is a heating-induced increase in the number of conduction electrons which occupy states above E_F; that is, $df/dT_e > 0$ for $\hbar\omega > E_\mathrm{F} - E_\mathrm{d}$. We expect to see a heating-induced *increase* in the reflectivity (decrease in absorption) since fewer empty conduction-band states are available for transitions from the d-band. When the probe's photon energy coincides with the transition energy from the d-band$\rightarrow E_\mathrm{F}$ (~ 2.38 eV in Au), there is no temperature modulation of the probed unoccupied states, thus $df/dT_e = 0$. The spectral behavior of df/dT_e is plotted in Fig. 1.6(b) for three different temperatures: 100, 300 and 600 K respectively. We see that as the temperature T_e of the conduction electrons is lowered, the spectral width of the Fermi distribution smearing df/dT_e is reduced. In any case, there is no Fermi smearing for a probing photon energy of 2.38 eV.

Assuming that the picture discussed above is correct, we may make a model calculation of $\Delta\epsilon$ associated with d-band$\rightarrow E_\mathrm{F}$ transition in Au. For this, we adopt the picture presented in Fig. 1.6(a) for the density of states $g(E)$ in Au. There, most of the electrons in the metal are in sp-states, and so make up a free electron gas with density of states $g(E) \propto E^{1/2}$ [12]. The d-states enter into

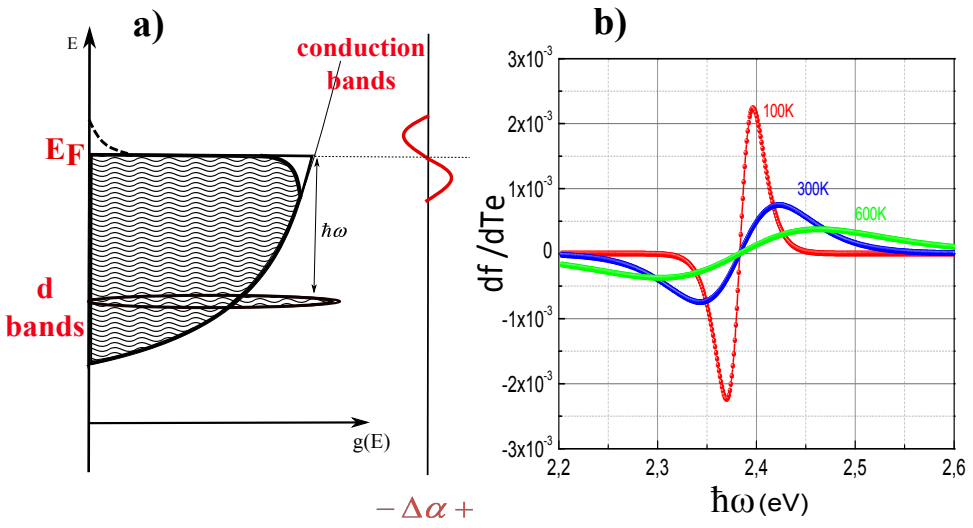

Figure 1.6: ***(a)*** *Simplified model of the electronic band structure in noble metals: isotropic parabolic conduction band and dispersionless d-bands. The dashed line shows the "Fermi level smearing" mechanism which cause the "derivative like" feature in absorption.* ***(b)*** *calculated temperature derivative of the Fermi distribution* $f(E,T_e)$ *, i.e., change in electronic occupancy, versus the energy difference between the top of the d-band and Fermi level in gold. The derivative is evaluated at* 100*,* 300 *and* 600 K*, demonstrating the spectral broadening as temperature increase.*

the density of states as a delta function at 2.38 eV below E_F. The number of electrons of energy E is given by:

$$n(E) = f(E,T_e)g(E), \tag{1.18}$$

where $g(E)$ is the density of states and $f(E,T_e)$ is the Fermi-Dirac distribution function described by Eq. (1.17). Now we want to calculate the change in ϵ'' due to Fermi level smearing caused by the increase in the electronic temperature T_e. We may separate ϵ'' into free and bound parts (intra- and inter-band constributions):

$$\epsilon'' = \epsilon''_{Drude} + \epsilon''_{ib}(T_e). \tag{1.19}$$

In this model, the amount of absorption (i.e., contribution to $\epsilon''_{ib}(T_e)$) depends on the availability of electrons for transitions in the d-states, as well as the number

of empty states near E_F. Assuming $g(E_F) = N_0$[7] we can write:

$$\epsilon''_{ib}(\hbar\omega, T_e) \propto N_d N_0 f(E_d, T_e)(1 - f(E_d + \hbar\omega, T_e)), \tag{1.20}$$

where N_d is the density of states in the d-band. In Eq. (1.20) it is considered that the d-bands are delta functions in energy and we ignore variations in $g(E)$ around E_F. Now, since the d-band states are completely filled, the problem simplifies because $f(E_\mathrm{d}, T_e) = 1$ for all k. Then, when T_e changes, ϵ''_{ib} changes as:

$$\Delta\epsilon''_{ib}(\hbar\omega) \propto N_d N_0 (f(\hbar\omega, T_e + \Delta T_e) - f(\hbar\omega, T_e)) = C\frac{\partial f(\hbar\omega)}{\partial T_e}\Delta T_e, \tag{1.21}$$

where C is some constant which can be determined experimentally, and ΔT_e is the rise in temperature of the electron gas. It is important to note the appearance of the term $\partial f/\partial T_e$ which gives rise to the characteristic derivative-lineshape in Fig. 1.6(b)(observed also in thermoreflectance experiments).

Finally, the change in ϵ' must accompany changes in ϵ''. Since ϵ' and ϵ'' are related via Kramers-Kronig relations [67], one can also derive an expression relating $\Delta\epsilon'$ and $\Delta\epsilon''$:

$$\Delta\epsilon'(\omega) = \frac{1}{\pi}P\int_{-\infty}^{\infty} d\omega' \frac{\Delta\epsilon''(\omega')}{\omega' - \omega}, \tag{1.22}$$

where P denotes the principal value of the integral. In this way, we consider the two contributions of $\Delta\epsilon'$ and $\Delta\epsilon''$, since reflectivity change depends on them both. As we probe close to the interband transition, we have chosen not to consider the contribution of free electrons (ϵ_{Drude}). However, while probing far from interband transition this consideration is no longer valid. In this case this term can be dominant.

1.3.2.2 Real model calculation

Unfortunately, the model described above is qualitatively, but not quantitatively correct. First, neither the d-bands nor p-states near E_F are dispersionless. Both

[7] We take the density of states near the Fermi level to be roughly constant. This approximation is fine, since we are only interested in states within a range of $\approx k_\mathrm{B}T_e$ relative to the Fermi level, and the variation of the density of states is minimal in the noble metals at E_F over this small interval.

display marked curvature as the wavevector k is varied around the Brillouin zone. In this case, the optical absorption will not occur at one precisely defined energy and the width of the Fermi-smearing feature will be broadened. For a quantitative result we need to consider parabolic bands with different masses in the directions parallel and perpendicular to the $\Gamma \rightarrow L$ direction in the Brillouin zone; the real electronic band structure of gold was previously shown in Fig. 1.5(a,c). Second, the width of the feature is broadened by the enormous carrier density present in the metal. The presence of other carriers greatly reduces the lifetime of both the hole created in the d-bands as well as the electron placed in the p-band near E_{F}.

As we have mentioned in section 1.3.1 an accurate model for calculating temperature induced variation of $\Delta\epsilon$ and the following ΔR has been developed by Rosei *et al.* [59–62] for the purpose of detailed characterization of the band structure of noble metals with thermomodulation[8] experiments.

In the spectral region that we consider, following Rosei, the interband dielectric functions of the noble metals are described by a ***three-band model***: interband transitions d→ p from the filled d-band to the conduction band p, near the Fermi level, and p→ s from the conduction band to the empty s-band. Finally, $\Delta\epsilon''$ is proportional to the joint density of states, i.e., associated with a transition of given energy, which is equal to the density of states in the d and s,p-bands satisfying energy and wavevector conservations [59].

This approach is commonly used to calculate the modification of the optical properties of noble metal films and nanoparticles induced by absorption of an ultrashort laser pulse.

[8]Modulation spectroscopy involves periodically perturbing the sample, and measuring changes in the optical spectrum which is synchronized with the perturbation. Since only changes in the optical spectrum are measured, modulation spectroscopy is extremely sensitive to critical points in the band structure. There are several different types of modulation spectroscopy, each characterized by the kind of perturbation used: piezomodulation where a periodic stress is applied; electromodulation where an electric field is used; thermomodulation where a current modulates the sample's temperature.

1.3.3 Hot electron spectral and temporal variations and their link with reflectivity

1.3.3.1 Spectral variations

Up to now we have discussed the microscopic origins of the dielectric function and have derived an expression for $\epsilon(\omega)$ in terms of electron distribution. Since $\epsilon(\omega)$ links the microscopic physics of transitions in the metal with the macroscopically observable reflectivity, we will focus on understanding how changes due to electron dynamics in the sample, cause the reflectivity to change. We may write the fractional change of the reflectivity $\Delta R/R$ due to variations in ϵ as [68]:

$$\frac{\Delta R}{R} = \frac{\partial \ln R}{\partial \epsilon'}\Delta\epsilon' + \frac{\partial \ln R}{\partial \epsilon''}\Delta\epsilon''. \tag{1.23}$$

On the other hand, in a semi-infinite medium the macroscopic optical reflectivity R is related to n and k via the well-known formula [67]:

$$R = \frac{(n-1)^2 + k^2}{(n+1)^2 + k^2}. \tag{1.24}$$

By taking into account that $n = \sqrt{\epsilon}$, such that $\epsilon' = n^2 - k^2$ and $\epsilon'' = 2nk$ we can therefore estimate the fractional coefficients:

$$\frac{\partial \ln R}{\partial \epsilon'} = \frac{n}{n^2 + k^2}\left(\frac{n-1}{(n-1)^2 + k^2} - \frac{n+1}{(n+1)^2 + k^2}\right), \tag{1.25}$$

$$\frac{\partial \ln R}{\partial \epsilon''} = \frac{k}{n^2 + k^2}\left(\frac{n-1}{(n-1)^2 + k^2} - \frac{n+1}{(n+1)^2 + k^2}\right) + \frac{n}{n^2 + k^2}\left(\frac{k}{(n-1)^2 + k^2} - \frac{k}{(n+1)^2 + k^2}\right). \tag{1.26}$$

These coefficients are numbers determined by the complex refractive index of the metal at the probe wavelength, which may be estimated using an interpolation of the available optical data in gold.

In this way the changes in real and imaginary parts of the dielectric function can be related to the transient relative changes of reflectivity. Thus, features

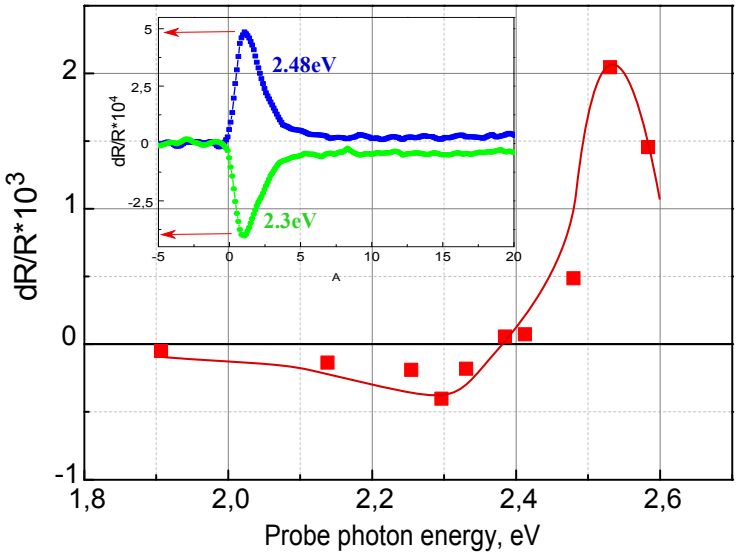

Figure 1.7: *Maximum changes of probe beam reflectivity obtained in pump-probe experiments on a 50 nm thick gold film with probe photon energies around the threshold of interband transitions (red squares) The red line is a guide for the eyes. The inset shows two typical pump-probe traces for a probe photon energy of* 2.48 *and* 2.3 eV*, i.e., for* 500 *and* 540 nm *probe wavelengths.*

in the dielectric function, in particular the derivative-like shape due to changes in the electron distribution function [Fig. 1.6(b)], will also be recovered in the $\Delta R/R$ spectral response.

Scouler [69], Rosei and Lynch [59] were the first to observe a polarity reversal of ΔR when the photon energy was tuned through the d-band $\rightarrow E_{\mathrm{F}}$ transition energy of Au and Cu. The unique polarity reversal of the thermoreflectance signal originating from this transition was interpreted as the result of Fermi distribution smearing, that is, a heating-induced increase in unoccupied states above the Fermi level and a decrease in occupied states below it.

We have performed a preliminary test of the model for the dielectric function, i.e., we have verified for a well-defined pump fluence (thus a fixed electron temperature), the trend of $\Delta R/R$ with probe photon energy around the interband transition threshold (around 2.4 eV). Corresponding pump-probe measurements were carried out on a 50 nm thick gold film. The maximum values of the probe beam reflectivity change $(\Delta R/R)_{max}$, taken from time-dependent measurements as shown in the inset, are plotted in Fig. 1.7 as a function of the photon energy

of the probe beam. The observed variations with photon energy and the sign change at the interband transition threshold are in qualitative agreement with earlier results reported in the literature [66, 68]. These variations of transient reflectivity with photon energies close to the interband transition threshold are a general feature of all noble metals.

1.3.3.2 Temporal variations

The dielectric function given by Eq. (1.21) is static. For a complete spectral and temporal characterization of the detected optical signal we then incorporate the time dependence in the Fermi-Dirac distribution via the electron temperature $T_e(t)$.

When considering the evolution of absorbed energy into the metal, we distinguish three processes occurring in successive time intervals, as sketched in Fig. 1.8. To induce a change in the dielectric function of a metal we irradiate its surface with an ultrashort pump pulse, transferring energy to the free electrons through the absorption of the incident photons. Although the electrons are initially in a nonthermal distribution [Fig. 1.8(a)] [68, 70], electron-electron collisions establish a temperature within $\approx 500\,\mathrm{fs}$ in gold [71], after which the electrons can be described by Fermi statistics. Once the thermal equilibrium among the excited electrons is established, we encounter the physical situation of a ***hot electron*** bath in a ***cold lattice***, which can be described by two separate temperatures T_e and T_l [Fig. 1.8(b)]. Subsequently, electron-phonon collisions transfer energy from the electrons to the lattice, leading to a thermal equilibrium of the entire system in several picoseconds [Fig. 1.8(c)].

In this thesis, when referring to *hot electrons*, we address the bath of hot electrons, which are internally thermalized, but out of the equilibrium with the lattice, situation depicted in Fig. 1.8(b). The distribution of this hot electrons is assumed to be described by a Fermi-Dirac statistics at a well-defined electron temperature and we suppose that the change of the material response follows the changes in T_e. The energy exchange between the electrons and the lattice is described in time by the ***two temperature model*** (TTM) which uses a set of two coupled diffusion equations, one describing the heat conduction of electrons and another of the lattice. Both equations are connected by a term that is proportional to the electron-phonon coupling constant g and

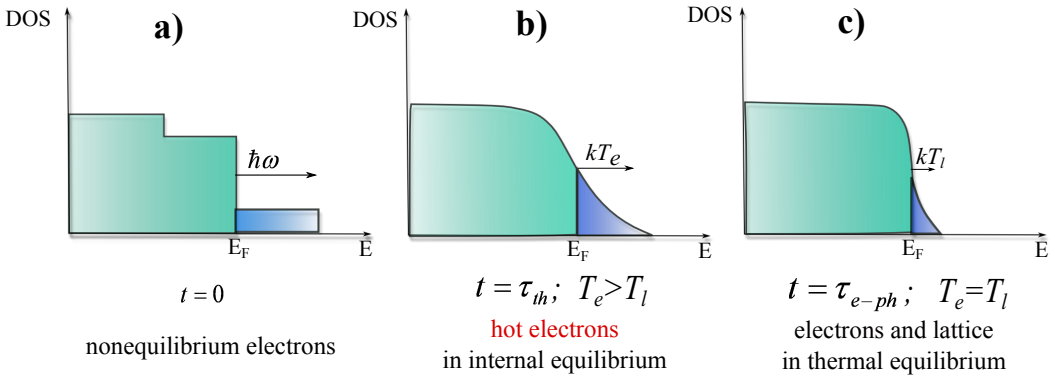

Figure 1.8: *Three distinguished relaxation phases of optically excited electrons in metals:* ***(a)*** *Photon absorption within the optical penetration depth generates at t=0 nonequilibrium electrons.* ***(b)*** *At $t=\tau_p h$ electrons have equilibrated by electron-electron collisions forming a Fermi distribution with a well defined temperature T_e.* ***(c)*** *Electrons reach the equilibrium with the lattice through electron-phonon coupling at $t=\tau_{e-ph}$.*

to the temperature difference between the two baths. The assumption that the electron phonon coupling can be merged into one linear coupling term of the form $g(T_e - T_l)$ is the essence of the two-temperature model (TTM), originally proposed by Anisimov *et al.* [72]. It can be written in the form:

$$C_e(T_e)\frac{\partial T_e}{\partial t} = \frac{\partial}{\partial z}\left(K_e \frac{\partial}{\partial z} T_e\right) - g(T_e - T_l) + P(\mathbf{r}, t), \tag{1.27a}$$

$$C_l \frac{\partial T_l}{\partial t} = g(T_e - T_l). \tag{1.27b}$$

Here C_e and C_l are the respective heat capacities of electrons and the lattice, and K_e is the thermal conductivity of the electrons. Since we are only interested in the relaxation dynamics that leads to the thermal equilibrium of electrons and lattice, the heat conduction of the lattice is neglected. The source term:

$$P(\mathbf{r}, t) = \frac{\alpha A I(\mathbf{r}, t) e^{-\alpha z}}{(1 - e^{-\alpha d})}, \tag{1.28}$$

describes the absorbed energy density, determined by optical penetration depth

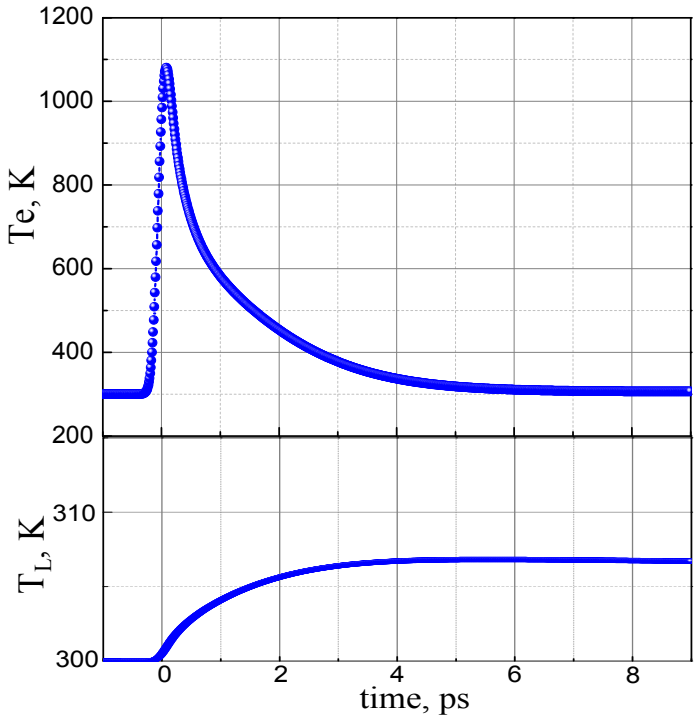

Figure 1.9: *Electron temperature relaxation at the surface of a 200nm thick gold film (upper panel) and lattice heating (lower panel) predicted by the TTM. The following material constants were used for calculation:* $g = 2 \cdot 10^{16} W/m^3 K$, $R = 0.408$, $1/\alpha = 15.328 \cdot 10^{-9} m$, $C_e = \gamma T_e$ *with* $\gamma = 67.96\,\mathrm{J/m^3K^2}$, $K_e = K_{e,0} \cdot T_e/T_l$ *with* $K_{e,0} = 318\,\mathrm{W/mK}$, *gold film thickness* $d = 200\,\mathrm{nm}$ *and fluence* $0.5\,\mathrm{mJ/cm^2}$.

$1/\alpha$[9], film thickness d, and the absorbed fraction of the incident intensity $AI(\mathbf{r}, t)$, with $A = (1 - R - T)$. Here R and T denote reflectivity and transmissivity, respectively.

We have numerically solved the TTM, in order to predict the time dependence of T_e and T_l. A typical time evolution of the electron and the lattice temperatures at a gold film surface is shown in Fig. 1.9. We simulate here the perturbation of the surface of a gold film in the condition similar to a femtosecond pump-probe experiment. The curves have been calculated with the following material constants: $g = 2 \cdot 10^{16}\,\mathrm{W/m^3K}$, $R = 0.408$, $1/\alpha = 15.328 \cdot 10^{-9}\,\mathrm{m}$, $C_e = \gamma T_e$ with

[9]For more exact calculations the model has to account for the ballistic motion of electrons. This effect can be incorporated in the TTM by adding the ballistic range (λ_{ball}) to the optical penetration depth in the source term (λ_s). In this case in Eq.1.28 the total energy deposition depth can be written as $\alpha^{-1} = \lambda_s + \lambda_{ball}$.

γ = 67.96 J/m^{3}K^2, K_e = $K_{e,0} \cdot T_e/T_l$ with $K_{e,0}$ = 318 W/mK, gold film thickness d = 200 nm and fluence 0.5 mJ/cm^2. Both T_e and T_l, before the perturbation, have the same initial temperature, equal to that of the ambient 300 K. After the energy has been injected into the system, it is absorbed by the electrons, giving rise to an electron temperature variation of more than 1000 K in the first picosecond. Afterward, the electrons relax with the lattice, their temperature decreases, while the temperature of the lattice increases. Finally, after $\approx$ 6 ps we have a thermal equilibrium within electrons and lattice ions, with $T_e = T_l$ = 307 K in the perturbed region.

1.4 Conclusion

In this chapter we provided a separate description of surface plasmons and hot electrons. However, plasmons and electrons may interact in metals in a time scale of a few tens of femtoseconds. This interaction is followed by the SPP energy transfer to the electrons (plasmon absorption) and the consequent electron temperature variation at at femtosecond time-scale the electrons are hot and out of the equilibrium with lattice.

The hot electron dynamics inside metals is described by the dielectric permittivity, and a transient change of it cause a change in the optical reflectivity. Thus, based on a simple model we explained how the changes in electronic temperature are linked with the permittivity variations. and shown that in order to resolve the initial electron heating contribution to optical reflectivity in noble metals, we must use probing photon energies which produce transitions from the d-band to the Fermi level.

Finally, by employing a two temperature model, we illustrated the different characteristic times involved in the relaxation processes.

CHAPTER 2

Femtosecond pump-probe thermoreflectance for ultrafast measurements

In this work we are interested in the transient response of hot electrons excited by plasmons in noble metals. Time scales of electronic relaxation are in the order of few hundred of femtoseconds up to a few picoseconds. In order to achieve this time resolution we have chosen to use thermoreflectance pump-probe spectroscopy.

The bench we describe here has been developed during the PhD work of Gaëtan Calbris. This bench was suited for the study of nanoparticles in solution in a transmission configuration. We adapted the set-up for imaging and filming reflectivity changes with a spatial resolution limited by diffraction ($0.5\,\mu$m) and a temporal resolution limited by the pulse duration (150 fs). The bench we developed allows different measurement configuration such as transient point measurement, snapshots, and temperature field movies in reflection, transmission configuration with the capacity to focus the pump and the probe beams either both on the front side or one on the front and the second beam on the rear side of the sample.

This state-of-the-art experiment in femtosecond thermoreflectance allows plasmon absorption imaging in metallic structure with 150 fs time resolution.

Contents

2.1 Introduction

In the previous chapter we have formulated the connections between optical properties, namely reflectivity, and microscopic material states. In particular, we found that linear reflectivity properties are determined by the dielectric function $\epsilon(\omega)$, which in turn depends on the electron transitions in the material. Since we are concerned about electron dynamics we need to keep in mind that generally, electron dynamics in solids is a very fast phenomenon that has a time scale on the order of femtoseconds (10^{-15} s) to picoseconds (10^{-12} s). To analyze such types of processes, it is necessary to use short laser pulses to perturb the sample with a temporal resolution equal to or larger than the involved time scales. It is impossible to understand fast processes by using long perturbations.

Typically, the heat diffusion time in a metal film is on the order of nanoseconds (10^{-9} s) to microseconds (10^{-6} s) time scales, and the electron-phonon coupling time of most materials is from picoseconds to nanoseconds. Therefore, only when laser energy is deposited at a time scale much shorter than both the heat transport and the electron-phonon coupling, it is possible both to generate and probe the electron relaxation dynamics.

Consequently, using femtosecond laser pulses is indispensable for purposes of shortening both perturbation and probe (response) times.

Remarkable progress in the generation of femtosecond pulses with solid-state lasers has followed from the discovery of self-mode-locking in a Ti:sapphire laser by Sibbett's group in 1991 [73]. This discovery has opened a new scientific field-***ultrafast phenomena***[1] - which has extended the comprehension of several disciplines such us physics, material science, chemistry and biology. The first, and most obvious, characteristic of femtosecond lasers is that they produce pulses of light as short as a few femtoseconds[2] [75]. These short pulses can be used to observe phenomena with a resolution 1000 to 10000 times better than with any other known technique. Scientists can now directly observe many important phenomena including, for example, energy transfer from electrons to the lattice

[1] Ultrafast phenomena refers to phenomena which occurs on extremely short time scales (from fs to ns). For the study of the dynamics of such phenomena are employed *ultrasort pulses*, i.e., laser pulses whose duration is of the order of ps or less.

[2] We specifically refer here to the pulses with the duration in the femtosecond range. However, such pulses no longer hold the record for the shortest pulses artificially generated, as there have been reported pulses on the attosecond (10^{-18} s) time scale [74].

in solids [70], chemical reactions in gases [76], and the temporal evolution of luminescence in biological cells.

The second key characteristic of femtosecond pulses is that they can deliver an enormous amount of power with a moderately small amount of total energy, because the energy is compressed into a short time. In our experiment, we use pulses that are about 150 fs long and have up to a few $\approx \mu$J of energy, giving a peak power ranging from $\approx$ kW/cm^2 up to $\approx$ GW/cm^2. When such a laser pulse is focused to a small spot, the produced intensity and electric field are enormous. Thus, such a pulse is capable of generating a gas of hot electrons in a solid material. Furthermore, the laser pulse creates the hot electron gas before energy can be transferred from the excited electrons to the lattice. The free electrons can reach extremely high temperatures (thousands of K), while the lattice of atoms is still cold; this unique non-equilibrium excitation is exploited in our experiments in order to reveal the plasmon absorption.

The measurements described herein utilize the pump-probe technique [77]. The experiment employed throughout this work has been previously developed in this team [78] for the purpose of time-resolved studies of plasmonic nanoparticles. During this thesis it has been gradually adopted for imaging and time-resolved measurements of propagating surface plasmons. We will next proceed by presenting how we measure reflectivity variations by making use of femtosecond pump-probe experiments.

2.2 Experimental Set-up

2.2.1 Principles of pump-probe thermoreflectance

We utilize a pump-probe experiment with femtosecond pulses both to create and to measure the plasmon excited hot electrons and the consequent reflectivity change. The energy of the ultrashort laser pulses will be initially absorbed by electrons because they are charged. The electron temperature fastly increases while lattice remains cold, since electron's heat capacity is much smaller than that of the lattice. Later on, the energy is transferred to the cold atomic lattice until thermal equilibrium between electrons and the lattice is reached. Consequently, the ultrafast and highly photoexcited hot electrons can be measured using the

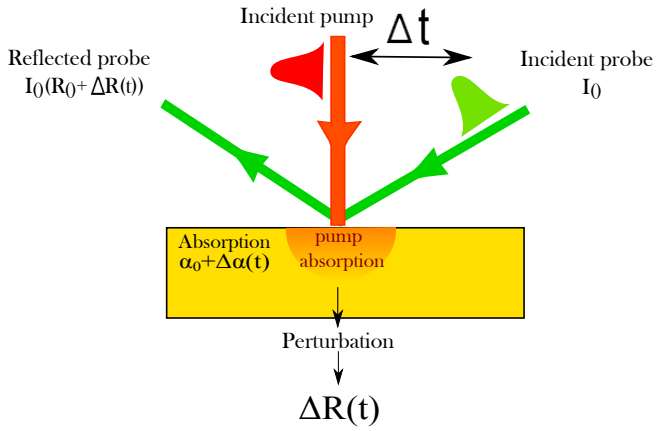

Figure 2.1: *Representation of optical pumping and probing of a metal film in a pump-probe experiment leading to a change of reflectivity.*

femtosecond pump-probe technique.

The basic idea of this experiment is depicted in Fig. 2.1. One laser pulse, called the ***pump*** pulse, starts to induce changes in the material. The impulsively induced excitation causes the optical properties (i.e., the reflectance, absorption) of the sample to change. After a certain time delay, a second, typically weaker pulse, called the ***probe***, "interrogates" the area that is perturbed. Reflected intensity of the probe beam is altered by the pump induced change. The action of the pump pulse on the sample may be analyzed in two different ways. The first is measuring the modification of the probe pulse characteristics (intensity, phase, wave vector, and etc.) after interacting with the sample, before and after the action of the pump pulse [68, 79]. The second is observing new effects created by the probe itself before and after the action of the pump pulse, including Raman scattering spectroscopy [80], laser-induced fluorescence [81], and coherent anti-Stokes Raman spectroscopy [82]. With respect to our experiment, the incident pump pulse will generate surface plasmon waves, whose absorption in the metal will modify the reflectivity and we measure the amount of the probe that is reflected from the affected region. The probe pulse can be variably delayed from the pump pulse, allowing the development of the excitation to be mapped out in time by scanning the probe delay.

The ammount of reflectivity and absorption variation, caused by the pump

pulse excitation, can be expressed respectively:

$$R_0 + \Delta R(t) \text{ and } \alpha_0 + \Delta\alpha(t), \tag{2.1}$$

where R_0, α_0 stand for the initial values of the optical properties and the second terms in the above expressions contain the information about the pump-induced perturbation (Fig. 2.1). The probe pulse should be *nonperturbative*[3], meaning that the intensity should be significantly smaller than that of the pump. If I_0 is the intensity of the incident probe beam, then the reflected probe beam intensity, due to a modified absorption, can be written as (Fig. 2.1):

$$I_0(R_0 + \Delta R(t)). \tag{2.2}$$

To reveal the dynamics of the physical processes under study, we need to combine the pump-probe reflectance principles described above with the principles of optical sampling. The commonly employed technique of optical sampling is the *synchronous sampling* [83]. The main feature of this type of sampling is that both the pump pulse train and the probe pulse train originate from the same laser source. The temporal delay between the two pulse trains is created via an optical path difference of one of the beams. In particular, we vary the delay between the pump and probe pulses by changing the distance the probe has to travel before reaching the sample: for each additional micron, the probe arrives 3.3 fs later. This implies that the initial pump and probe arms should be carefully made to be of *equal length*, starting from the source laser output up to the sample position. Experimentally, the optical path difference is created by inserting in the optical path of one beam a motorized translation stage with a retroreflecting mirror mounted on top of it. A displacement of the translation stage causes a variation of the path length of the respective beam. When the laser beam is reflected from the retroreflecting mirror, it makes a round trip in the translation stage. When the translation stage continuously change its position $X(t)$, we have a continuously varying path between two beams, which produces a continuously

[3]Even if the probe induces a perturbation, it can not be sensitive to "itself", unless it induces some nonlinear effects.

varying delay between pump and probe pulse trains:

$$\tau(t) = \frac{2X(t)}{c} \times N_{\text{paths}} \tag{2.3}$$

where c stands for speed of light in air, the factor of 2 appears because of the round trip made by the light at one reflection from the mirror and N_{paths} denotes the number of back-and-forth paths set on the translation stage. In this way we are able to precisely control the particular instant $\tau(t)$ when the probe pulse should "read" the material optical response, after the perturbation produced by the pump. The position $X(t)$ is measured relative to a reference position called "coincidence", which signifies the moment t_0 when pump and probe pulses arrive instantaneously on the sample.

The optical response of the material is reconstructed afterward by assigning to each position $X(t)$ of the translation stage a certain value $\tau(t)$ of the corresponding delay. According to Eq. (2.3) a delay of 100 fs is equivalent to a displacement of 15 μm of the translation stage. The latter quantity is easily attainable for commercial motorized translation stages.

2.2.2 Description of the laser chain

Both the excitation and the detection of thermal, plasmonic, mechanic phenomena depend critically on the wavelength. We need an accurate selection of the pump beam wavelength in order to excite the exact phenomena. The same reason is also valid for the selection of the probe beam, so that we need a certain probe wavelength to access the information of interest. Localized surface plasmons (LSPs) in nanoparticles have also been studied via pump-probe experiments and it has been shown that by adjusting the probe wavelength at the peak of surface plasmon resonance (SPR) reveals the information about absorption cross-section, whereas a probe set in the slope of the SPR reveals the mechanical properties of the nanoparticles [84]. This reason is also valid for non-structured materials, such as Al film. Probing with a red beam gives insight on the thermal properties of the metal, while a green beam is considerably more sensitive to acoustic effects [85].

For this reason, we require a tunability of the laser wavelengths. In our experiment we achieve this by employing an optical parametric amplifier (OPA) in

combination with an amplified laser chain. The laser chain consists of a commercial femtosecond Ti:Sapphire oscillator followed by a regenerative amplifier.

The femtosecond oscillator represents the first element of the laser chain. We use the "MIRA Model 900" Coherent company [86] mode-locked ultrafast laser which employs Titanium:Sapphire as the gain medium, is tunable from 710 up to 1000 nm and operates at a repetition rate of 76 MHz. The main operation parameters and the characteristics of the output beam are summarized in Table 2.1. A fine adjustment and optimization of this element is crucial, so as an instability at it's level can be amplified through a cascade effect along the entire chain. The pulse train delivered by the oscillator is injected afterwards in the regenerative amplifier.

The regenerative amplifier in this chain is a commercial "RegA" Coherent system ([87], Table 2.1) operating at $\lambda = 800$ nm. The time required for a pulse amplification allows RegA an injection of only *one* pulse each 4 μs. This causes a reduction of the repetition rate of RegA pulse train to 250 kHz. At the RegA exit, a beamsplitter was introduced which allows to take a part of the output beam and inject it directly into the experimental bench. The remaining part of the RegA beam is still intense enough for injection in the optical parametric amplifier OPA.

We utilize a commercial "OPA 9400" from Coherent ([88], Table 2.1) for the purpose above, i.e., obtaining a tunability of laser wavelengths, particularly in the visible range. We obtain this spectral range by means of the parametrical amplification process. This process is based on a combination of two waves in a nonlinear crystal: from two waves of different frequencies, a new wave is generated with the frequency equal to the difference of the first two. As a result of this nonlinear process, pulse trains are generated in the range from 480 to 700 nm. Along with this main pulse train in the visible range, OPA also delivers a residual second harmonic (SH) beam at 400 nm and a white light continuum, which can also be used in the experiment when needed. The repetition rate of this pulse train is set by the RegA.

Both Mira and RegA are optically pumped by a Coherent Verdi V18 laser system. It represents a Nd:YAG laser which delivers 17.5 W at $\lambda = 532$ nm in CW regime. By using a 70/30 % beam-splitter, 5.5 W of the Verdi total power are used for MIRA pumping, and 12.5 W for RegA.

Table 2.1: ***Main characteristics of each element of the laser chain***

Chain element	Input beam λ	Output beam λ	Average output power	Repetition rate	Pulse duration	Energy / pulse
MIRA	532 nm	800 nm	600 mW	76 MHz	120 fs	≈ 8 nJ
RegA	532 nm/ 800 nm	800 nm	1 W	250 kHz	150 fs	$\approx 4\,\mu$J
OPA	800 nm	400 nm 480 – 700 nm	100 mW 15 mW	250 kHz	150 fs	$\approx 0.4\,\mu$J ≈ 60 nJ

In summary, the laser chain described above provides us three distinct laser beams: two of them are coming from OPA (one is tunable in the 480 – 700 nm range and the other is the 400 nm SH residuum) and the third beam is the 800 nm leakage-part taken directly from the RegA output. We have also added to our experimental bench a system of detachable mirrors and beam-splitters which allow one to easily switch between the three beams and the paths they follow, depending on the "role" they have in each experiment, i.e., which one will serve as a "pump" and which one, the "probe".

2.2.3 Description of the detection system

Since the laser beam intensity is not stable during the course of the experiments, it leads to low frequency fluctuations of the intensity and increase the noise in the detected signal. We can reduce the effects of this source of noise by using an electronic *differential detector*. The principle of its functioning is the real-time subtraction of the intensity of a reference beam from that of the beam reflected by the sample. The reference beam is chosen to have the same amplitude as the reflected one, but it comes directly from the source. The result is that fluctuations of the source laser output intensity (as the source is the same for all beams) are nearly canceled, leaving only the signal produced by the pump. We use a differential detector model "P140A" from Thorlabs, with silicon photodiodes which allow the operation in the wavelength range 320 nm to 1000 nm and a variable bandwidth from 100 kHz to 150 MHz.

The previously described differential detection is combined with a *lock-in detection*. The addition of this helps us to remove other undesirable signals other

than the fluctuations present in the source laser (e.g., electronic, mechanical or thermal perturbations), which are usually present in the environment.

To achieve this, we incorporated in the path of the pump beam a mechanical chopper as a modulator, which "chops" periodically the laser intensity at a frequency f_m, which in our case is about 10 kHz. In this way the excitation, and therefore the material response, are modulated at this frequency. Our goal is to measure the amplitude of this spectral component representing the signal we are interested in. To extract this particular signal we use Stanford Research Systems SR830 [89] lock-in amplifier. The output from the detector is sent to the lock-in amplifier, which is phase locked to the chopper. This is important for two reasons. First, a lock-in amplifier discards all signals which are not at exactly the same frequency as, and in phase with, the phase reference. Thus, lock-in detects modulations in the received probe intensity which are caused by the effect of only the pump on the sample; all other uninteresting signals are rejected. Second, the lock-in-chopper arrangement allows one to choose a modulation (i.e., chopping) frequency in a spectral region which is free of external noise (e.g., 50 Hz noise from room lights).

The output of this detection scheme gives us a voltage $\Delta V(t)$ proportional to the variation of the beam intensity $\Delta I(t)$. The division of this value by the photodiode voltage in the reference arm, i.e., the signal V_0 without excitation, allows one to directly obtain the relative variations of the reflectivity of the sample:

$$\frac{\Delta V(t)}{V_0} = \frac{\Delta I(t)}{I_0} = \frac{\Delta R(t)}{R_0} \tag{2.4}$$

Another important task is to find the correct phase setting of the lock-in internal reference. This is necessary because one must know the correct sign of the pump-probe signal, as an increase or decrease in reflectivity is associated with different electronic transitions at the microscopic level. Setting the phase is accomplished by blocking the probe beam with a card, turning off the reference channel (to eliminate noise), and increasing the gain on the lock-in until some constant signal is observed. This signal is caused by the detection of small amounts of scattered pump light; the correct phase setting is that which maximizes this signal.

With this system, we are able to detect pump-probe signals with relative amplitude variations of the order of 10^{-3} to 10^{-6}.

2.3 Measurements

As we have described before, the pump beam induces a perturbation in the system which evolves over space and time. In the following we describe different ways to perform measurements in order to access spatial and temporal information.

For each type of measurement, specific devices and optical components have been incorporated into the experimental bench. Their role and operation is explained within the context of the information we want to measure.

2.3.1 Measurement 1: Point-measurement vs time

The first type of measurements, the most commonly performed in pump-probe experiments, is to record the time-resolved response of the material caused by an excitation.

For a fixed position of the sample, we spatially overlap the pump and the probe beams. The pump pulse train periodically induces a perturbation in the system, while the probe pulse train monitors the reflectivity changes for a gradually increasing delay between the two pulse trains. As a result, one records the temporal response of a "point" sample region (from hereon called "pixel") of an area equal to the probe beam focus spot.

The critical characteristic of a temporal measurement is the temporal resolution. We will estimate the temporal resolution of the experimental set-up, which in our case translates into the minimal attainable temporal delay between the pump and probe pulses. We have established before that the temporal delay between the pump and the probe pulse, $\tau(t)$, is directly proportional to the translation stage position $X(t)$ [Eq. (2.3)]. In this case, the estimation of the temporal resolution relies on the estimation of the displacement uncertainties of the translation stage.

Here, we use a translation stage XML 350 (Ultra-Precision Linear Motor Stage) from Newport [90]. The different characteristics and stage positioning accuracy are summarized in Table 2.2. The maximal values of the intrinsic possible errors of the stage positions are of the order of about $1\,\mu$m, which is equivalent to a pump-probe delay of $\approx 13\,$fs. This is far smaller than the pulse duration,

Table 2.2: ***Summary of the resolution parameters of the translation stage***

	Maximal Length	**Maximal speed**	**Minimal increment**	**Resolution**	**Repetability**	**Precision**
Stage	350 mm	300 mm/s	10 nm	1 nm	80 nm	3 μm
Equivalent delay[4]	$\approx$ 4.6 ns	$\approx$ 4 ns/s	$\approx$ 0.13 fs	$\approx$ 0.013 fs	$\approx$ 1 fs	$\approx$ 40 fs

which means that the final parameter which fixes our temporal resolution is the pulse duration.

The maximal length of our translation stage is 35 cm. We have integrated two retroreflecting mirrors on it, causing the light to make a double round trip through the stage. In this way we have maximized the temporal range of the material response one is able to access. Therefore, according to Eq. (2.3), the maximal temporal range of the optical response, which we are able to explore is about 4.5 ns.

A typical temporal signal measured with our pump-probe experiment is presented in Fig. 2.2. It shows the relative change in reflectivity ($\Delta R/R$) of a gold film which follows a pump pulse excitation, for an increasing pump-probe delay. In the presented curve we can locate the "coincidence" delay, which is conventionally marked as the maximum of the signal. This $(\Delta R/R)_{max}$ corresponds to the hot electrons excitation which are measured throughout this work.

2.3.2 Measurement 2: Snapshots

In order to have a complete picture of the underlying physical processes, one also needs to record how these processes evolve in space. We should also recall that the processes related to surface plasmons, which we are interested in, have a propagative nature. For this reason, the time-resolved response of a single pixel in space does not carry sufficient information, as the reflectivity variations occurring outside this "pixel" are not detected. To gain insight into spatial information about the plasmon absorption and reflectivity change, we make use of an imaging system. In the experimental bench a scanning optical imaging system is

[4]The values are calculated considering Eq. (2.3) with N_{path} = 2, which is the case for our experiment.

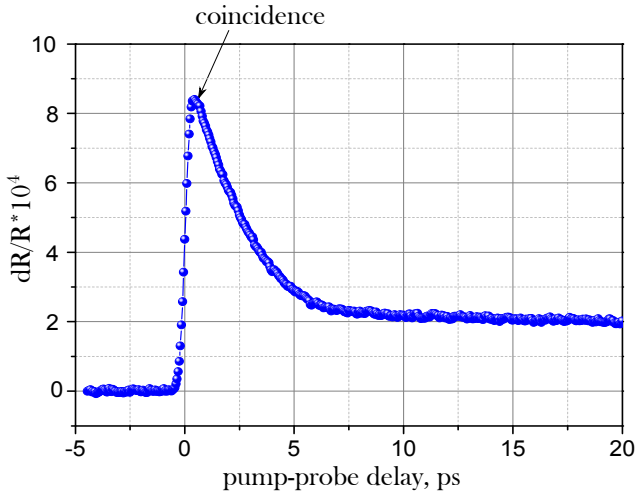

Figure 2.2: *Relative change of reflectivity of* 100 nm *thick gold film as a function of the pump-probe delay. The "coincidence" delay is conventionally marked as the maximum of the curve. The pump and probe beams wavelengths are respectively* 800 *and* 490 nm*. After a delay of* 20 ps *a* $\Delta R/R$ *is measured since the lattice is not yet cooled at this time-scale.*

integrated, where the probe beam raster scanns the surface of the sample. The detection of the reflected probe beam is synchronized with the scanner motion in order to obtain the signal for each pixel. In this way, we can reconstruct a map, in the sample plane, of the reflectivity variations.

To settle this imaging system, we have integrated an automated *scanning-mirror*: a flat mirror mounted on a dynamic two-axis mount that allows small, rapid, computer-controlled changes in the mirror's X and Y angles. We make use of an FSM-300 Fast Steering Mirror system (Newport) [91]. This system is composed of the mirror head (including the mirror carrier, flexure suspension, position sensors etc.) which works with a controller to produce the precise rotation and the characteristic speed of the components. The angular mechanical[5] range of the scanner is ±26.2 mrad (±1.5^o), with a resolution of less than 1 μrad. In this way the laser beam can be stabilized to less than single microradians; the high accuracy and position repeatability almost totally eliminate image blurring due to motion and far-field laser beam jitter.

The scanning mirror is coupled with an afocal system of two lenses and the

[5]Optical angular range is equal to twice the mechanical angular range

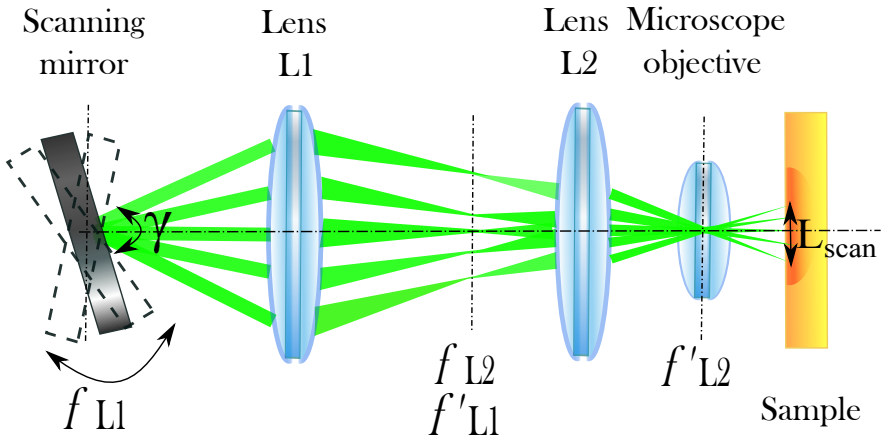

Figure 2.3: *Schematic representation of the optical imaging system. The center-point of the scanning mirror has to be conjugated with the object focal plane. For a microscope objective generally the entrance pupil plane corresponds to object focal plane, so we have conjugated the scanning-mirror plane with the microscope objective entrance pupil.*

microscope objective. The details of the imaging system are depicted in Fig. 2.3 and its complete characterization and validation is described in the thesis of G.Calbris [78]. For each particular angle γ, set for the scanner, and a particular microscope objective, corresponds a precise length L_{scan} scanned by the beam in the sample plane. As an example, for a microscope objective 50X (NA=0.45, focal distance f = 3.6 mm), setting an angle of scan γ = 10.48 mrad the length of scan in the sample plane represents $\approx 65\,\mu$m.

The spatial resolution of the images is imposed by the diffraction limit, i.e., is dictated by the size of the focus spot we use for a particular experiment. The focus size can be as small as a few hundreds of nanometers for a high numerical aperture microscope objective (e.g., for an oil immersion 100X objective with NA=1.5, in the blue-green spectral region the focus size can be $\approx$ 200 nm).

2.3.3 Measurement 3: Thermoreflectance movies

As we have previously shown, we are able to perform point-measurements and record the time-resolved $\Delta R/R$ response for a pump induced excitation. We are

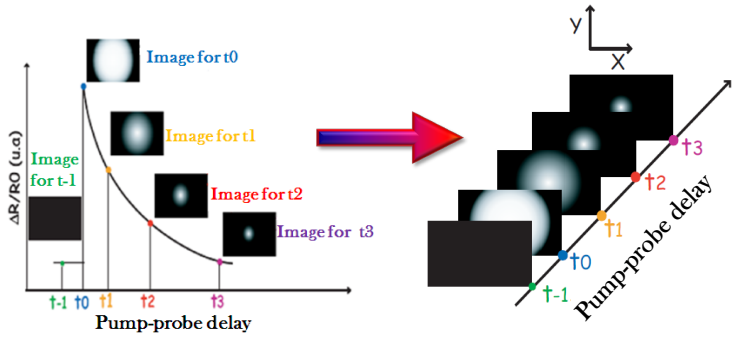

Figure 2.4: *Procedure of a reflectance movie reconstruction:* ***(a)*** *An image is acquired for each pump-probe delay (i.e., translation stage position)* ***(b)*** *The movie is reconstructed afterwards by attributing to each of the images the corresponding pump-probe delay.*

also capable of obtaining a map of reflectivity variations in space at a particular delay following the excitation. Combining the two types of measurements we can reconstruct the information both in space and time, i.e., we can record a thermoreflectance movie describing the entire process of hot electron excitation and their consequent relaxation.

The steps involved in the process of a complete spatio-temporal characterization are schematically depicted in Fig. 2.4. Firstly, an image is acquired for a fixed position of the translation stage. By consecutively increasing the delay between the pump and probe pulses, we record a map for each position of the translation stage. Finally, by attributing the corresponding pump-probe delay to each image we reconstruct, frame-by-frame, the movie.

An example of a set of consecutive frames, which are recorded at the specified pump-probe delay, is represented in Fig. 2.5. The images describe the electron-phonon thermalization process of a 100 nm thick gold film, excited by a red pump (λ = 800 nm, 0.5 mJ/cm^2) and probed by a green probe (λ = 532 nm, 0.3 mJ/cm^2).

2.4 General description of the experiment

We now provide a few details on the general functionality of the system for a better understanding. The overall scheme of the experimental set-up is presented in Fig. 2.6. Both the elements of the laser chain and other main bench components

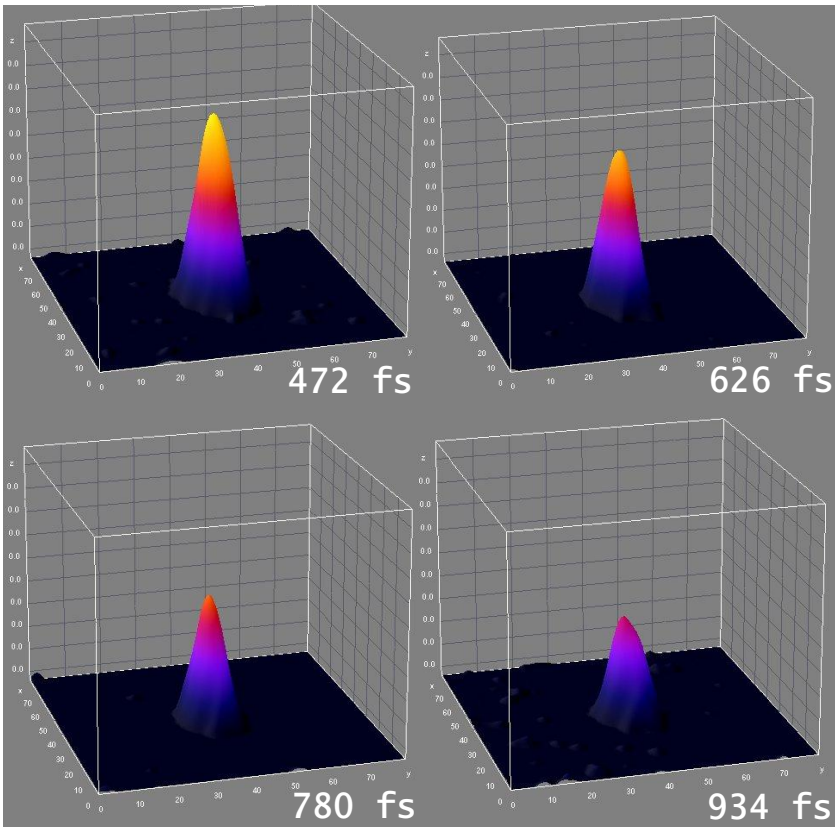

Figure 2.5: *Reflectance images of a* 100 nm *thick gold film, taken after the perturbation produced by a pump pulse, at four consecutive temporal delays. The delays are specified in the images. The pump and probe beams illuminate the sample from the same side and their wavelengths are* 800 *and* 532 nm*, respectively.*

have been previously described.

The laser chain is followed by a system of detachable mirrors, beam-splitters, lenses and other optical elements. The location of all optical components have been specifically designed in order to allow the switching between the trajectories of the three output beams. As we have mentioned previously, the pump and the probe beams optical paths have to be exactly the same at the position of the sample. For this reason, in all possible configurations and possible beam wavelengths and "role" (either pump, either probe) combinations, the lengths of all trajectories have been precisely adjusted.

The translation stage is integrated in the path of the probe beam. Both beams are finally injected in an inverted optical microscope, Olympus IX71, on which the sample is placed. In the microscope, we spatially recombine the

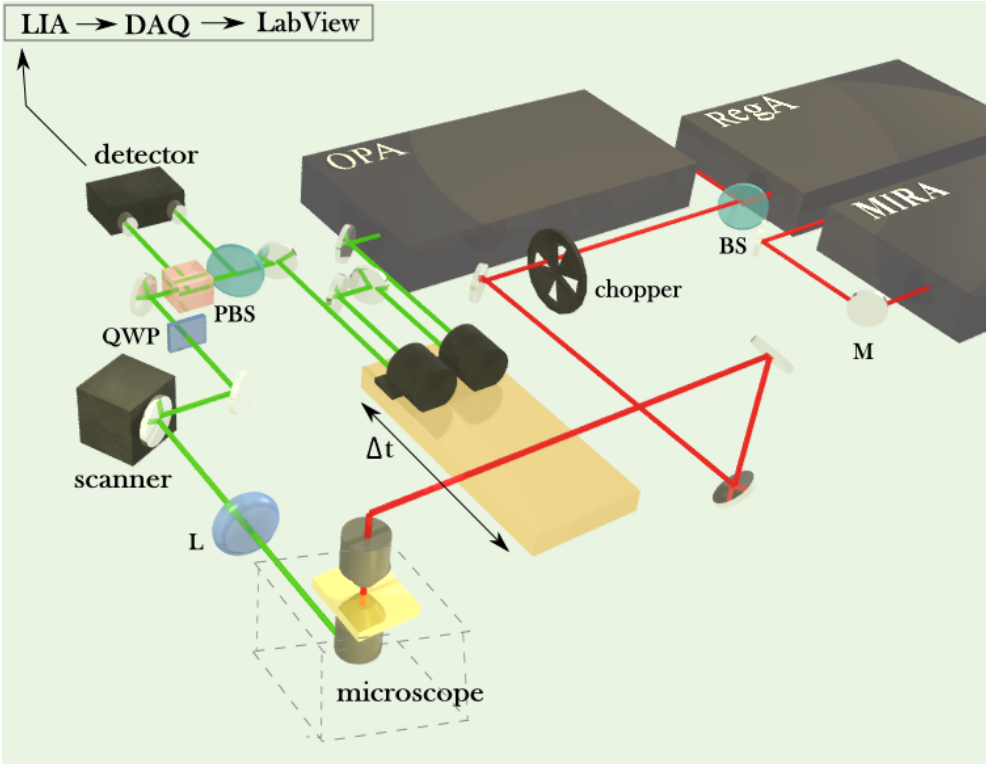

Figure 2.6: *Schematic representation of the entire experimental set-up. In the configuration presented here, pump and probe beams are incident from opposite sides on the sample and reflected light is detected. BS=beamsplitter; M=mirror; PBS= polarizing beamsplitter; QWP= quarter wave-plate; L=lens; LIA=lock-in amplifier; DAQ= data acquisition. Many optical components are not shown.*

two beams and we can easily switch between microscope objectives. We also use a bright-field lamp, incorporated with the microscope, and the microscope camera port to send the imaged sample region to a camera. The visualization system is important in our experiments as the objects of our study are micro-, sub-micro-metrical structures. Thus, we need to locate the structures and the beam's relative positions to them.

On the microscope we installed an automated XY Microscope Stage for Inverted Olympus Microscopes (PILine). This automated stage allows one to position, adjust and shift the sample in the XY-plane with sub-micrometrical resolution and repeatability steps. This microscope stage is driven by ultrasonic piezo-linear motors and it operates with a suitable controller.

Another important degree of freedom we control is the sample side from

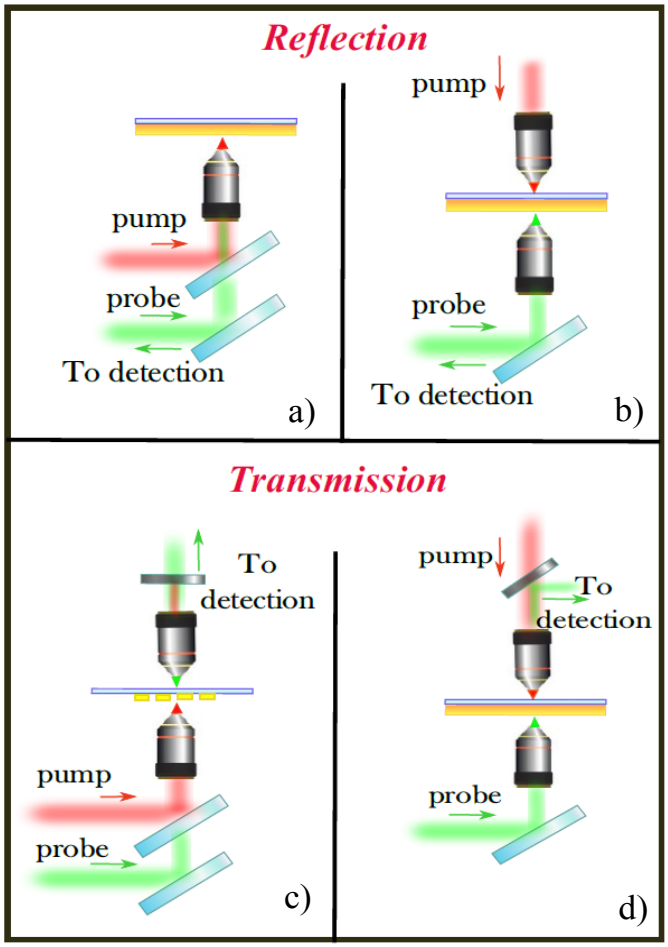

Figure 2.7: *Possible configurations of the pump-probe set-up:* ***(a)*** *Pump and probe beams are incident from the same side of the sample and the intensity of the reflected probe is collected.* ***(b)*** *Pump and probe beams are incident from the opposite sides of the sample and the intensity of the reflected probe is collected.* ***(c)****Pump and probe beams are incident from the same side of the sample, but the intensity of the transmitted probe is collected.* ***(d)****Pump and probe beams are incident from opposite sides of the sample and the intensity of the transmitted probe is collected.*

which we excite and probe the perturbation, as well as the detection of either reflected, or transmitted beam. From this point of view, there are four available configurations, which are summarized in Fig. 2.7.

In the reflection configuration, the reflected probe is taken with a polarizing beamsplitter from the back-probe path and sent to the detector. If we need to work in transmission, the transmitted part of the beam is collected by a second

microscope objective and focused after into an optical fiber, which is directly connected with the detector. However, all experimental results presented in this thesis are performed only for reflection configurations, displayed in Fig. 2.7(a,b).

The entire set-up is computer controlled with a LabView software, connected with a data acquisition card "National Instrument" PCI-6251 and a GPIB communication.

The home-made software allows the user to:

- drive the translation stage and thus to control the delay;
- set/read the X and Y voltage for the scanning mirror;
- simultaneously launch the reading of the reflected probe intensity and the displacement of the delay line;
- simultaneously launch the reading of the reflected probe intensity and the movements of the scanner.

The parameters for detection, number of registered points for every measurement, studied temporal range, speed of the translation stage, and lock-in settings are chosen according to the sample and the required acquisition time. To achieve a better signal to noise ratio, the measured signals are averaged. It is worth mentioning that for most of the results presented here, the signals are obtained by using a pump beam coming directly from RegA and the probe beam from OPA.

2.5 Conclusion

We have described in this chapter the experimental bench used throughout this work. It represents a femtosecond pump-probe experminet, allowing a tunability of wavelengths, integrating an optical imaging system, precise positioning and motion control of the sample, as well as several working configurations (reflection/transmission). This set-up allows us to measure the spatial and temporal evolution of $\Delta R/R$ which follow a pulsed perturbation, on a time scale ranging from fs to ns. The temporal resolution of the experiment is limited by the pulse duration ($\approx 150\,\text{fs}$), and the spatial resolution is dictated by the diffraction limit of light ($\approx 200\,\text{nm}$ in the blue-green spectral region).

Combining electronic differential detection and lock-in detection schemes we are able to detect pump-probe signals with relative amplitude variations of the order of 10^{-3} to 10^{-6}. All degrees of freedom implemented in the set-up allows one to adjust all the necessary parameters of the detection (i.e., wavelength, time-scales, temporal/spatial response etc.) in order to measure the information of interest.

CHAPTER 3

Reavealing surface plasmon absorption around subwavelength structures

This chapter is the first demonstration of the capability of thermoreflectance to image the power density dissipation (absorption) by plasmons along their propagation. We started by investigating the surface plasmon absorption around a simple and canonical structure such as a sub-wavelength slit. Theoretical calculations (from Philippe Lalanne group) have shown that diffraction from a slit produces a rather complex absorption profile, characterized by an unexpected plateau profile. In contrast to our general belief that the intensity of waves, created by local sources, should decrease with the distance, we reveal that the dissipated heat at the surface of the metal remains constant over a broad spatial interval of a few tens of wavelengths. This complex absorption profile served to validate thermoreflectance and to prove that by measuring the plasmon-excited hot electrons we do measure the absorbed plasmon energy. This chapter describes a one year work during which we designed and engineered the sample in order to extract the tiny contribution of plasmon heating compared to huge amount of heat deposited by the excitation laser. The major results of this chapter have been published into a letter [2].

Contents

3.1 Introduction

Nearly 16 years ago [92] it was shown that holes or slits etched in a metal film can generate surface plasmon polaritons (SPPs) when illuminated by light of wavelength greater than the aperture size. The diffraction and scattering by such apertures in metal films is a fundamental phenomenon of wave physics with a long history [93]. In recent years, the topic has become a subject of renewed interest due to its importance in modern sciences and techniques ranging from sub-wavelength optics and optoelectronics to chemical sensing and biophysics [94–101]. Current efforts are mostly focused on developing these apertures as "plasmon launchers" but so far, little is presently known about the heat dissipated by the electromagnetic field in the metal surface near the holes or slits.

In general, it is expected that the intensity of the waves created by local sources should decrease continuously with the distance from the sources [102]. However in this chapter, we present a remarkably simple case that invalidates this intuition. This occurs for the field scattered by isolated sub-wavelength apertures on the surface of noble metal films at near infrared frequencies ($\lambda \geq 0.8\,\mu$m). Thus, the dissipated heat at the surface remains constant over a broad spatial interval of a few tens of wavelengths.

This behavior was firstly predicted by numerical calculations. In addition, an analytical model was developed which completes the understanding, explains the origins of a constant absorption and further highlights the complex role played by plasmons and quasi-cylindrical waves in the revealed phenomenon. The anomalous absorption profile around a single sub-wavelength slit was possible to observe with non-intrusive pump-probe reflectance measurements and by developing a special sample design. The absorbed energy of the surface waves is brought in evidence by probing the hot-electron gas temperature at femtosecond time scales. Additionally, computational results reveal that the absorption plateau is an intrinsic property that occurs for a large variety of topologies, regardless of aperture shapes.

3.2 Calculation of the absorption profile

3.2.1 Prediction by numerical simulations

The absorption profile around sub-λ apertures depends on the spatial shape of the heat source. In the case the aperture generate SPPs, the absorbed electromagnetic surface wave produces a heat source. Thus, the absorbed energy is directly related to the electromagnetic field and power density of the launched SPP.

In the following calculations, the relevant quantity which is calculated and described is the ***absorbed power density*** A ($\mathrm{W/m^3}$), conventionally called ***absorption*** henceforth.

In order to define the absorption, we first consider the surface plasmon excited at the metal/dielectric interface. As the plasmon represents a collective excitation of the electrons in metal, we consider a charge distribution in the metal, characterized by the charge density ρ and the current density $\boldsymbol{J}$. The charges of a volume element dV of the distribution are subjected to Lorentz force:

$$\mathbf{F} = \rho(\mathbf{E} + \mathbf{v} \times \mathbf{B})dV. \tag{3.1}$$

The magnetic force does not work, and in this case the electromagnetic power $\mathcal{P}$ supplied to the charges of a volume element dV is expressed as:

$$\delta\mathcal{P} = \rho\mathbf{v} \cdot \mathbf{E}dV = \mathbf{E} \cdot \mathbf{J}dV. \tag{3.2}$$

Integrating over entire volume V, we obtain the power supplied by the electromagnetic field source (SPPs in our case) to the ensemble of charges

$$\mathcal{P} = \int_V \mathbf{E} \cdot \mathbf{J}dV. \tag{3.3}$$

Our goal is to link the absorption with the electromagnetic field intensity. For this we recall that the current density is linked with the polarization as $\boldsymbol{J} = \partial\mathbf{P}/\partial t$. Thus, we can write the absorbed power density as the average electromagnetic

power *absorbed* by a volume V of a material:

$$A = \langle \mathbf{E} \cdot \mathbf{J} \rangle_t = \frac{1}{2}\mathrm{Re}\left\{\mathbf{E_0} \cdot (-i\omega \mathbf{P_0}^*)\right\} = \frac{1}{2}\omega\epsilon_0 \mathrm{Re}\left\{(-i\chi)^*\right\} \|\mathbf{E_0}\|^2 = \frac{1}{2}\omega\epsilon_0\chi'' \|\mathbf{E_0}\|^2 , \tag{3.4}$$

where ω is the frequency of the electromagnetic field, ϵ_0 denotes the vacuum permittivity, χ and χ'' stand for the material susceptibility and its imaginary part respectively. Considering that $\epsilon_0\chi'' = \epsilon''$ (with ϵ being the material relative permittivity) we can finally define the absorption as:

$$A = \frac{1}{2}\omega\epsilon'' \|\mathbf{E_0}\|^2 . \tag{3.5}$$

According to Eq.(3.5) absorption in our case is defined as the imaginary part of the permittivity times the field intensity, for a given frequency.

The calculations of the absorption profile around sub-wavelength slits presented in this chapter have been performed by Mathias Perrin[1] and Philippe Lalanne[2] in the frame of a collaboration. We will briefly present the main steps of the calculation and will bring in evidence the important calculation results.

In order to compute the heat source profile, numerical simulation has been carried out using a fully-vectorial aperiodic-Fourier-modal method [103–105]. The aperiodic Fourier modal method is a generalization of the Rigorous Coupled Wave Analysis [106], which relies on an analytical integration of Maxwell's equations along one direction and on a supercell approach with perfectly matched layers in the two other transverse directions.

We consider a slit aperture in a gold film with the axes defined as in Fig. 3.1 illuminated by the fundamental TM slit mode. For the values of the gold permittivity ϵ_m tabulated in [107], the electric field $\mathbf{E}(x, z)$ scattered by a slit aperture is calculated. Figure 3.1(a) shows the distribution inside the gold film depth of the absorbed power density $A(x, z)$ in the metal calculated with Eq.(3.5). The presented numerical simulation were performed by considering a slit width of $w = 300\,\mathrm{nm}$, and an incident plane wave having $\lambda = 0.8\,\mu\mathrm{m}$. As our objective (at least ideally) was to consider all the absorption in the metal, the next step would

[1] Laboratoire Onde et Matière d'Aquitaine (LOMA), CNRS-Université de Bordeaux.

[2] Laboratoire Photonique, Numérique et Nanosciences (LP2N), Institut d'Optique d'Aquitaine.

be the computation of the vertically-integrated absorption profile

$$A(x) = \int A(x,z)dz. \tag{3.6}$$

For this reason, we performed an integration over the 110 nm thick layer (≈ 10 skin depths at $\lambda = 0.8\,\mu$m) of the absorption profile $A(x,z)$ computed in Fig. 3.1(a).

The obtained profile $A(x)$ is plotted in Fig. 3.1(b) (continuous red curve). We remark that the profile $A(x)$ displays a plateau that is almost constant over a $10\mu m$ spatial interval. The same calculations have been performed for other wavelengths, see Fig. 3.1(b). The plateau size is found to increase with the icreasing wavelength, to reach a size of 70λ at $\lambda = 1.5\,\mu$m. In the visible spectrum range for $\lambda \leq 0.7\,\mu$m, $A(x)$ rapidly decreases with increasing distance from the slit and no plateau is observed. For $\lambda \geq 1.5\,\mu$m, most of the energy is dissipated in the immediate vicinity of the slit, and the plateau is still observed but for very weak absorptions.

In the following it is assumed that all fields should be identical to those launched by a line source when far enough from the slit. From the computed total scattered field $\mathbf{E}(x,z)$, we extract the electric field $\mathbf{E}_{\mathrm{SPP}}(x,z)$ of the SPPs that are launched on each side of the slit [108], to further compute the SPP-absorption profile $A_{\mathrm{SPP}}(x) = \frac{1}{2}\omega \int \epsilon''_m \left\|\mathbf{E}_{\mathrm{SPP}}(x,z)\right\|^2 dz$ that would be absorbed if the electromagnetic field in the metal would only be composed of SPPs. $A_{\mathrm{SPP}}(x)$ is shown with red-dashed curves in Fig. 3.1(b) and as expected, decreases exponentially with x. At long distances from the slit, $A(x) \approx A_{\mathrm{SPP}}(x)$, which implies that the absorption is mainly due to the launched SPPs. In the plateau area, however, we note that the actual absorption is substantially smaller than that of the SPP, implying that *only a fraction of the scattered SPP field is actually dissipated as heat.*

At first, the constant absorption came as a surprise. The absorption is proportional to the SPP intensity, so one would expect it to decrease (exponentially) with distance from the slit source. In order to gain physical insight into this anomalous behavior and to understand how the plateaus vary with material parameters and wavelength, we developed an analytical model to explain qualitatively the origin of the observed absorption plateau.

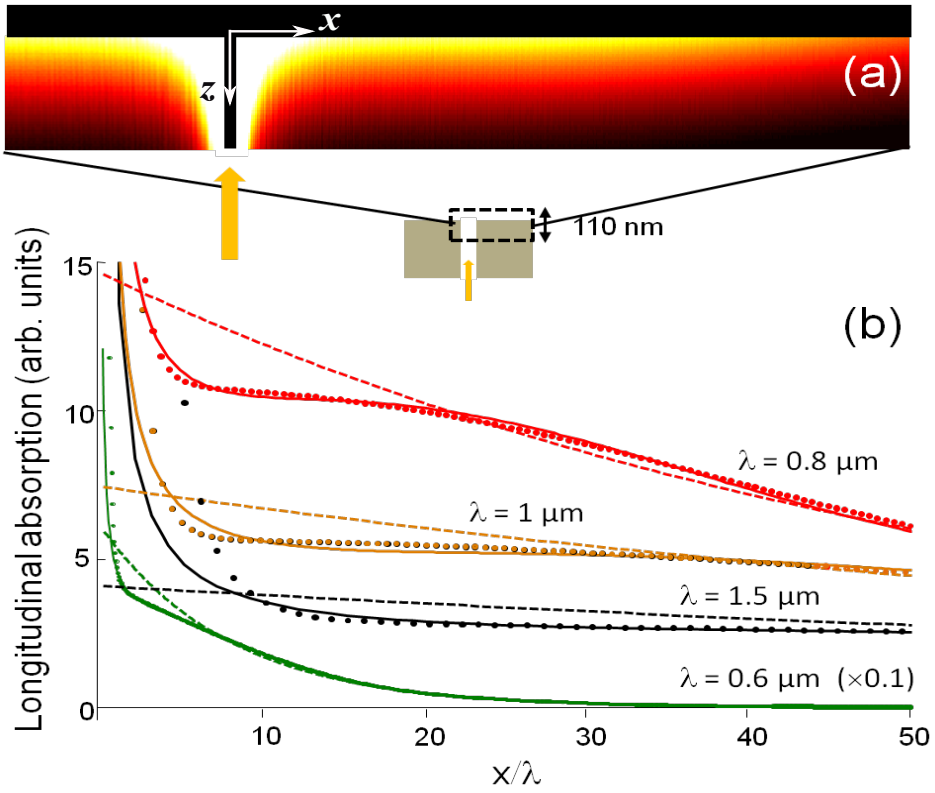

Figure 3.1: *Computed results obtained for the absorption at a gold/air interface illuminated by the fundamental TM mode of a 300 nm width slit.* ***(a)*** *Absorbed power density $A(x,z)$ in a linear scale.* ***(b)*** *The solid curves represent the absorption profile $A(x) = \int A(x,z)dz$. The red-dashed curve represents the absorption profile $A_{\mathrm{SPP}}(x)$, which would be achieved if the metal field was only composed of two SPPs launched in opposite directions. Results are presented for several wavelengths and for the same slit-width-to-wavelength ratios. The red dots are fitted data, using Eq.(3.10).*

3.2.2 Prediction by analytical modeling

In previous works, Lalanne and his collaborators have shown both theoretically and experimentally [108, 109] that sub-wavelength slits produce not only SPPs, but also another type of diffraction light waves, called quasi-cylindrical waves (CWs) [110]. Quasi-cylindrical waves are diffraction waves generated by the slit, which propagate in all directions above the film with nearly cylindrical wave fronts and with a wavelength almost equal to that of the SPPs. It is found that they play an important role in the case of sub-wavelength apertures and their contributions give rise to new physics that can be exploited. Recently,

[111] has been also explicitly shown the role of CWs in the extraordinary optical transmission (EOT)[3] phenomena [92].

Based on this, in our investigation of absorption around sub-wavelength apertures, we adopt the dual-wave picture and assume that the electromagnetic field scattered by the slit is composed of SPPs and quasi-cylindrical waves. The two waves are emitted with their own amplitude and phase, depending in particular on the shape of the scatterer. Then they decrease (SPP, exponentially and CW, algebraically), when going away, along the interface.

Accurate analytical expressions obtained by integration in the complex plane are known in the literature both for the quasi-cylindrical waves and SPPs [110]. The electric field components $[\mathbf{E}_x, \mathbf{E}_z]$ of each wave excited in the noble metal, under the condition $z << x$, can be written as:

$$\mathbf{E}_{\mathrm{SPP}} = E^0_{\mathrm{SPP}} exp(ikn_{\mathrm{SPP}}x - ik\chi_{\mathrm{SPP}}z)[\chi_{\mathrm{SPP}}, n_{\mathrm{SPP}}], \tag{3.7a}$$

$$\mathbf{E}_{\mathrm{CW}} = E^0_{\mathrm{CW}} W(2\pi\gamma x)/x^{3/2} exp(ikn_{\mathrm{CW}}x - ik\chi_{\mathrm{CW}}z)[\chi_{\mathrm{CW}}, n_{\mathrm{CW}}], \tag{3.7b}$$

for the the SPP field and quasi-cylindrical waves, respectively. In the previous equations, $k = \omega/c$ is the wave-vector modulus, ϵ_d is the permittivity of the dielectric, $n_{\mathrm{SPP}} = (1/\epsilon_m + 1/\epsilon_d)^{-1/2}$ and $n_{\mathrm{CW}} = (\epsilon_d)^{1/2}$ are the normalized propagation constants of the SPP and quasi-cylindrical waves. Both complex factors E^0_{SPP} and E^0_{CW} give the amplitude and phase of the SPP and CW emitted by the scatterer. The function $W(2\pi\gamma x)/x^{3/2}$ describes the algebraic decay of the CW (see [110] for more details). The other coefficients are defined as:

$$\chi_{\mathrm{SPP}} = \left(\epsilon_m - (n_{\mathrm{SPP}})^2\right)^{1/2},\ \chi_{\mathrm{CW}} = (\epsilon_m - \epsilon_d)^{1/2}, \text{ and } \gamma = n_{\mathrm{SPP}} - n_{\mathrm{CW}}. \tag{3.8}$$

It is important to note that, for good metals, since the refractive index of the metal is much higher compared to the dielectric one ($|n_m| >> |n_d|$), we can approximate that $\chi_{\mathrm{SPP}} \approx \chi_{\mathrm{CW}}$ and $n_{\mathrm{SPP}} \approx n_{\mathrm{CW}}$. Based on these approximations, it is straightforward to show that the vertically integrated total absorption profile:

$$A(x) = \frac{1}{2}\omega\epsilon''_m \int \left\|\mathbf{E}_{\mathrm{SPP}}(x,z) + \mathbf{E}_{\mathrm{CW}}(x,z)\right\|^2 dz, \tag{3.9}$$

[3]Extraordinary optical transmission represents the greatly enhanced transmission of light through a sub-wavelength aperture in an otherwise opaque metallic film which has been patterned with a regularly repeating periodic structure.

can be written as:

$$A(x) \approx A_{\mathrm{SPP}}(x)\left[1+2\sqrt{\frac{A_{\mathrm{CW}}(x)}{A_{\mathrm{SPP}}(x)}}\cos(\mathrm{Re}(kn_{\mathrm{SPP}}-kn_{\mathrm{CW}})x+\alpha)\right]+A_{\mathrm{CW}}(x). \tag{3.10}$$

In this expression $A_{\mathrm{SPP}}(x) = \frac{1}{2}\omega\epsilon_m'' \int \|\mathbf{E}_{\mathrm{SPP}}(x)\|^2 dz$ is the exponentially decaying absorption due to the SPP, and $A_{\mathrm{CW}}(x) = \frac{1}{2}\omega\epsilon_m'' \int \|\mathbf{E}_{\mathrm{CW}}(x)\|^2 dz$ is the algebraically decaying absorption due to the quasi-cylindrical wave, which can be neglected a few wavelengths away from the slit. The real number α represents the relative phase between SPP and CW, which varies slowly in space (with x).

From Eq.(3.10) one can see that the total absorption $A(x)$ consists of not only the absorptions both of SPPs and CWs, but also a beating term of the two waves is present, which depends on the relative phase α between them . The "anomalous" absorption profile is thus understood as resulting from a background term, the SPP absorption $A_{\mathrm{SPP}}(x)$, over which an oscillatory term is imprinted with a spatial frequency that results from the beating of a SPP and a quasi-cylindrical wave. In other words, the calculations show that the CWs destructively interfere with the SPPs, and with a diminished SPP intensity, there is less for the gold to absorb. The interference effect is strongest closer to the slit and fades away by about 15 μm, as the CWs intensity decreases relative to the SPPs.

A fitting procedure between the developed analytical model and the numerical data obtained with the aperiodic Fourier modal method is carried out. For this, $A_{\mathrm{SPP}}(0)$, $A_{\mathrm{CW}}(0)$ and α are the three real independent parameters that are fitted. During the fitting procedure, the decaying form of the two waves is exploited. At large distances away from the slit, the absorption decay is mainly due to the plasmon, while the quasi-cylindrical field is negligible. Working in this range the *numerically calculated* absorption decay is fitted with an exponential decay and in this way the coefficient $A_{\mathrm{SPP}}(0)$ is calculated first. Afterward, finding the two other real coefficients, $A_{\mathrm{CW}}(0)$ and α, with a least square method does not produce any numerical uncertainty. The red dots in Fig. 3.1(b) (superimposed with red curve) are fitted values computed from Eq.(3.10). For all wavelengths, they well match the numerical data. Despite its simplicity, the analytical model well predicts all the salient features of the absorption profile: the initial rapid decrease followed by a plateau, and the exponential decrease at large separation

distances.

Noting that the plateau length L is approximately given by half the beating period, we obtain a very simple expression for L:

$$\frac{L}{\lambda} = \frac{\pi}{2\mathrm{Re}(n_{\mathrm{SPP}} - n_{\mathrm{CW}})} \approx \mathrm{Re}\left(\frac{\epsilon_m}{\epsilon_d^{3/2}}\right). \tag{3.11}$$

We have verified numerically that Eq.(3.11) represents a very good approximation of the plateau size for $0.8\,\mu\mathrm{m} < \lambda < 1.5\,\mu\mathrm{m}$, for various dielectrics ($\epsilon_d = 1;\ 2.25;\ 4$), and for noble metals (gold, silver).

For the sake of generalization, point source (instead of line source) scatterers are also investigated. Instead of a specific geometry such as a nano-hole in a metal film, we rather considered electric dipole sources located just above a flat gold surface and calculated the absorbed power-density profile:

$$A(\rho,\theta) = \frac{1}{2}\omega \int \epsilon_m'' \left\|\mathbf{E}(\rho,\theta,z)\right\|^2 dz, \tag{3.12}$$

radiated by the sources in the metal (ρ and θ denotes the radius and the azimuth in cylindrical coordinates). $A(\rho,\theta)$ is shown in Fig. 3.2(a) for two dipole sources emitting at $\lambda = 0.8\,\mu\mathrm{m}$, respectively polarized perpendicularly and parallel to the surface along the x-axis. In Fig. 3.2(b), the solid curves represent $\rho A(\rho,\theta)$, a quantity directly proportional to the absorption of the surface element $\rho d\rho d\theta$ located at polar coordinate $(\rho,\theta\ )$, as a function of ρ for a dipole parallel to the surface and for four values of θ, $\theta = \pi/6,\ \pi/4,\ 2\pi/5$, and $\pi/2$. Remarkably, all curves exhibit a large plateau.

The same conclusion holds for the azimuthally-averaged absorption:

$$A(\rho) = \int A(\rho,\theta)d\theta/2\pi, \tag{3.13}$$

of an elementary ring of radius ρ (see the circles in the Fig. 3.2(b)). Virtually identical results (upon rescaling) are obtained for the perpendicular polarization. We finally note that the absorption profiles $A(\rho)$ in Fig. 3.2(b) and $A(x)$ in Fig. 3.1(b), which are obtained for point and line sources respectively, are virtually superimposed when rescaled and plotted on the same graph at $\lambda = 0.6, 0.8, 1$ and $1.5\,\mu\mathrm{m}$ (see the dotted-blue curve and the associated circles

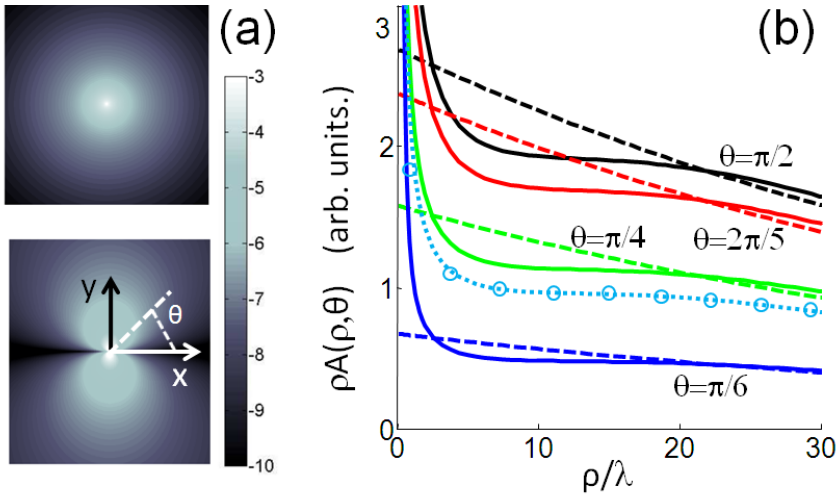

Figure 3.2: *Absorbtion at a gold-air interface illuminated by a point dipole source located at $x = y = 0$, just above the metal plane and emitting at $\lambda = 800nm$. **(a)** Absorbtion $A(\rho, \theta)$ for a dipole perpendicular (upper panel) or parallel (lower panel) to the surface and oriented along the x axis. **(b)** Solid curves: $\rho A(\rho, \theta)$ for several θ. The dashed curves correspond to the associated SPP absorbtion $\rho A_{\mathrm{SPP}}(\rho, \theta)$. The dotted-light-blue curve represents the azimuthally-averaged absorbance $A(\rho)$. It is virtually superimposed with the circles that represent the absorption profile $A(x)$ of the slit (red curve in Fig. 3.1(b)) after vertical rescaling.*

in Fig. 3.2(b)). This leads us to the finding that the *anomalous absorption is a general property of sub-wavelength apertures in metal films.*

To conclude, the above calculations are the first to provide some understanding of the heat dissipated by the electromagnetic field in the metal surface around the aperture. Actually, we show that, as it propagates away from the slit, this field heats the metal and paradoxically the heat dissipated at the surface remains constant over a broad spatial range of several tens of wavelengths. The phenomenon is general since the same absorption plateau occurs for a variety of topologies, irrespective of whether the aperture shape corresponds to one-dimensional line (slit) or point-like (hole) sources. It is well predicted by a simple analytical model based on recent works [110, 112] that describe the field radiated on metal surfaces as a superposition of two waves, a surface-plasmon polaritons and a quasi-cylindrical wave. The model additionally shows that the heat dissipated in the plateau area is actually weaker than the heat deposited by the plasmon launched on the surface. This highlights the intricate role played by

the quasi-cylindrical wave at the metal surface.

3.3 Experiment

3.3.1 Experimental description

The knowledge of the heat dissipated (the local heat source term in the thermal diffusion equation) in miniaturized plasmonic devices is of fundamental importance. It is not easy to predict the heat dissipated with electromagnetic calculations of the absorption $A \propto \epsilon_m'' \left\|\mathbf{E_0}\right\|^2$, simply because calculations neglect grain roughness or crevasses, which are crucial in the absorption process especially for highly-confined plasmons. The measurement of the heat dissipated is also a difficult task. In particular we note that low resolution techniques, such as those reviewed in Ref. [1], provide temporally- and spatially-broadened versions of the local heat source because of the phonon diffusion transport in the metal. Ideally to measure the local heat source term in the thermal diffusion equation, one should be able to detect the generated electron-hole pairs. Here we use the pump-probe technique described in Chapter 2. The SPP-to-hot electron conversion is measured by launching 150 fs SPP pulses into a slit aperture, and by probing the permittivity variations induced by the hot-electron gas. The variations that are collected a few hundreds femtoseconds after the plasmon absorption, are expected to provide faithful (with a weak broadening) images of the local heat source or equivalently of the density of the electron-hole pairs.

As mentioned in the beginning of this chapter, our interests lie in revealing the absorption around a sub-wavelength slit in a gold film. For this we use femtosecond pump-probe reflectance set-up, described in Chapter 2, and we perform the experiment schematically depicted in Fig. 3.3. The sample represents a nanoslit in a gold layer, deposited on a glass substrate. The slit is illuminated from the rear glass/gold interface (in the following called "back" interface) with the first, "pump" laser. The pump pulse (λ = 800 nm, 150 fs full-width-at-half-maximum) is slightly focused on the rear interface (to have an almost plane wave incident on the slit). The polarization can be set either parallel (TE) or perpendicular (TM) to the slit. The incident light is dominantly reflected or absorbed. Only a small fraction of the incident energy is funneled through the slit. At the front

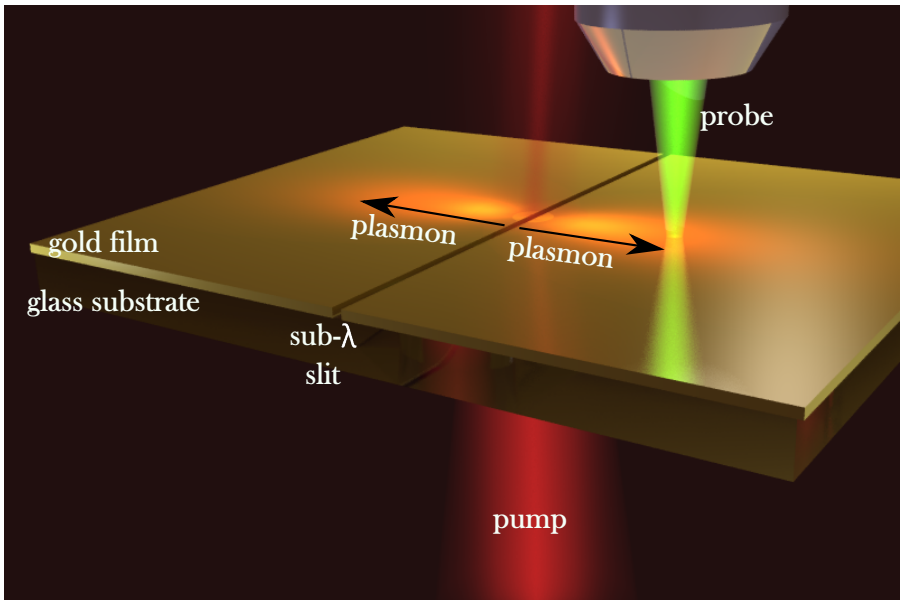

Figure 3.3: *Sketch of the slit-experiment: A first laser pump pulse (λ = 800 nm) is slightly focused on the rear interface. A second laser pulse (λ = 532 nm) probes the gold/air interface and records the reflectance variations ΔR with a controlled delay between the pump and the probe pulses.*

aperture, light is either diffracted in the far field or converted into surface waves (SPPs and CWs) at the gold/air interface (in the following called "front" interface). The surface waves propagate outward, perpendicular to the slit direction. As the waves die out and are absorbed by the metal, their heating is enough to affect the ability of the surface to reflect light.

To measure the absorbed plasmon power on the top interface, we raster scan the front surface of the sample with the second "probe" beam. The probe laser pulse (λ = 532 nm, 150 fs FWHM) probes the gold/air interface and records the reflectance variations ΔR with a controlled delay between the pump and the probe pulses. The reflectance map of the gold/air interface should represent the absorption profile of the dissipated surface waves at this interface. We have chosen to probe at λ = 532 nm $\approx$ 2.3 eV since at this wavelength we optically probe the electronic states slightly below the Fermi level in gold (2.38 eV). In this case, the effect of heating is to cause an increase in absorption/decrease in reflectivity (see Fig. 1.6).

3.3.2 Preliminary estimation of some experimental constraints

The characteristic time and space scales related to surface waves must first be understood and compared to those related to the heat diffusion phenomena. For this reason, we start with a few preliminary estimates of the time and space scales involved and compare them to our experimental possibilities.

3.3.2.1 Transverse heat diffusion

In the pump-probe experiment, when a pump pulse is incident on the rear sample side, it deposits an enormous amount of energy. Once it impinges on the slit, a part($\approx 1-3\%$) of this energy will eventually be coupled in surface plasmons[4], but the major part of the deposited energy will be transformed into a heat flux propagating from back to front metal interfaces. The challenge of this experiment is to image the plasmon heat source through variation of temperature in the time-frame before heat diffusion starts. So it is necessary to take into account some temporal and spatial considerations. If we want to detect only the heat deposited on the front interface, the heat coming from the rear side should be blocked. For that, we take advantage of the fact that phonons propagate much slower than light. More specifically, one should compare the time of flight T_{SPP} of the electromagnetic mode in the slit with the diffusion time T_{ph} of the phonons that are generated on the rear (pump) side of the sample and that scatter up to the top (probe) side.

Due to this consideration, we estimated the time of flight of the surface waves and compare it to heat diffusion speed. We consider a distance of 100 nm, which is on the order of the gold film thickness. Thus, our temporal requirement is given by the fact that the phonons time of flight should be greater than propagation time of surface waves:

$$T_{\mathrm{ph}} >> T_{\mathrm{SPP}}. \tag{3.14}$$

Time taken by phonons to pass through the gold is described by the characteristic

[4]Throughout this chapter using *plasmons* we address both plasmons and quasi-cylindrical waves.

thermal diffusivity process and is given by

$$T_{\mathrm{ph}} = \frac{d^2}{D_{\mathrm{TH}}}, \tag{3.15}$$

where d is the thickness of the gold film, D_{TH} is the thermal diffusivity, which for gold is $1.27 \cdot 10^{-4}\,\mathrm{m^2/s}$. From the Eq. (3.15), we estimate that the heat flux will diffuse from the rear side of the gold film to the front side in $T_{\mathrm{ph}} \approx 80\,\mathrm{ps}$.

The same distance is crossed by SPPs in an interval of

$$T_{\mathrm{SPP}} \approx \frac{d}{c}, \tag{3.16}$$

where c is the speed of the slit mode, which is almost equal to the speed of light ($c = 3 \cdot 10^8\,\mathrm{m/s}$). According to Eq. (3.16) we find that the deposited pump energy will funnel through the slit over a distance $d = 100\,\mathrm{nm}$ in $T_{\mathrm{SPP}} \approx = 0.33\,\mathrm{fs}$.

Therefore, the time of flight of phonons from the back to front surface of the sample is 3 orders of magnitude larger than the time it takes for the plasmon energy to funnel through the slit, and by probing the front surface of the sample at pump-probe delays of a few hundreds fs, one should not be contaminated by the heat flux deposited by the pump on the rear sample side.

3.3.2.2 Lateral heat diffusion

Regarding the heat transport, there will also be some along the film due to strong absorption inside the slit, which also contributes to the heating and reflectivity change. We estimate the size of this in-plane heat diffusion at some reference time-scale, and we see if the diffusion length may affect the plasmon-induced heat profile.

With respect to our experiment, we are able to detect absorption due to surface waves only if the size of the heat source is considerably larger than phonon diffusion length in the sample plane. We can estimate this length since for a certain pump-probe delay, a certain value of diffusion length is associated. For a pump-probe delay of $T_{\mathrm{delay}} \approx 500\,\mathrm{fs}$ (the choice of the respective delay is specified in one of the following sections), using the same equations for phonon diffusion (Eq. 3.15), we estimate that the heat flux will diffuse horizontally over a distance of $L_{\mathrm{ph}} \approx \sqrt{D_{\mathrm{TH}} \cdot T_{\mathrm{delay}}} \approx 8\,\mathrm{nm}$. On the other hand, within 500 fs, the SPPs will

propagate a distance of $L_{\mathrm{SPP}} = T_{\mathrm{delay}} \cdot c \approx 150\,\mu$m along the interface.

From these calculations we conclude that at short time, the measured temperature profile fits the SPP absorption profile in the metal. The "speed" of the phonon flux diffusing in the plane is not comparable at all with the speed of light.

Finally, by estimating the characteristic time of flight and diffusion lengths for the plasmon and phonons, we conclude that the existence of a *temporal resolution* is crucial for this experiment. We need to employ femtosecond pulses to probe before any heat diffusion starts, since at longer time scales, this heat could entirely cover the signal we are interested in.

3.4 Ultrafast heat transfer phenomena in homogenous gold films

3.4.1 Sample fabrication and description

Fabrication of sub-wavelength structures imply a complex and multi-step process. These steps are depicted in Fig. 3.4(a) and the entire process could be summarized in the following operations:

1. The glass substrate is subjected to a wet chemical cleaning, later on Ti-adhesion (3 nm) and Au (150 nm) layers are sputtered on the substrate by electron beam evaporation.

2. On the top gold film, PMMA (polymethyl methacrylate) electron-beam resist is deposited by spin coating.

3. We continue by nanopatterning the PMMA resist using electron-beam lithography.

4. The slits are etched with ion beam etching using ACP (Aerosol Collector Pyrolyser) Ar ion source.

5. The last step of the fabrication process is the wet removal of the PMMA electron-beam resist.

Following this procedure, slits with different widths from $w = 250$ to 650 nm, with a 50 nm step were fabricated. An image of a typical fabricated slit-structure,

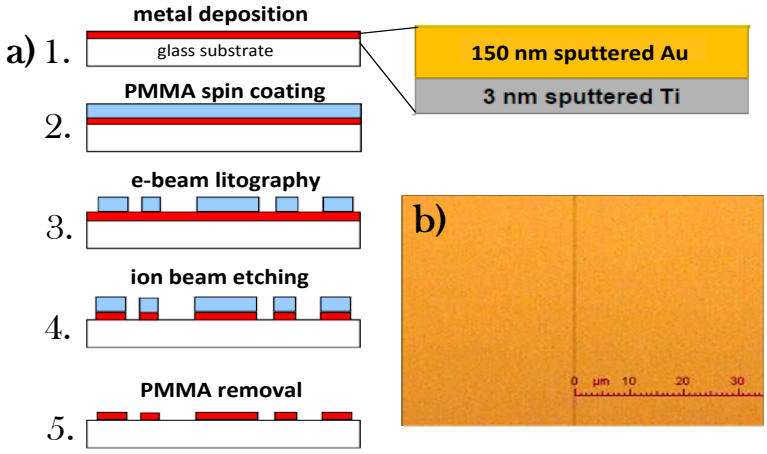

Figure 3.4: *Sample fabrication:* ***(a)*** *Multi-step sample fabrication process: bi-layer deposition, PMMA resist deposition, nanopaterning, ion beam etching and finally PMMA resist removal;* ***(b)*** *Microscope image of a fabricated* $500nm \times 200\mu m$ *slit.*

recorded with an optical microscope, is shown in Fig. 3.4(b). One can see a single 500 nm × 200 μm slit, fabricated with the process described above. The samples have been fabricated by Buntha Ea-Kim at Laboratoire Charles Fabry, CNRS-IOGS-Université Paris XI in Palaiseau, France.

3.4.2 Results

We carry out the experiment sketched in Fig. 3.3. Performing the above experiment, a pump beam (10x objective, beam waist $\approx 7\,\mu$m, $\lambda = 800$ nm) is incident on the rear sample side. The probe beam (50x objective, beam waist $\approx 2.5\,\mu$m, $\lambda = 532$ nm) raster scans the front gold/air interface at 500 fs pump-probe delay.

It is important to understand the reason behind choosing to probe at the characteristic 500 fs pump-probe delay. In Chapter 1, we have described that the absorption of ultrashort pulses by metal films is described as a multi-step process with different time scales [113, 114]. First, the energy is absorbed by the free electron gas, which is much lighter and more reactive than the ion lattice and thermalize very rapidly towards the equilibrium Fermi-Dirac distribution with a time scale of *few hundreds* fs. Then, the hot electron gas relaxes through internal electron-phonon collisions characterized by a time scale of *a few* ps, before a classic heat diffusion transport takes place with a much longer characteristic time. The *500 fs* pump-probe delay corresponds to an internally thermalized electron

gas (for gold), which is not yet cooled down with the lattice. The electrons are out of the equilibrium and they are "hot", while the lattice is still cold, so that all the absorbed energy is stored in the excited hot electrons.

In Fig. 3.5 the reflectance maps recorded in the above configuration are presented[5]. In Fig. 3.5(a) (with the corresponding averaged profile in Fig. 3.5(b)), the reflectance map of a $15 \times 15 \mu m^2$ area is presented, when the pump beam is focused on a slit-free gold film (sketch in Fig. 3.5(c)). The reflectance map is recorded at 500 fs pump-probe delay. We record a similar snapshot while focusing our pump-laser onto the slit, (see Fig. 3.5(d)) and its corresponding profile in Fig. 3.5(e). However in this case, the Gaussian shape presents a feature of a "cut" at the position of the slit (the slit-structure is not well centered onto the pump-beam). The presented snapshots show the pump-beam profile, but measured through an 150 nm thick metal layer, much thicker than the optical skin depth of the laser (≈ 20 nm at $\lambda = 800$ nm), and at a 500 fs delay (delay in which the phonons would travel only 8 nm, as we have calculated in section 3.3.2.2).

Typically, the phonons should diffuse to this interface only after tens of picoseconds. However, the above experimental results show that we have a strong reflectivity change from the opposite side (regarding the excitation) of the gold film at short time-scales due to the heat absorbed from the pump beam. In other words the pump heating has traveled from the rear side to the front side of the sample within less than 500 fs.

The effects of such an ***ultrafast heat transport*** were also observed by Brorson *et al.* through pump-probe experiments when the sample thickness was varied [79]. The originality of the Brorson's work is that they perform the pumping from one side - the front side of the sample, but monitor *simultaneously* front- and rear- side probes. They compared the temporal evolution of the excitation and relaxation process of the $\Delta R/R$ of the front and back-probe signals between them. As a result, for the "front pump"-"back probe" configurations, the measured delays of the rising $\Delta R/R$ peak (corresponding to internal electron thermalization and hot electron generation) were found to be much shorter (hundreds femtoseconds) than the expected value if the heat were carried by dif-

[5]We need to mention that for the probing wavelength we use (532 nm) the $\Delta R/R$ gold response is negative, i.e., an increased absorption/decreased reflectivity is detected. However, for the ease of visualization, throughout the entire thesis $|\Delta R/R|$ is presented.

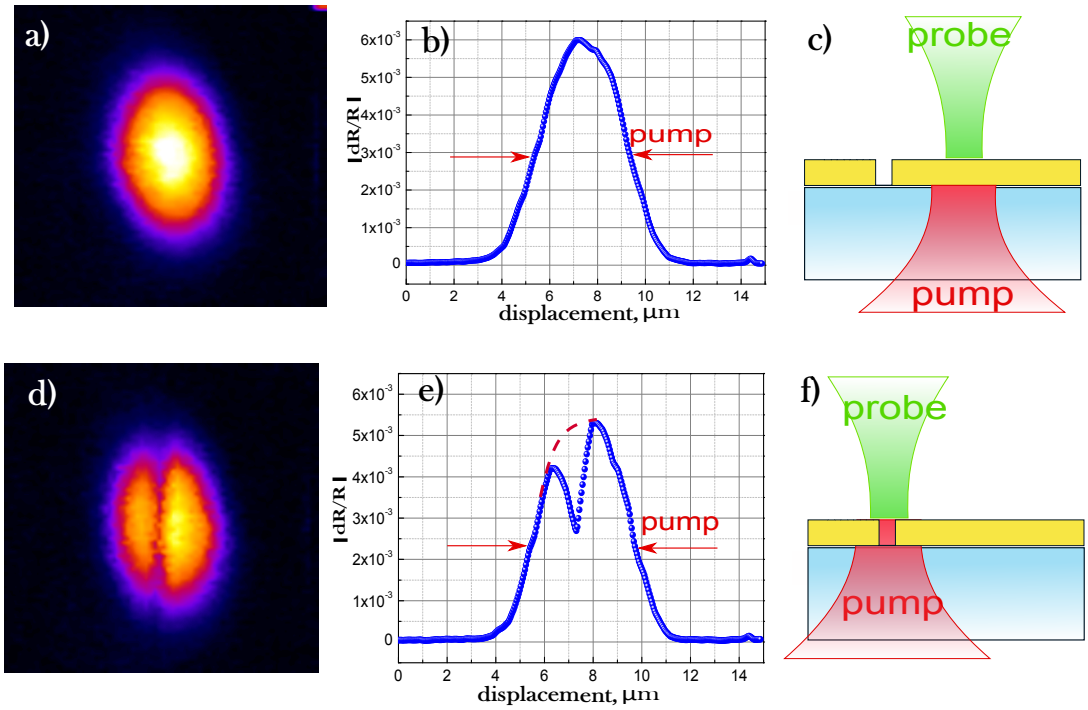

Figure 3.5: *Reflectance maps taken at 500 fs pump-probe delay, in a back-pump front-probe configuration* ***(a)*** *map of gold film, with the corresponding profile in* ***(b)*** *and the sketch of the performed measurement in* ***(c)****;****(d)*** *map of a* 400 nm *slit when the pump pulse is incident on it, the respective profile in* ***(e)*** *and sketch of the measurement in* ***(f)****. In* ***(d,e)*** *we remark a decrease in* $\Delta R/R$ *at the slit-location. In the presented images we reveal the pump-beam profile probed at the opposite side of the metal film. The pump-beam is not well centered onto the slit.*

fusion of electrons in equilibrium with the lattice (tens of picoseconds). Later on, monitoring the delay of the rising peak for different sample thicknesses, they found the delay to increase linearly. Finally, by repeating the experiment for several film thicknesses, they extracted a heat transport velocity of $\approx 10^6$ m/s. This is of the same order of magnitude as the Fermi velocity of electrons in Au, $v_F = 1.4 \times 10^6$ m/s. The authors concluded that the origin of the ultrafast heat transport from front to back is caused by (supposedly) ballistic hot electrons, which are out of equilibrium with the lattice at this time scales.

Photoexcited electrons at Fermi velocity v_F, in gold will move over 100 fs, on a distance $d \approx 100$ nm. Consequently, for a gold film of 150 nm employed in previous experiment, the hot electrons generated by the pump pulse on the rear

film side can reach the front side after a few hundreds of femtoseconds. This effect is the origin of the $\Delta R/R$ measured at short pump-probe delays and presented in Fig. 3.5.

We need to mention that besides the effect of hot electron transport, there is the effect of hot electron diffusion to also consider. This process, although considerably slower than electron transport at v_F, still overlaps with the time-scales we perform our studies. Thus, for a metal film thicker than the laser skin depth ($d > 30\,\text{nm}$) there is an electron flux diffusing in the film depth. This effect can be brought in evidence with a comparative study of reflectivity change amplitude and relaxation behaviour of gold films of two markedly different thicknesses. In Fig. 3.6(a) are presented the results of time-resolved responses obtained by pumping and probing ($\lambda = 800\,\text{nm}$, and 532 nm respectively) two gold films of 50 and 150 nm thicknesses (with the experimental sketch in Fig. 3.6(b)). By comparing the two sets of curves, obtained in similar experimental conditions, the main feature is the strikingly different thermal relaxation of the two samples. The increasing film thickness decreases the observed reflectivity decay time-constants. We explain this by considering that with different film thicknesses, we have a different initial *depth*-distributions of the absorbed energy.

In the 150 nm thick sample, the pump-excited hot electrons diffuse into greater depths, leading to a fast, almost exponential relaxation of electron temperature within about 3 ps. In contrast, in the 50 nm thin film, hot electron diffusion is inhibited and the energy is stored in a much smaller volume (comparable to the laser skin depth), resulting in an almost linear relaxation decay of the electron temperature during the first 6 ps. The linearity in time can be understood by considering the Two Temperature Model (Chapter1, Eq. 1.27b). During the first few picoseconds the lattice remains cold, so that from the two TTM equations we consider only the first one :

$$C_e(T_e)\frac{\partial T_e}{\partial t} = \frac{\partial}{\partial z}(K_e\frac{\partial}{\partial z}T_e) - g(T_e - T_l) + P(\mathbf{r},t). \tag{3.17}$$

Furthermore, for thin films the absorbed energy is almost homogeneously distributed throughout the film. Hence, there is no temperature gradient to drive hot electron diffusion and the term $\frac{\partial}{\partial z}(K_e\frac{\partial}{\partial z}T_e)$ in Eq. 3.17 disappears. Introducing the electron heat capacity $C_e = \gamma T_e$ into the remaining equation and by

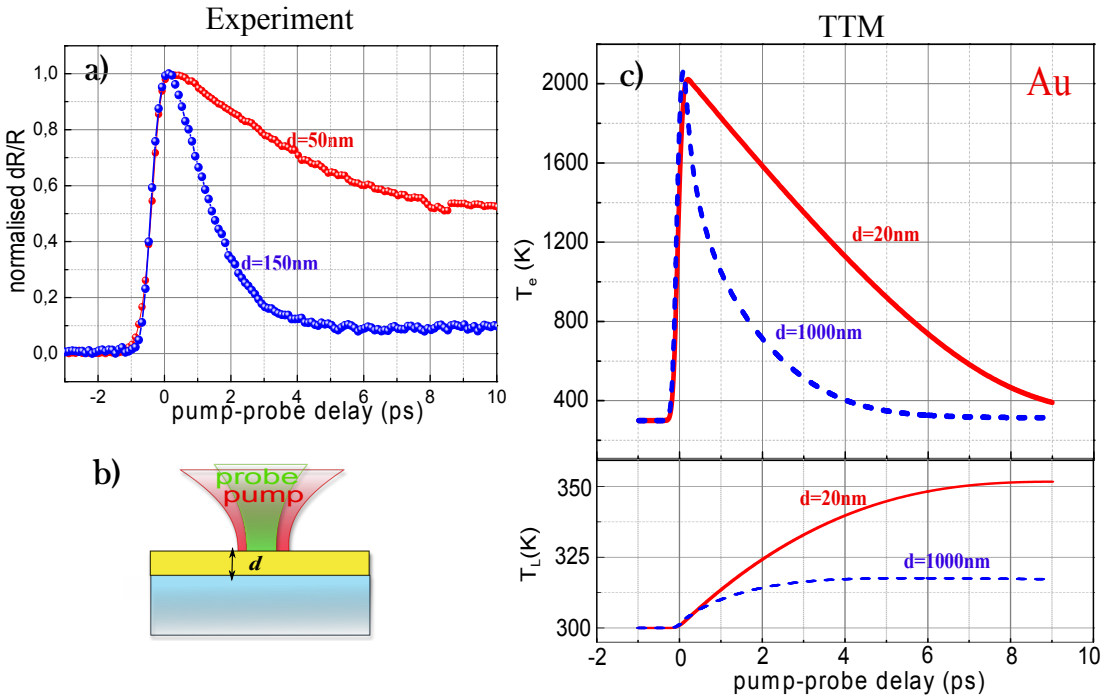

Figure 3.6: ***(a)*** *Comparison of the measured normalized $\Delta R/R$ for gold films of two different thicknesses: a 50 nm and 150 nm thick gold film;* ***(b)*** *the experimental sketch. The measurement has been performed for a pump fluence of 20 mJ/cm^2;* ***(c)*** *Electron temperature relaxation at surface of 20 and 1000 nm thick gold samples (upper curves) and lattice heating (lower curves) as predicted by the TTM. In oder to obtain the same ΔT_e, flunces of 0.49 mJ/cm^2 for the 20nm film and 1.9 mJ/cm^2 for the 1000nm one have been used in the calculations.*

integrating one obtains a linear decay of T_e with time

$$T_e(t) = T_{\mathrm{e,max}} - \frac{g \cdot (1 - T_{\mathrm{amb}}/T_{\mathrm{e,max}})}{\gamma} \cdot t, \tag{3.18}$$

where $T_{e,max}$ is the starting maximum temperature at $t = 0$ and T_{amb} is the initial electron temperature equal to the ambient temperature. Thus, from the above relations, we conclude that the observation of a linearly decreasing change in reflectivity is a signature of the absence of an in-depth hot electron diffusion.

The results presented above are consistent with the TTM calculations for two limiting cases: a 20 nm (comparable with the laser skin depth) gold film and a considerably thicker gold film of 1000 nm. Electron temperature relaxation and lattice heating at surface of bulk and 20 nm thick gold samples are presented

in Fig. 3.6(c). The curves have been calculated with the following material constants: $g = 2{\cdot}10^{16}\,\mathrm{W/m^3K}$, $\gamma = 67.96\,\mathrm{J/m^3K^2}$, $K_{e,0} = 318\,\mathrm{W/mK}$. For obtaining the same ΔT_e, flunces of 0.49 mJ/cm^2 for the 20nm film and 1.9 mJ/cm^2 for the 1000nm one have been used in the calculations. Both T_e and T_l, before the perturbation, have the same initial temperature equal to the ambient 300 K. We see the same tendency as in our previous experiment: the thinner is the sample, the more linear is the electron temperature relaxation behavior. The calculations for the thicker sample, reveal a fast exponential decay due to the hot electrons which diffuse in the sample depth. It is worth mentioning that the effects of electron transport in the performed TTM calculations are not considered.

To summarize, in the case of a gold film thicker than the skin depth ($L >> d_0$), the observed reflectivity decay is very fast since *several competing processes* remove energy from the probed region of the sample: electron transport, electron diffusion, and consequently electron-phonon relaxation. Conversely, when the sample length decreases to the order of the optical skin depth ($L \approx d_0$), less transport and transverse diffusion occurs, and the reflectivity change is primarily due to energy relaxation. The net result is that the front surface reflectivity-decay time increases as the sample dimensions decrease. These findings are in qualitative agreement with previous studies of electron thermalization in gold [71, 115–117].

In the context of surface plasmons absorption, we conclude that the absorption profile around sub-λ apertures depends not only on the spatial shape of the heat source (the absorbed electromagnetic wave), but also depends on the ***complex heat transport*** that takes place inside the metal during the experimental time-frame.

In the actual sample configuration, the *hot electrons excited by the plasmon* are completely blurred by the *hot electrons created by the pump* on the rear side which diffuse to the front surface of the sample. In order to access the signal only due to SPP, we need to develop an approach to block this pump-excited hot electron transport and diffusion.

3.5 Revealing surface plasmon absorption

3.5.1 New sample fabrication and description

In section 3.4.2 we put in evidence the existence of an ultrafast heat transfer (both electron transport and hot electron diffusion), which impedes from observing the absorption of the surface waves around sub-wavelength apertures.

In order to block the electron transport and hot electron diffusion transverse to the film, we have designed a new special multilayered structure [Fig. 3.7(a)]. The whole structure and sub-wavelength slits fabrication process is similar to that described in section 3.4.1, Fig. 3.4(a). The particular changes are brought at the first step, since a multilayer deposition must be employed.

To build the multilayered structure, first the Ti-adhesion and Au layers are sputtered on a fused-silica substrate surface cleaned with Ar-magnetron plasma sputtering. Afterwards, a SiNx layer is deposited with a Plasma-Enhanced-Chemical-Vapor-Deposition technique, onto which the upper gold layer is sputtered. The slit is etched into the multilayer film with electron beam lithography and argon-ion beam etching in an oxygen plasma. Finally, slits with different widths from w = 200 to 800 nm are etched through the multilayered Au(100 nm)/SiNx (25 nm)/Au(100 nm)/Ti(3 nm) film. In Fig. 3.7(b) one sees a microscope image of a 300 nm × 40 μm slit etched in the multilayered structure, while in Fig. 3.7(c) a Scanning Electron microscope image of a 200 nm × 40 μm slit is shown. The SiNx layer buried between two optically-thick gold layers is essential for the thermoreflectance measurements. This insulating layer acts as a barrier thus preventing the tremendous amount of heat deposited by the pump on the rear side. It blocks the hot electron flow coming from the rear interface, at least in the measured time-frame (500 fs) of the pump-probe experiment. This therefore allows us to reveal the weak absorption due to the electromagnetic field scattered by the slit at the front-side interface with thermoreflectance measurements.

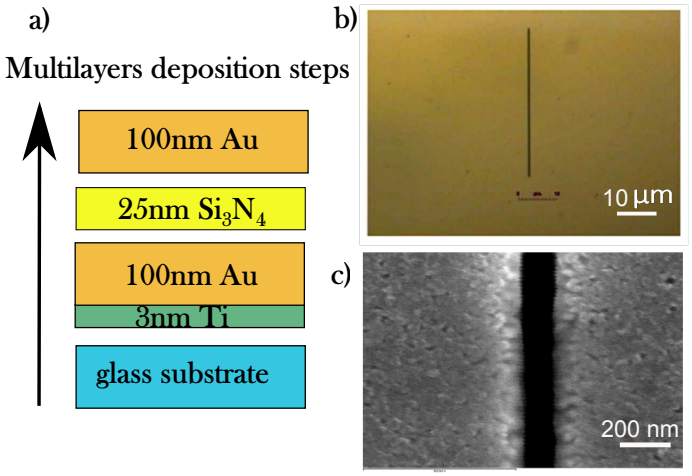

Figure 3.7: *New sample design and fabrication:* ***(a)*** *Multilayer-ed structure of the sample.* ***(b)*** *Optical microscope image of a* $300nm \times 40\mu m$ *slit etched in the multilayered structure;* ***(c)*** *A Scanning Electron Microscope image of a nanoslit.*

3.5.2 Results

3.5.2.1 Blocking the transverse hot electron diffusion

Now let us focus on the role of the aforementioned insulating layer. To make it evident, we have performed three comparative experiments (Fig. 3.8). For all three experiments, we use a back-incident pump (800 nm, $\approx 30\,\mu$m beam waist, $35\,mJ/cm^2$) and a front probe (532 nm, $\approx 2.5\,\mu$m beam waist, $3\,mJ/cm^2$ records the relative reflectivity changes $\Delta R/R$.

Fig. 3.8(a) illustrates the time-resolved signal measured by pumping a 150 nm thick gold film without any insulating layer. The blue curve (in the left pannel of Fig. 3.8) corresponds to this case and clearly shows a heat transport occurring across the film. To suppress this transport, we add the SiNx insulating layer. Fig. 3.8(b) shows the second experiment when we measured the Au(100 nm)/SiNx (25 nm) /Au(100 nm)/Ti(3 nm) film. The corresponding curve (black) demonstrates the efficient suppression of the electron transport. In the third experimt, the pump impinges on a nanoslit in the multilayered structure [Fig. 3.8(c)] and the probe measures the $\Delta R/R$ signal at $\approx 10\,\mu$m away from the slit, i.e., the plasmon-induced heating. The red curve in the left pannel of Fig. 3.8 corresponds to this case. Thus, this layer very efficiently suppresses the heat transport normal to the film.

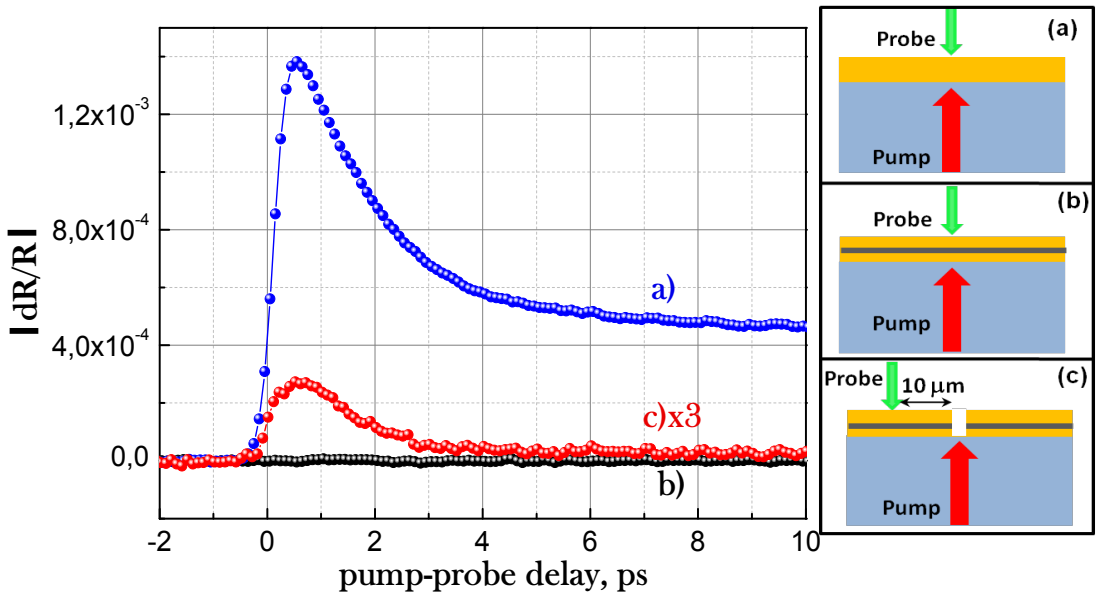

Figure 3.8: *$\Delta R/R$ time-resolved response as a function of the pump-probe delay for (a) 150 nm thick gold film (blue curve), (b) for the Au(100nm)/ SiNx (25nm)/Au(100nm)/Ti(5nm) film (black curve) and (c) the sample from (b), at 10µm from the slit, in the region where we launch SPP and CWs (red curve).*

3.5.2.2 Revealing the SPP absorption profile and the plateau feature

We repeat the same experiment described in section 3.3.1 and depicted in Fig. 3.3, but now we probe the reflectivity changes around sub-λ slits in the presence of the isolating-barrier layer. The reflectance maps for a 300 nm width slit, recorded at 500 fs pump-probe delay, are presented in Fig. 3.9. The snapshot taken for a TE polarization of the pump (i.e., electric field is parallel to the slit) and for a TM pump polarization (i.e., electric field oriented perpendicular to the slit) are shown in Fig. 3.9(a) and Fig. 3.9(b), respectively.

By comparing the two images, the first striking observation is that, away from the slit, the reflectance variation is much weaker for TE polarization than for TM, consistently with the fact that, only for TM polarization, part of the scattered light is launched on the metal surface and is dissipated as heat. The signal around the slit, for a TM-polarized pump, is the signature of the hot electrons due to surface waves absorption. To the best of our knowledge, Fig. 3.9 represents the first *direct non-intrusive observations of absorption loss induced by light scattering at a sub-wavelength aperture in metal films.*

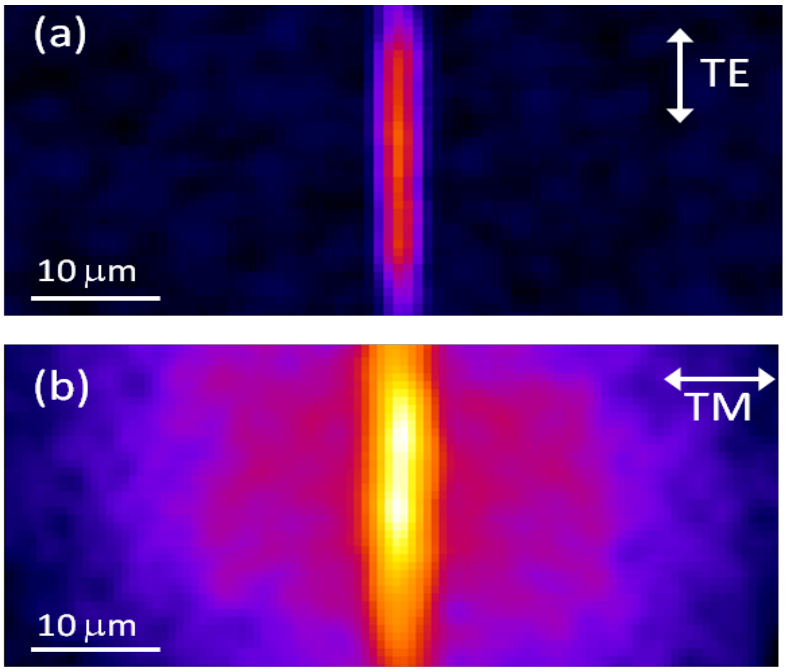

Figure 3.9: *Reflectance maps for a 300 nm width slit.* ***(a)*** *Images obtained for TE polarization, when the energy is not coupled to plasmons, so we do not observe any absorption around the slit.* ***(b)*** *The same slit from* ***(a)*** *but for a TM polarization of the pump beam; The signal around the slit is the signature of the hot electrons due to surface waves absorption.*

In order to obtain a more quantitative analysis, we extract 40 horizontal adjacent line scans from the central part of the TM image [Fig. 3.9(b)] and average them. The averaged thermal profile is shown in Fig. 3.10 (black dots). The absorption is maximal at the slit location. Far from the slit, the absorption gradually decreases. This behavior is expected since it is generally admitted that the amplitude of waves generated by local scatterers decreases as the distance increases. However, at intermediate distances from the slit surprisingly, the absorption exhibites a remarkable feature in the form of a plateau. The latter displays a nearly constant absorption over a large spatial interval ($15\,\mu$m $\approx 18\lambda$). This implies that as it propagates away from the slit, the electromagnetic field launched at the metal interface heats the metal but remains essentially constant. Indeed, consistently with the theoretical calculations, the $\Delta R/R$ profile displays a plateau that is essentially constant over a $10\,\mu$m spatial interval.

The theoretically calculated absorption profile $A(x)$ is superimposed over the

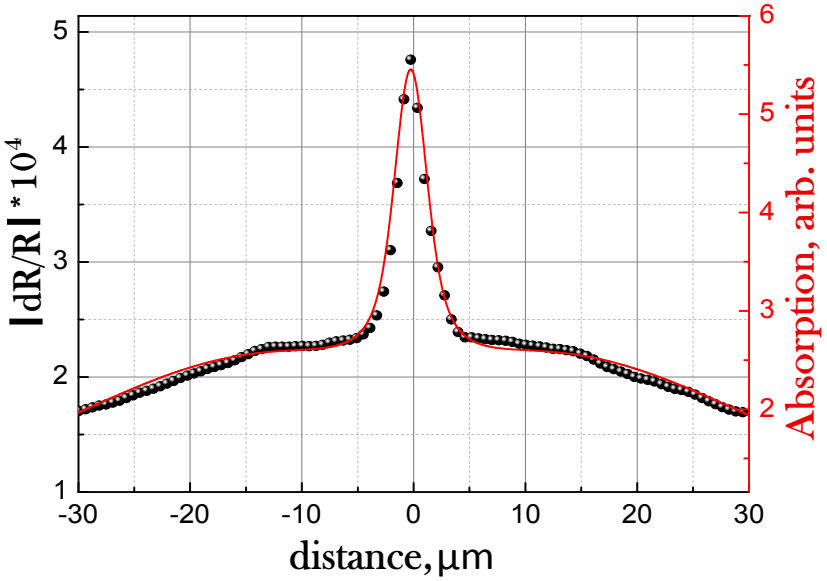

Figure 3.10: *Reflectance map profile around a 300 nm slit superimposed with the theoretically predicted absorption: data (black dots) are obtained by averaging 40 line scans from Fig. 3.9(b). The solid red curve represents the calculated absorption $A(x)$ convoluted by a Gaussian with a FWHM equal to the probe beam waist (2.6µm)*

measured $\Delta R/R$ profile in Fig. 3.10. For this, the theoretically calculated $A(x)$ has been convoluted by a Gaussian with a FWHM of 2.8 μm to mimic the impact of the finite probe-beam waist on the reflectance measurements. The convoluted data are further fitted with the experimental data and are shown by the solid red curve in Fig. 3.10. Comparison of the two curves establishes *quantitative agreement.*

Once we have revealed reflectivity changes caused by plasmon absorption, the point of interest is to compare the amount of the $\Delta R/R$ due to transverse electron transport with the reflectivity changes due to SPP absorption.

We evaluate the measured thermal profiles for the two different structures: the slit in the 150 nm gold film and the slit in the multilayered structure with the SiNx isolating layer. We maintained the same experimental parameters for the two situations (the one used to record the reflectance snapshots in Fig. 3.9) in order to be able to compare the two cases. We recorded a reflectance map of the gold/air interface of the sub-wavelength slits at 500 fs pump-probe delay. The obtained reflectance map has been averaged to a line-profile and superimposed for comparison. The resulting profiles are shown in Fig. 3.11. In Fig. 3.11(a),

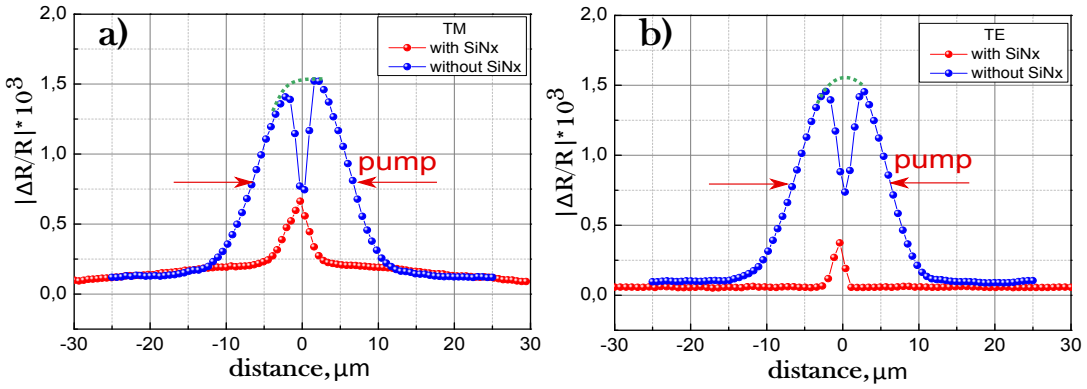

Figure 3.11: *Comparison of the measured $\Delta R/R$ averaged profile around 400nm-width slits in the sample with and without the SiNx isolating barrier:* ***(a)*** *reflectance profiles for a TM-polarized pump around a slit with isolating layer (red circles) and without isolation (blue circles)* ***(b)*** *the same results as in* ***(a)*** *but for a TE-polarized pump. The slit centering is not perfectly the same in different measurements.*

the $\Delta R/R$ profiles of two 400 nm width slits are presented, when a TM polarized pump beam is incident onto its rear side. The blue curve represents the measured $\Delta R/R$ for the slit in a 150 nm gold film, while the red curve is the reflectivity change around the slit in the presence of the electron-barrier layer. We observe that the reflectivity change due to plasmon absorption in the plateau region is one order of magnitude smaller than the $\Delta R/R$ caused by the hot electrons created by the pump on the rear side of the sample. The hot electrons created by a propagating SPP in Fig. 3.11(a) are completely "overwhelmed" by the hot electrons created by the pump, such that the detection of the former is impossible without removing the latter.

Fig. 3.11(b) represents the same experiment, but for a TE polarized incident pump beam. The $\Delta R/R$ signal for the slit milled in the multilayered structure (red curve) is virtually null around the slit. Since we do not launch SPPs for this polarization, there is nothing to be absorbed and to create hot electrons. While for the blue curve, the reflectivity change due to hot electrons excited by the pump, has the same magnitude as for a TM polarization (this sample). From this we can conclude that the transverse electron transport is not sensitive to the incident pump polarization.

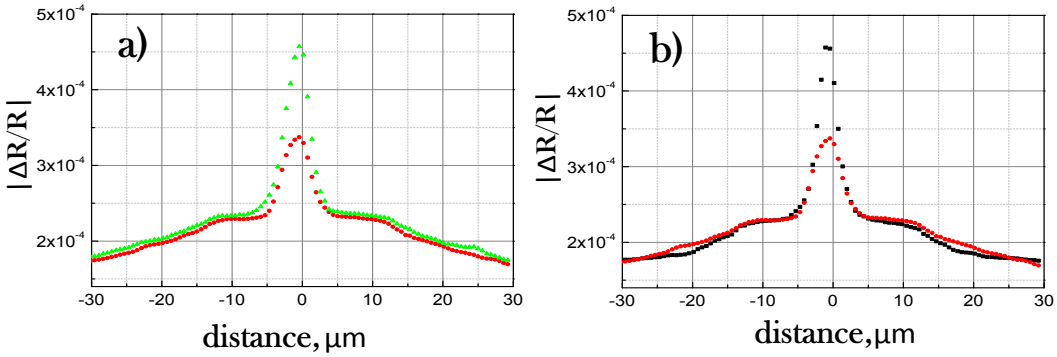

Figure 3.12: *$\Delta R/R$ profiles for different pump and slit size.* ***(a)*** *400 nm (green triangles) and 300 nm (red circles) slit widths;* ***(b)*** *profiles for a 30 μm (red circles) and 40 μm (black squares) pump waists. The size of the plateau is not affected neither by the slit width, nor by the pump beam size.*

3.5.2.3 Plateau length dependence

The reflectance measurements have revealed the existence of a region of constant absorption. The numerical simulations have predicted the large plateau-region of tens of wavelengths in agreement with an analytical model that explains the origin of this plateau using the interference between two surface waves, namely SPPs and quasi-cylindrical waves. We have a beating between the two waves. Also from the analytical model we deduced the length L of this plateau to be approximately given by half of the beating period:

$$L \approx \lambda \cdot \mathrm{Re}\left(\frac{\epsilon_m}{\epsilon_d^{3/2}}\right), \tag{3.19}$$

where ϵ_m and ϵ_d represent the permittivity of the metal and the dielectric, respectively. From the above expression, one can see that for a given excitation wavelength, the plateau length is independent of any experimental parameters and is not even dependent on the dimensions of the scatterer (the slit width in this case). The only physical quantity which impacts the plateau length is the nature of the employed materials, i.e., permittivity of the metal and the dielectric. In order to verify the validity of the above expression, we have performed measurements by varying some of the available experimental and geometrical parameters. In particular, we have investigated how the plateau length is af-

fected by the pump beam diameter and the slit-structure width. The results are summarized in Fig. 3.12. The investigation of the influence of the slit width is presented in Fig. 3.12(a); both profiles are obtained using a 30 μm pump waist, but for 300 nm (red circles) and 400 nm (green triangles) slit widths. The influence of the pump beam diameter is shown in Fig. 3.12(b) where the $\Delta R/R$ profile is obtained by focusing a 30 μm pump waist (red circles) and 40 μm pump waist (black squares) onto a 400 nm slit width. From these findings we conclude that the size of the plateau is not affected by the size of the pump beam. This is a direct consequence of the effective isolation provided by the insulating layer. As the size of the beam waist is far from the diffraction limit, and we have a geometry in which the excitation is invariant along the slit, we can assume a plane wave excitation. Thus, our experimental condition is similar to the developed theoretical model and the size of the plateau does not depend on any geometrical parameters. Consistently, Fig. 3.12 shows that the plateau characteristics do not depend on the slit width and the pump size, within the interval of available parameters we work with.

3.5.2.4 Plateau signal dependence vs pump power

An important characteristic of the plasmon-induced reflectivity or temperature change, is its dependency on incident pump power. For this we have performed a study of the reflectivity change signal for different incident powers. For a slightly focused pump beam ($\approx$ 30 μm beam waist) the average pump power has been varied from 30 to 65 mW (17 – 37 mJ/cm^2). The probe beam ($\approx$ 2.5 μm beam waist, 3 mJ/cm^2) is focused at 10 μm distance away from the slit, in the plateau region. We detect the $\Delta R/R$ signal at the characteristic 500 fs pump-probe delay.

The obtained values (black dots) are shown in Fig. 3.13, and the red dashed line represents the best linear fit curve. From the measured data one can conclude that, in the weak excitation regime we work with, the reflectivity change (and consequently temperature changes), induced by plasmon absorption, depends linearly on the incident pump power.

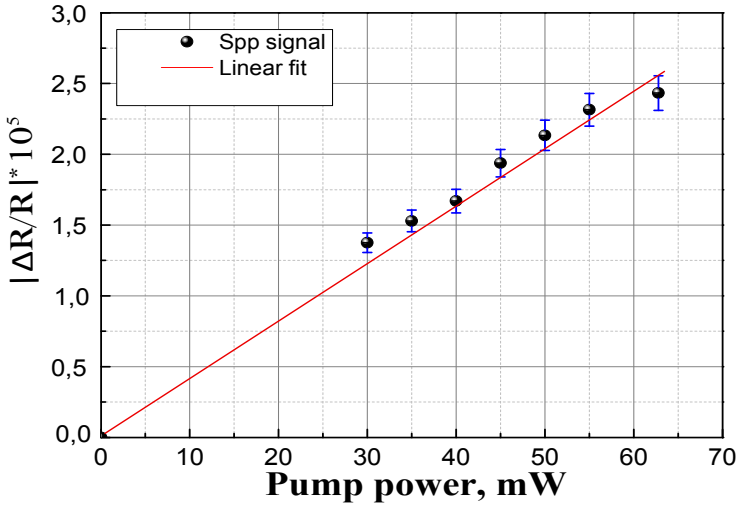

Figure 3.13: *Relative change of reflectivity, caused by the plasmon-excited hot electrons, as a function of pumping power. The signal is measured at 10 μm distance from the slit (in the absorption plateau region). The dashed red line represents a linear fit to the experimental points.*

3.5.2.5 Plateau signal dependence on slit width

The final quantitative characterization of the sub-wavelength slit experiment is the investigation of the amount of the temperature change around the aperture and its dependence on the slit width. The amplitude of the temperature variation around the slit depends directly on the quantity of generated plasmons (and quasi-cylindrical waves). A slit which more efficiently couples the incident far-field radiation to plasmons, will be characterized by a higher absorption around it, i.e., higher ΔT_e. The ability of a structure to couple the incident radiation into SPPs is characterized by the SPP generation efficiency factor.

We have mentioned previously that the slit structure is a canonical and fundamental type of scatterer in diffraction optics. Therefore, it received considerable attention, both theoretically and experimentally [49, 118–120]. In the relevant work of Kihm *et al.* [121], generated SPP's intensities are directly measured through a near-field scanning microscope measuring both the transmitted and the scattered light as a function of the slit width. These results demonstrate enhancement as well as suppression of surface plasmon generation efficiency at specific slit widths. The experimentally observed sinusoidal width dependence is explained by diffraction theory. A single slit with an optimal slit width shows

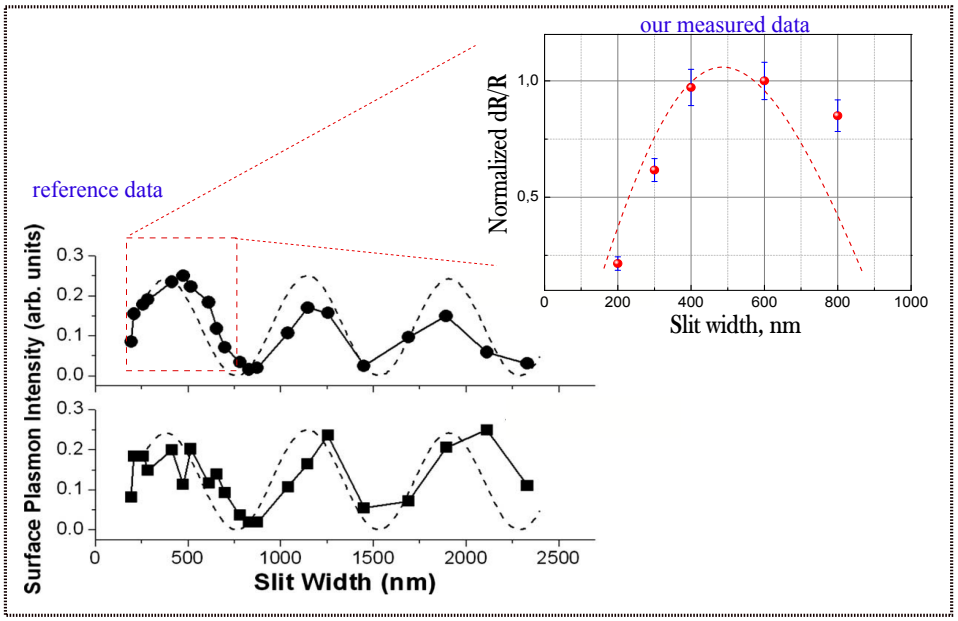

Figure 3.14: *Near-field analysis as a function of the slit width by measuring the transmitted light (filled circles), scattered light (filled squares) and calculated slit-width dependent SPP launching (dashed line), based on the diffractive nature of plasmons. The incident wavelength was λ = 780nm. By the red dashed-square is delimited the range of slit-widths available in our experiments and should be compared with our results (from [121]). The* **inset** *shows* ***our measured data****: the normalized relative change of reflectivity, caused by the plasmon-excited hot electrons, as a function of the slit width (red circles), the red line is a guide for the eyes. The incident pump fluence is kept the same for for all measurements.*

a ten times stronger SPP generation compared to the slit with the minimum generation efficiency. Our point of interest was to verify if the absorbed surface plasmon energy, brought in evidence by reflectivity change, will have a dependency on the slit width parameter.

As we mentioned in section 3.5.1, we have fabricated slits of different widths: 200, 300, 400, 600 and 800 nm. We performed a point-measurement with a slightly focused pump ($\approx 30\,\mu$m) incident onto the slit and the probe ($\approx 2.5\,\mu$m) focused in the absorption plateau region. The incident pump fluence is kept constant for all measurements around 25 mJ/cm^2 and the variable parameter was the slit width. Our measurement results, together with those from Ref. [121], are presented in Fig. 3.14. The reference data has been obtained for 780 nm excitation wavelength, and the minima in the signal are observed at approximately the integer multiples of the incident wavelength. With the red-dashed square, we

have delimited the region of slit-widths measured in our experiment.

The *inset* of Fig. 3.14 summarizes our measurements of normalized relative change of reflectivity, caused by the plasmon-excited hot electrons, as a function of the slit width .

The reflectivity changes around the sub-λ structure increase with the increasing width, in the slit-width range $100-600\,\text{nm}$ and reaches a maximum at about $400-600\,\text{nm}$. Afterward the signal begins to decrease for a slit-width of 800 nm. According to [121], a minimum should be found at a width around 800 nm (for an incident pump $\lambda = 800\,\text{nm}$, but in our experiment the measured reflectivity change for this slit width is still higher than the one measured for the 200 nm width.

3.6 Conclusion

In summary, we applied pump-probe thermoreflectance to measure the surface plasmon absorption around sub-λ structures in metal films. As we have shown in this chapter, the measurement of the plasmon absorption is more complex than one may assume, since we need to measure the local heat source before the diffusion process starts. We also put in evidence the existence of an ultrafast heat transport across the sample at femtosecond time-scales, which was eliminated by employing a multilayered structure with an electron barrier layer.

Finally, we imaged the absorbed SPP energy around a nanoslit, by measuring the generated hot electron bath, and revealed that the absorbed energy does *not* decrease continuously with increasing distance from the scatterer, but remains constant over a large range of several tens of wavelengths. Thus, in this plateau area, the dissipated heat is weaker than the heat deposited by the plasmon launched at the surface. This phenomenon that occurs only with noble metals at near-infrared wavelengths ($\lambda > 800\,\text{nm}$) is an intrinsic property, which is likely to be observed for any sub-wavelength aperture geometries. This opens interesting perspectives for optimizing the performance of metallic devices for energy harvesting, or for designing compact plasmon launchers that deliver surface plasmons at a certain distance with a reduced heat dissipation at the delivery point, a valuable property for lowering decoherence in quantum plasmon circuitry [122].

Our results provide the first comprehensive study of the photothermal heat generation in plasmonic films with sub-wavelength patterns, and may allow us to derive new recipes for managing optical heating in complex plasmonic systems on different time and space scales by combining surface plasmons with localized plasmonic resonances [1, 123].

CHAPTER 4

Surface plasmons and hot electrons dynamics

In the previous chapter the only advantage of femtosecond resolution laid in preventing hot electron transport from rear to front side of the sample. In this chapter we keep on investigating the time-resolved response of surface plasmon absorption losses in a free space metal film propagation. In this case we use a metallic grating structure as a efficient SPP transducer. By imaging the reflectivity relative changes induced by plasmon-excited hot electrons, we can visualize the absorption of SPP wavepackets at different positions in time as it propagates along the metal-air interface. We performed a qualitative characterization of absorption-mediated SPP signal and we estimated the propagation length of plasmons and their group velocity.

Contents

4.1 Introduction

In the previous chapter we have illustrated that the plasmon surface waves, while propagating at a metal/dielectric interface, are absorbed and heat up the metal. This plasmon heating is large enough to induce a variation in the refractive index and thus, a change in the ability of the metal to reflect light. By detecting $\Delta R/R$ due to electronic temperature variation, at time scales when electrons are out of the equilibrium with the lattice ions, we measure the absorbed plasmon energy.

Next, we study the temporal evolution of the plasmon-mediated hot electrons. For this, we have chosen to work with another type of SPP launching structure, specifically, metallic gratings. This selection has been done for several reasons:

1. The slit structure is inconvenient for generating SPPs as for a normal incident light (configuration available in our experiment) the plasmon generation efficiency is small, being 1-3%. Consequently, the absorption signal is relatively weak, which makes it difficult to perform a study of the dynamics. In contrast, an array of such sub-λ slits assure that $25 - 30\%$ of the incident radiation is coupled into SPPs.

2. The grating coupling scheme allows one to define a much better confined SPP source.

3. Numerical simulation on the absorption around a grating structure has shown that there is no wave interference effects and the absorption is due to launched SPPs. In this way, by measuring the plasmons absorption losses through hot electrons, we will try to indirectly characterize the launched plasmons.

Thus, gratings with sub-λ period have been fabricated and used to efficiently couple the incident light to SPPs. The excited SPPs travel at the local speed of light and cross a distance of *tens* of μm in *hundreds* of fs, which is compatible with the temporal range of our laser pulses. Subsequently, by measuring the temporal evolution of plasmon-excited hot electrons, we have estimated indirectly the propagation length and group velocity of excited SPPs.

4.2 Theory of grating

Metallic gratings have a special importance in plasmonics, as they are standing at the origin of this field. After its discovery in 1902 by Wood [124], grating "anomalies" have fascinated specialists of optics for over a century. Wood, observing the spectrum of a continuous light source given by an optical metallic diffraction grating, noticed an "anomalous" phenomenon: under certain conditions, a drop from maximum illumination to minimum takes place, and it happens, remarkably, for only TM-polarized light, i.e., electric field is perpendicular to the grating grooves. Even though the notion of Surface Plasmon Polariton (SPP) appeared more than half a century afterward, Wood's discovery is undoubtedly a cornerstone of plasmonics. Later on, Lord Rayleigh conjectured that the anomaly occurs at grazing incidence, implying that the absorption anomaly has a purely geometrical origin [125]. After 30 years, Strong [126] showed that the spectral location of Wood's anomalies of different metallic gratings having the same period was dependent on the metal. Finally, these anomalies were associated to the excitation of surface waves, by Fano [127].

SPP generated by gratings has been extensively studied. The pioneering work of Ebbesen *et al.* of extraordinary optical transmission through sub-wavelength hole arrays [92] can be explained by the excitation of SPPs on the periodic arrays. Radko *et al.* systematically studied the efficiency of local SPP excitation on 1D periodic ridges [128]. The grating coupling scheme is also an efficient technique, which is now widely adopted as an SPP source in NSOM experiments [129].

Once the plasmon launched, its propagation direction can be controlled via scattering at locally created defects, in the otherwise planar film. The scatterers can be introduced in the form of surface undulations, or by milling of holes into the film. Their controlled positioning enables the realization of functional elements such as Bragg mirrors for reflecting SPPs [38]. Even plasmon focusing can be achieved, which was shown by Offerhaus and colleagues using noncollinear phase-matching [130].A simple example of control over SPP propagation via scattering from height modulations was demonstrated by Ditlbacher and coworkers [38].

Regarding our experiment, for a further possibility to manipulate and to study more complex SPP processes and the related hot electron behavior, we require

a clear spatial separation between the SPP launcher and the propagating SPPs themselves. From this point of view, compared to other coupling mechanisms (like Kretschmann, Otto configurations, Fig. 1.4), the grating coupling scheme allows one to define a rather better-confined region of the SPP source (however, it is still not well focused enough for many nanoplasmonic applications). Comparing to the slit structure, which acts as a single diffraction sub-λ object, it does not require specific resonant conditions and one can excite plasmons over a wide spectrum of incident wavelengths, by using a grating SPP launcher, we need to fulfill a coupling condition.

For this reason, we must explain how light couples into SPPs in a grating structure and on what parameters an efficient SPP generation depends on. It is also important to adjust proper grating parameters to fit the experimentally available range of wavelengths.

Surface plasmon polaritons on a flat metal/dielectric interface cannot be excited directly by light beams unless special techniques for phase-matching are employed. We have already pointed out that the SPP dispersion curve [Fig. 4.1(a)] lies outside of the light cone of the dielectric. At a given photon energy $\hbar\omega$ and wavevector $\hbar\omega/c$, the projection along the interface of the photons momentum $k_{x,\mathrm{ph}} = k_{\mathrm{ph}} \sin\theta$ impinging under an angle θ, is always smaller than the SPP propagation constant k_{SPP}, even at grazing incidence, thus impeding phase-matching. In order to convert the far-field electromagnetic waves into SPPs, $k_{x,\mathrm{ph}}$ needs to be increased by a Δk_x value. Patterning the metal surface with a grating of grooves or holes with lattice constant a represents one way to overcome the mismatch in wavevector between the in-plane momentum $k_{x,\mathrm{ph}}$ of impinging photons and k_{SPP}.

For the simple one-dimensional grating of grooves depicted in Fig. 4.1(b), if an incident beam impinging onto a grating under an angle θ, its component in the surface can have wavevectors $\frac{\omega}{c}\sin\theta \pm m\frac{2\pi}{a}$, where m is an integer.

The dispersion relation can then be fulfilled by the sum of the constituting wavevectors in the surface:

$$k_x = \frac{\omega}{c}\sin\theta \pm m\frac{2\pi}{a} = \frac{\omega}{c}\sqrt{\frac{\epsilon}{\epsilon+1}} = k_{\mathrm{SPP}}, \tag{4.1}$$

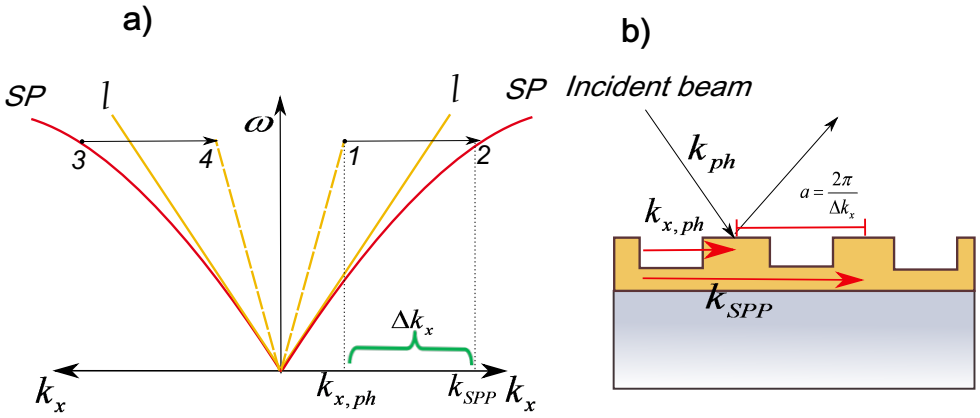

Figure 4.1: *The grating coupling.* ***(a)*** *SP: dispersion relation of SPPs, l: light line. The incoming light, having wavevector* $k_{x,\mathrm{ph}}$*, point (1) is transformed into SPP, denoted by point (2), by taking up* Δk_{x}*. The process* $3 \rightarrow 4$ *describes the decay of a SPP into light via* Δk_{x}*; it is the reverse of* $1 \rightarrow 2$*.* ***(b)*** *An incident beam impinging onto a grating under an angle* θ *has the wavevector component in the surface* $k_{\mathrm{x,ph}}$ *always smaller than* k_{SPP}*. It can be increased by* Δk_{x} *patterning the metal surface with grating of the period* $a = 2\pi/\Delta k_{\mathrm{x}}$ *and SPP phase-matching is achieved.*

or more generally

$$k_x = \frac{\omega}{c} \sin\theta \pm \Delta k_x = k_{\mathrm{SPP}}, \tag{4.2}$$

where Δk_x, the vector $1 \rightarrow 2$ in Fig. 4.1(a), originates from any perturbation in the smooth surface (a grating groove in our case); $\Delta k_x = 0$ gives no solution of the dispersion relation. Once phase-matching is fulfilled the resonance can be observed as a minima of the reflected light.

The reverse process can also take place: SPPs propagating along a surface modulated with a grating can reduce their wavevector k_{SPP} by Δk_x so that the SPP is transformed into light, and thus radiate into far-field (see Fig. 4.1(a) arrow $3 \rightarrow 4$). This light emission, a consequence of the photon-SPP coupling via roughness, plays an important role as it can be used as a detector for SPPs [131]. For example, Park and co-workers have demonstrated outcoupling of SPPs using a dielectric grating of a depth of only several nanometers with an efficiency of about 50% [132].

In our experiment, we work under focusing conditions and assume a normal incident pump on the grating. We would now like to establish the relation between the values of a, the grating period, and incident wavelength at which

phase-matching is achieved. From Eq. (4.1), it is straightforward to show that a normal incident plane wave approaches, the SPP excitation condition at a particular grating period defined by

$$a = \frac{2\pi}{k_{\mathrm{SPP}}}. \tag{4.3}$$

Therefore, the SPP resonant condition can simply be matched by designing the grating period to meet the momentum requirements with different metal/ dielectric configurations. Keeping in mind that $k_{\mathrm{SPP}} = 2\pi/\lambda_{\mathrm{SPP}}$, Eq. (4.3) gives:

$$a = \lambda_{\mathrm{SPP}}. \tag{4.4}$$

In other words, at normal incidence the grating period should be equal to the wavelength of the plasmon to be excited. In our experiments, usual pump wavelength is $\lambda_0 = 800\,\mathrm{nm}$ and in this case at a gold/air interface the wavelength of the excited SPP is:

$$\lambda_{\mathrm{SPP}} = \lambda_0 \sqrt{\frac{\epsilon_d \epsilon'_m}{\epsilon_d + \epsilon'_m}} \approx 780\,\mathrm{nm}, \tag{4.5}$$

where $\epsilon_d = 1$ is the permittivity of air and ϵ'_m is the real part of the permittivity of gold ($\epsilon_m = -22.1 + 1.77i$ at 800 nm taken from [107]).

From the above calculations, we conclude that for a normal incident light with $\lambda_0 = 800\,\mathrm{nm}$ the grating period (a) should be equal to 780 nm for an efficient SPP excitation.

4.3 Experiment and sample description

4.3.1 Experimental description

The experiment we performed is schematically depicted in Fig. 4.2. A pump pulse (800 nm, beam waist 4 μm, 10 mJ/cm^2) is incident onto the grating structure from the air side. The incident light is dominantly reflected or absorbed. And a fraction of this incident energy is launched along the metal/air interface as surface plasmons. The SPPs propagate along the interface and get absorbed. The absorbed energy heats the metal film. And as the plasmon pulse lasts $\approx 100\,\mathrm{fs}$, all the deposited heat is firstly taken by the free electron gas. We detect

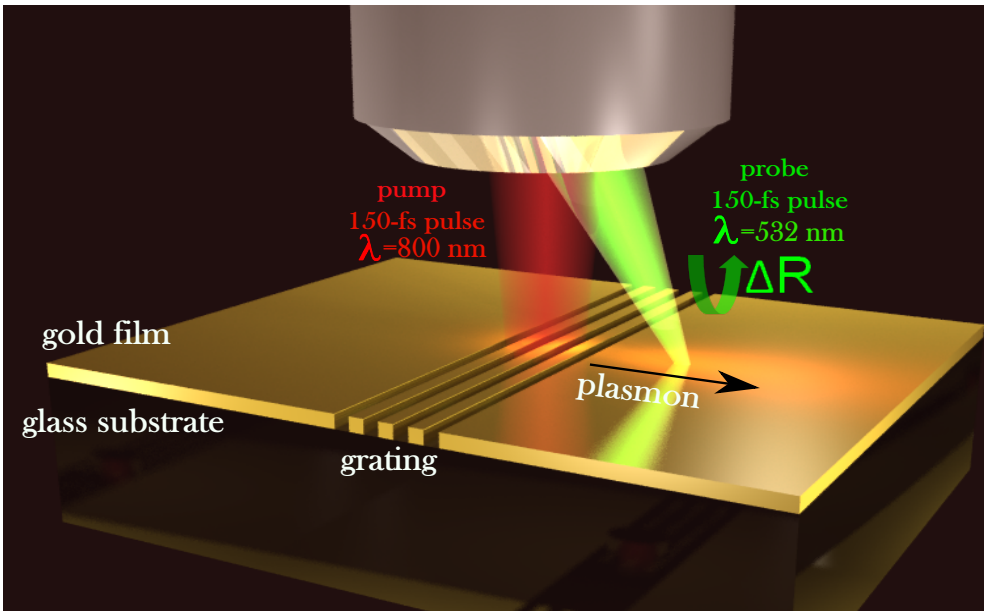

Figure 4.2: *Sketch of the grating-experiment: A first laser pump pulse (λ = 800 nm, 150 fs FWHM) is incident on the array of sub-λ slits on the gold/air interface. A second laser pulse (λ = 532 nm) probes the air-gold interface and records the reflectance variations ΔR with a controlled delay between the pump and the probe pulses. The pump and probe beams are incident on the same interface and pass through the same microscope objective.*

hot electrons at 500 fs delay with the probe pulse (532 nm, beam waist 2 μm, 3 mJ/cm^2), which raster scans the surface of the metal and detects the changes in reflectivity induced by temperature variations and heating.

Comparing the current experiment with the one from Chapter 3, we should emphasize several major differences:

1. For a better SPP coupling and respectively, higher generation efficiency and higher absorption, we have chosen to pump from the air side onto the grating. At the same time the probe is detecting the reflectivity change at the same gold/air interface. This implies that the pump and probe are incident on the same interface and are passing through *the same microscope objective*, which makes it difficult to adjust convenient pump and probe beam waists.

2. In this current experiment, the pump waist is rather highly focused. The generated SPP propagates a distance of tens of μm away from the location

it was generated. In this way the pump and the plasmon are spatially separated.

The second point above is rather important because it diminishes the problem of the pump-excited hot electron transport and diffusion. The hot electrons excited by the pump and which propagate at Fermi velocity (1.4×10^6 m/s), in 100 fs will transport the energy over a distance of $L = V_F/\Delta t \approx 100$ nm. At the characteristic pump-probe delay of 500 fs, the distance travelled by electrons at v_F in both transverse and lateral directions are ≈ 500 nm. As we are not interested in the $\Delta R/R$ on the rear sample side (gold/glass interface), the transverse hot electron diffusion is not affecting (at least qualitatively) our measurements performed on the front side. The lateral diffusion of 500 nm compared with tens of μm characteristic SPP spatial extents is negligible.

4.3.2 Sample design and fabrication

The sample has been fabricated using the similar process employed for the slits fabrication (see Chapter 3). We do not employ any multilayered structure. The sample consists of Au(200 nm)/Ti(3 nm) layers deposited on a glass substrate consequently passing trough the steps described in Chapter 3 for grooves etching. Sets of sub-wavelength slit arrays in a semi-infinite gold film have been fabricated by Buntha Ea-Kim at Laboratoire Charles Fabry, CNRS-IOGS-Université Paris XI in Palaiseau, France.

Figure 4.3 shows the structure design and characteristic dimensions. Figure 4.3(a) presents a microscope image of the grating structure constituted of 10 grooves. In Fig. 4.3(b) one can see an AFM image of the structure, with the image profile in Fig. 4.3(c). The AFM measurement profile confirmed that the film thickness is 200 nm and provided us the exact value of the grating period being $a = 780$ nm. The slit-arrays have been fabricated by varying the slit width, but keeping the overall grating period constant. We have shown in the previous chapter that the plasmon generation efficiency depends on the slit width. Thus, there is a grating-to-grating difference in efficiency of plasmon generation.

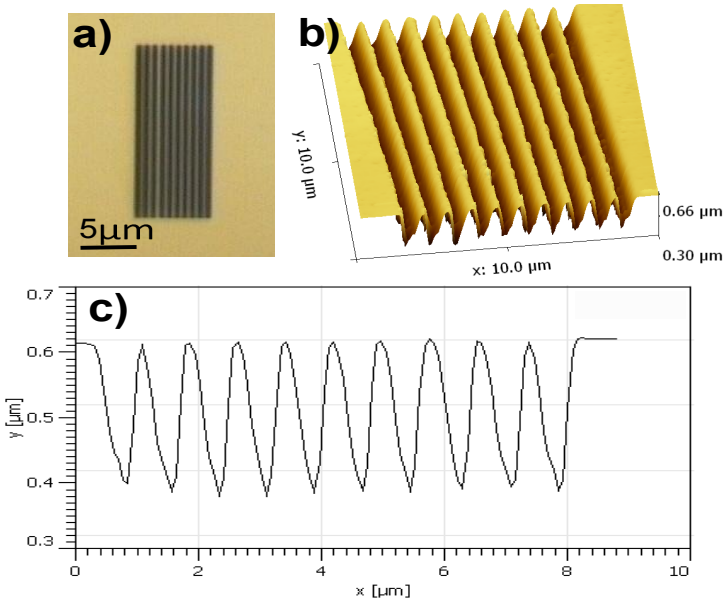

Figure 4.3: *Sample description:* ***(a)*** *Microscope image of a* 500 nm × 200 μm *slit, fabricated with the process described above;* ***(b)*** *AFM image of the sub-wavelength slits array, with the corresponding profile in* ***(c)****; The profile reveals a grating period of* 780 nm *and a gold film thickness of* 200 nm.

4.4 SPPs characterization through hot electrons temperature variations

4.4.1 Qualitative characterisation of plasmon absorption profile launched with a grating

We perform the experiment described previously in section 4.3.1. With the visualization system we locate a grating structure on the sample. Then we focus the pump beam on it. The probe beam raster scans the sample and records the reflectivity change ΔR at 500 fs pump-probe delay. We perform this measurement for two polarizations of the incident pump: TM and TE. As we have emphasized in Chapter 1, the SPP mode can be excited only for the TM incident polarized light. The measurement for the two polarization represents a starting test in all experiments. The crucial sensitivity on the incident light polarization is one of the major proofs for the plasmon origin of the signal we detect.

In Fig. 4.4 the reflectivity change snapshots of the grating structure at 500 fs

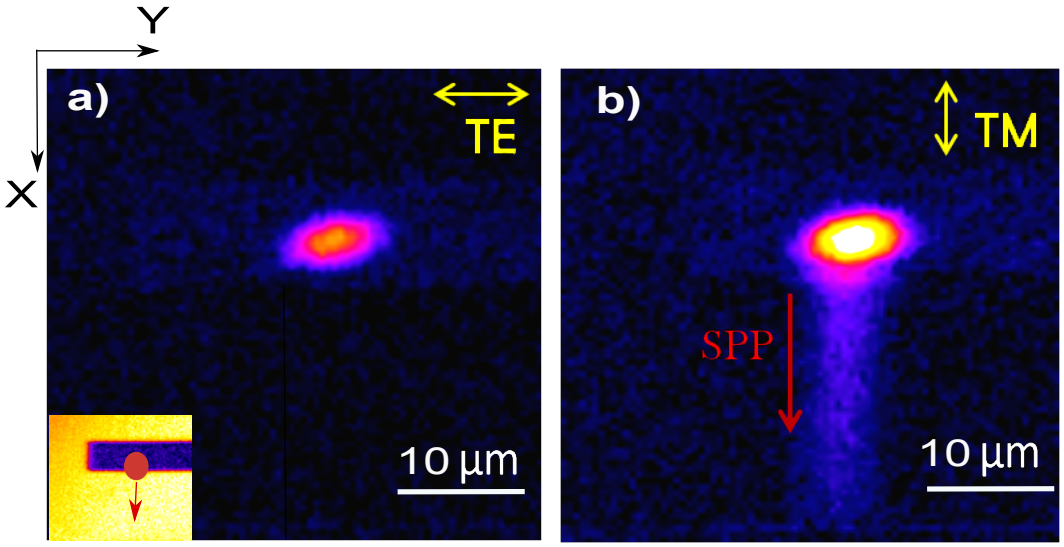

Figure 4.4: *Reflectance snapshots of the grating structure after a pump pulse excitation.* ***(a)*** *Image obtained for TE polarization, when the energy is not coupled to plasmons, so we do not observe any plasmon-absorption signature around the structure.* ***(b)*** *The same structure from* ***(a)*** *but for a TM polarization of the pump beam; The thermal tail starting from the grating is the signature of the excited hot electrons due to surface waves absorption. The inset in* ***(a)*** *represents a reflectivity image of the region being imaged, in the absence of the pump-induced excitation, and we can easily recognize the grating structure as the region with a lower reflectivity. In this way the grating position is also located in the other images.*

pump-probe delay are presented. Fig. 4.4(a) shows the snapshot when the incident light is TE polarized. The thermal signature in the image represents the thermal profile of the pump beam. In contrast, when we change the incident light polarization to TM [Fig. 4.4(b)], we recognize the same thermal profile of the excitation beam, but it gives rise to a thermal "tail" in the X-direction. The thermal tail represents the plasmon-induced metal heating and excitation of hot electrons. The width and spatial energy distribution along the Y-direction of this plasmon thermal tail is determined by the pump beam profile. By comparing the two images we also observe that, apart from the presence of the plasmon signature, the reflectivity change is also higher for TM polarization in the region where the pump beam is incident on the grating. This can be explained by the fact that when incident light is resonant with the grating, a stronger and more complex absorption processes takes place inside the structure for the TM-light (i.e., when the SPPs are generated), than for the TE polarization. The inset of

Fig. 4.4(a) represents a reflectivity image of the region being monitored, in the absence of the pump-induced excitation. In the image, we can easily recognize the grating structure (the region with a lower reflectivity) and in this way, the grating position is also located in the other images.

One can raise the question as to why we generate SPPs only in one direction of the grating, and not symmetrically (as in the case of the sub-wavelength slit structure). This is a direct consequence of the pump beam diameter dimensions compared to the dimensions of the grating structure. As we have mentioned before, an independent adjustment of the two beam waists is limited by the fact that the pump and probe beams are incident from the same microscope objective. The optimum dimensions we achieve for a 50X (NA=0.45) objective represents a $\approx 2\,\mu$m waist for the probe and $4\,\mu$m for the pump waist. In this way the pump beam does not entirely cover the grating structure (which is $\approx 8\mu m$). We have verified experimentally that when we focus the pump close to the upper or close to the lower grating border, we can generate plasmons either propagating up or down, respectively. In contrast, when the pump beam is focused at the center of the structure, we have a symmetrical but extremely weak thermal signatures on the both grating sides. This can be rationalized by the fact that when the plasmons are launched in the middle of the structure, during their propagation through the grating, the reverse process of SPP coupling takes place. This is known as the SPP outcoupling, i.e., SPPs reradiate in far-field. Thus a smaller fraction of SPPs reach the grating border and launch along the metal.

Finally, we consider Fig. 4.5 which describes the SPP behavior in the X-direction, i.e., normal to the propagation direction. It shows sections of SPP field intensity in the Y-direction, revealed by the relative reflectivity change. The four curves represents four cross sections derived from the image of Fig. 4.4(b) along the propagation path. The first section (black squares) is taken across the center of the launching beam. The line profiles are all normalized to the maximum value. Fig. 4.5 illustrates that, even after propagating a distance of $18\,\mu$m and after 500 fs delay, the SPP remains extremely well confined in the original launch direction. It may be concluded that there is no significant elastic SPP-SPP scattering that is strongly directional; significant forward scattering, for example, would lead to a broadening of the successive profiles in Fig. 4.5. These results prove once again that, at this time scale, phonon diffusion is not

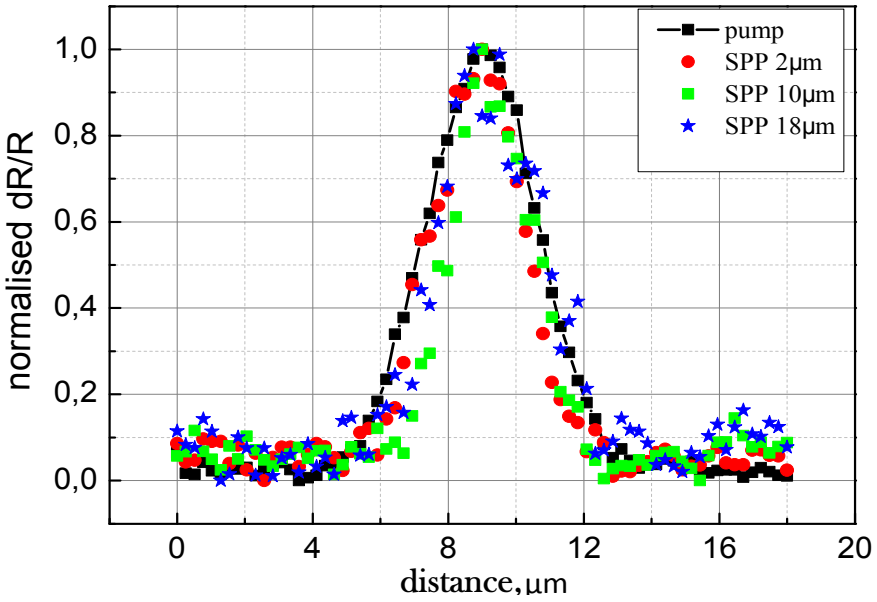

Figure 4.5: *Cross sections of reflectance snapshots from Fig. 4.4(b) of SPP propagating on gold, taken normal to the direction of propagation at various distances along the SPP path: black squares: center of the launching beam; red circles:* 2 μm*; green squares-*10 μm*; blue stars:* 18 μm

yet apparent, while electron diffusion is not spatially substantial. The important conclusion here is that ***the absorption profile is as confined as is the heat source***.

4.4.2 SPP propagation length

We have already mentioned that nanostructured metal/dielectric interfaces offer a whole range of possibilities both for manipulating SPP modes on the surface (beam splitters, mirrors etc. [38]) and for coupling them to freely propagating light [133, 134]. In order to make such wavelength-scale structure effective in manipulating SPPs, it is important that the SPPs have a propagation (attenuation) length that is at least several times their wavelength. The SPP propagation length L_{SPP}, defined in Chapter 1 as $L_{\mathrm{SPP}} = 1/2k_x''$, is a critical parameter for making photonic circuits.

In the following, we proceed with the estimation of propagation length of plasmon from its decaying thermal profile revealed in the reflectance snaphots, and consequently to compare the obtained results with the calculated values

based on material optical constants.

As noted above, the SPP propagation length, L_{SPP} is obtained from the imaginary part of the SPP wavevector and it accounts for internal damping processes due to the finite electrical conductivity of the metal [4]. The exact expression of the complex wavevector parallel to the surface is obtained from Eq. (1.10) as:

$$k_x'' = k_0 \frac{\epsilon_m''}{2(\epsilon_m'^2)} \left(\frac{\epsilon_m' \epsilon_d}{\epsilon_m' + \epsilon_d} \right)^{3/2}, \tag{4.6}$$

where ϵ_m and ϵ_d denote the dielectric functions of the metal and the adjacent dielectric medium, respectively, k_0 is the wavevector of light in free space. From this, the propagation length L_{SPP}, is found to be

$$L_{\mathrm{SPP}} = \lambda_0 \frac{(\epsilon_m')^2}{2\pi(\epsilon_m'')} \left(\frac{\epsilon_m' + \epsilon_d}{\epsilon_m' \epsilon_d} \right)^{3/2}. \tag{4.7}$$

From Eq. (4.7) one can realize that for a long propagation length we require a large (negative) real part , ϵ_m', and small imaginary part ϵ_m'' of the relative permittivity of the metal, i.e., we need a low-loss metal.

Experimentally, the propagation length is estimated from the energy decay length of SPP propagation along the interface; that is, the intensity of the SPP field at a point x along the propagation direction is given by

$$I_{\mathrm{SPP}} = I_0 e^{-x/L_{\mathrm{SPP}}}. \tag{4.8}$$

By fitting the propagating SPP intensity, outside the excitation beam area, with a monoexponential decay we obtain the real value of L_{SPP}. From the $\Delta R/R$ image presented in Fig. 4.4(b) we have extracted and averaged 10 lines along the SPP absorption signature (in the X-direction) outside the launching spot. We have performed this operation for 2 other reflectance snapshots recorded in identical experimental conditions, but for different grating structures. The obtained profiles are shown in Fig. 4.6. Fitting the $\Delta R/R$ decays with a monoexponential decay (in log scale), we extracted the L_{SPP} values for each decay. The level variations of the plasmon decay seen in the Fig. 4.6 can be explained by a slightly different plasmon generation efficiency from grating to grating, causing accordingly a different electron heating. Comparing the experimentally obtained

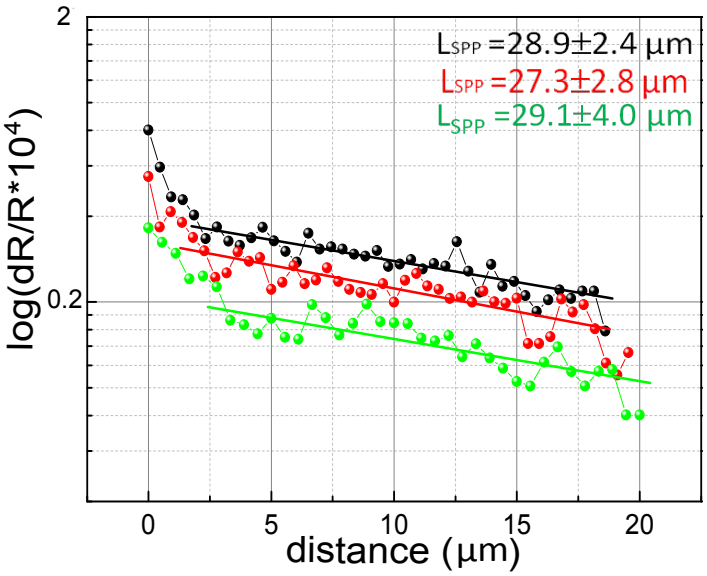

Figure 4.6: *Measured plasmon propagation length for gold/air interface at* λ_0 = 800 nm*; the curves represent profiles from three reflectance snapshots recorded in identical experimental conditions (*λ_0 = 800 nm*, pump waist* 4 μm, 10 mJ/cm^2*), but for different grating structures. The lines represent exponential fit to the profiles. First points have been not included in the fitting as they represent the tail of the excitation beam. The estimated average* $L_{\mathrm{SPP}} = 28 \pm 3\,\mu$m.

average value of plasmon propagation length $L_{\mathrm{SPP}} = 28 \pm 3\,\mu$m with the calculated value of $L_{\mathrm{SPP}} = 42\,\mu$m based on material optical constants (gold/air interface at $\lambda = 800$ nm and for $\epsilon_m = -22.1 + 1.77i$ from [107]) we conclude that, in our experiment, the SPPs have a stronger damping and consequently higher losses. One of the causes of higher losses could be the quality of the surface, i.e., presence of corrugations and roughness. Also is important the metal evaporation process. Thus, different approaches employed in the process of metal evaporation may give rise to substantial damping, as demonstrated in Ref. [135]. In their work the authors have shown that the SPP propagation length is the largest, and in agreement with optical constants, for single-crystalline Au. Much reduced propagation lengths were found for polycrystalline films, as additional loss mechanisms intervene from grain boundary scattering. More than twice reduction of L_{SPP} has been measured for polycrystaline Au with 80 nm grain size, and 10 times L_{SPP} reduction for the case of 20 nm grains.

4.4.3 Measuring group velocity of SPPs

One of the major motivations in the investigation of propagation and manipulation of electromagnetic surface modes is the possibility of designing highly integrated optical devices. And the uniqueness of this micro- and nano-scale devices is that they can operate at the local speed of light. This would facilitate information transport in extremely confined structures (beyond the diffraction limit) at incredible data rates.

In the previous section, we studied and put in evidence the excitation process of plasmons and then estimated their propagation length, which characterizes the plasmon propagation losses. Next, we proceed with the observation of propagation of surface electromagnetic fields and we try to estimate the propagation speed mediated by excited hot electrons.

4.4.3.1 Measuring SPP group velocity from snapshots

As femtosecond pulses are used to excite SPPs, femtosecond SPP wavepackets are created. When the SPP wavepacket is probed for different pump-probe delays, we can visualize it at different positions in time as it propagates along the metal interface. By exciting the plasmon with the pump beam on the grating structure, we have recorded reflectance snapshots for several consecutive pump-probe delays. Three snapshots measured at 140, 180 and 220 fs pump-probe delays are shown in Fig. 4.7. Every frame is a new scan of the measurement frame. The time delay between each frame is determined by the displacement of the delay line by $3\,\mu$m, corresponding to 40 fs. From this measurement sequence we can study the SPP dynamics directly. By following the absorption of SPP wavepacket in space , i.e., along the X-direction, we have averaged 5 lines in the region of the SPP signature. This procedure has been performed for each image from Fig. 4.7. The obtained profiles are shown in Fig. 4.8 for each time-frame. Each curve presents an exponential decay superimposed with some oscillations[1]. In order to estimate the group velocity we considered the sharp step-like wavefronts (marked by green dashed ellipses). By comparing to snapshots, we notice that these steps represent the positions which have been reached by the SPP-excited-hot-electrons at

[1]This oscillations are not understood yet. A possible explanation could be an interference pattern with the reflected part of the plasmon coming from an edge situated at $20\,\mu$m, out of the imaged field

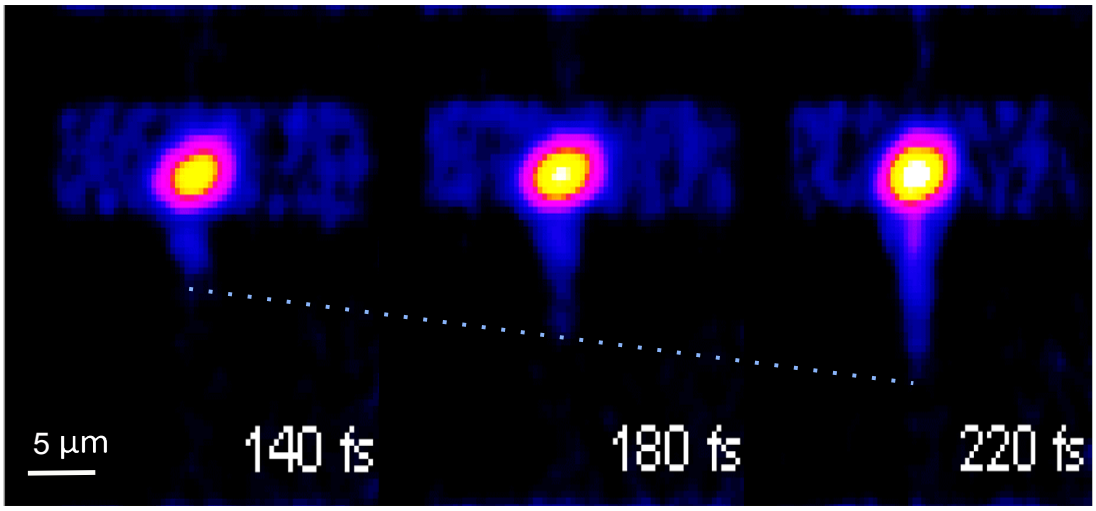

Figure 4.7: *Consecutive reflectance snapshots of the hot electron trace left by propagating SPP wavepacket. Succeeding frames are new scans of the probe. The time between two frames is* 40 fs. *The scan area is* $33 \times 33\,\mu\text{m}^2$.

the corresponding delay. Thus, in 80 fs (delay between the first and last frames) the distance propagated by the SPP wavepacket is $9.4\,\mu$m (estimated between the centers of the first and last steps). From these values, group velocity is estimated to be $v_g = (1.2 \pm 0.24) \times 10^8\,\text{m/s} = (0.4 \pm 0.08)c$, with c being the speed of light. This value is about 2 times lower than the expected one. For example, Temnov *et al.* [136] obtained experimentally SPP group velocity of $v_g = 0.92c$ at $\lambda_0 = 800\,\text{nm}$ for a gold/air interface. But we should bear in mind that we do not detect directly the SPP intensity, but the SPP absorption trough the hot electrons. The SPP lifetimes are of the order of tens of fs. The SPP decays generating in a first step a nonthermal electron distribution, which are thermalized to a hot electron gas (in internal equilibrium) through electron-electron scattering events. This last process takes place in time scales of hundreds fs, much slower than the SPP lifetimes. Another limiting factor present in our experiment, which could influence the lower experimental SPP group velocity is the pulse duration (150 fs). The phenomena we are looking at are shorter than or comparable with the pulse duration, which could introduce extra errors in our results.

It is also remarkable that, as we have mentioned previously, the hot electron transport takes place at the Fermi velocity and in gold it is $v_F = 1.4 \times 10^6\,\text{m/s}$: two

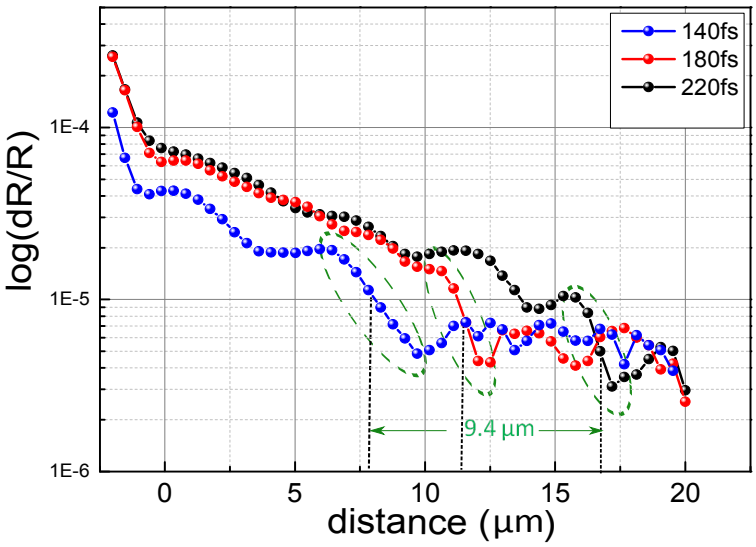

Figure 4.8: *$\Delta R/R$ profile, along the SPPs propagation direction, extracted from each frame from Fig. 4.8. the Consecutive reflectance snapshots of the hot electron trace left by propagating SPP wavepacket. Succeeding frames are new scans of the probe. The time between two frames is* 40 fs. *The scan area is* $33 \times 33\,\mu\text{m}^2$.

orders of magnitude lower than the SPP velocity. This value is also considerably lower than the experimentally estimated v_g of the SPP-excited hot electron trace. Thus, we can conclude that the measured propagation is not associated with hot electrons moving at v_F, and we do have a heat source which is moving along the interface at a speed of the same order of magnitude as the speed of light.

In the following experiment, we performed the imaging of the complete process, i.e., plasmon excitation of the hot electrons in the propagation direction, as well as their relaxation and diffusion. Fig. 4.9 presents recorded reflectance snapshots for increasing pump-probe delays. The pump-probe delay at which each frame has been taken is displayed on each image. As the temporal step between consecutive frames is bigger (comparing to the results presented in Fig. 4.7) the SPP tail appears almost instantaneously between the snapshots taken at 264 and 330 fs delay. In the next frames, in the plasmon tail region is observed an increase of the electron temperature (frames at 396, 462 and 594 fs) which is explained by the process of internal electron thermalization and the building up of the hot electron gas. Finally, the hot electron gas relaxes through electron-phonon cou-

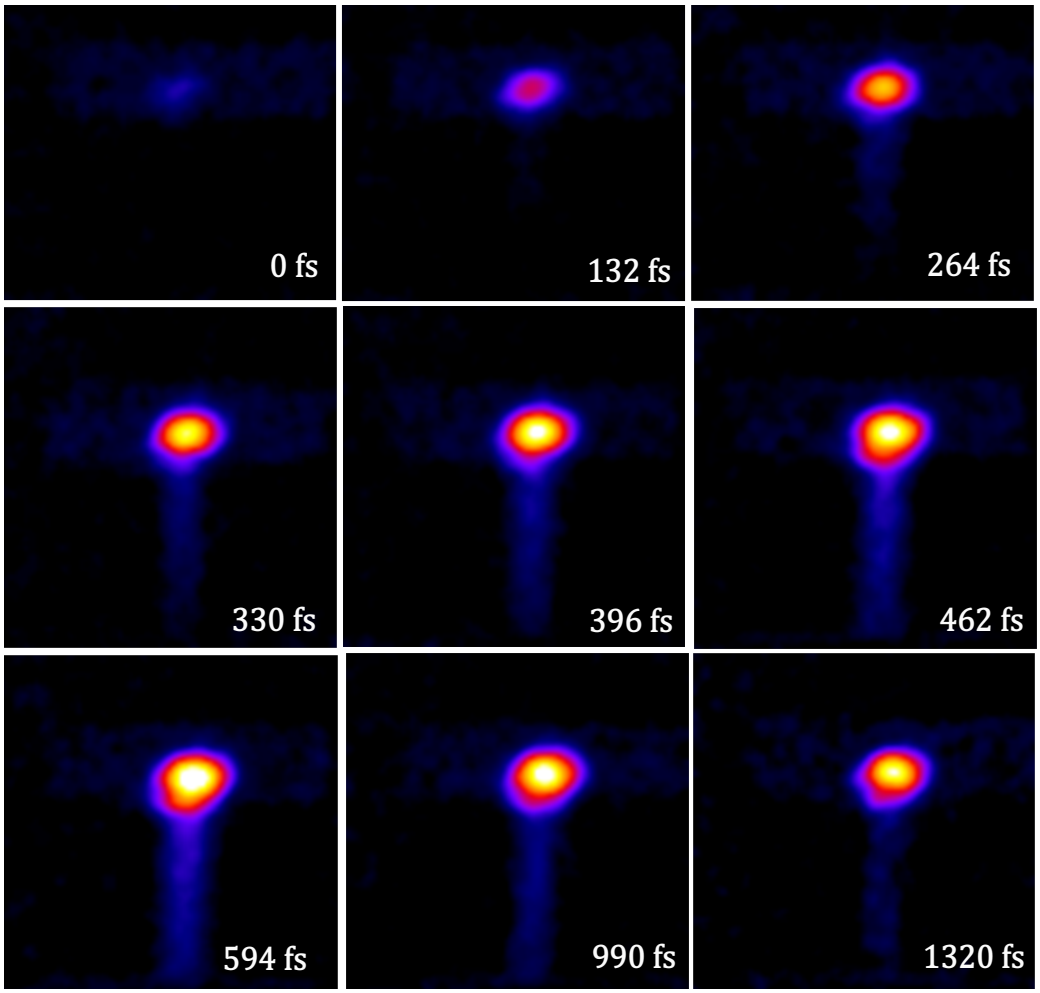

Figure 4.9: *Plasmon-excited hot electrons dynamics: consecutive reflectance snapshots of the hot electron trace left by propagating SPP along the taper structure, describing the process of the plasmon energy to hot electron conversion in time and space. Successive frames are new scans of the probe. The pump-probe delay at which each frame has been taken is indicated in the images. The scan area is* $33 \times 33\,\mu\mathrm{m}^2$.

pling and electron diffusion processes (frames at 990 and 1320 fs). Comparing to the thermal profile of the excitation beam, the hot electrons excited by the SPPs show a rather faster relaxation. In the last frame in Fig. 4.9, after 1320 fs, the plasmon thermal signature has almost vanished, while the excitation beam heating is still high. This effect is consistent with the two temperature model and experimental observations of electron-phonon thermalization process [71]. Thus, the higher is the electron temperature increase, the slower the system becomes and the longer the process of electron-phonon relaxation.

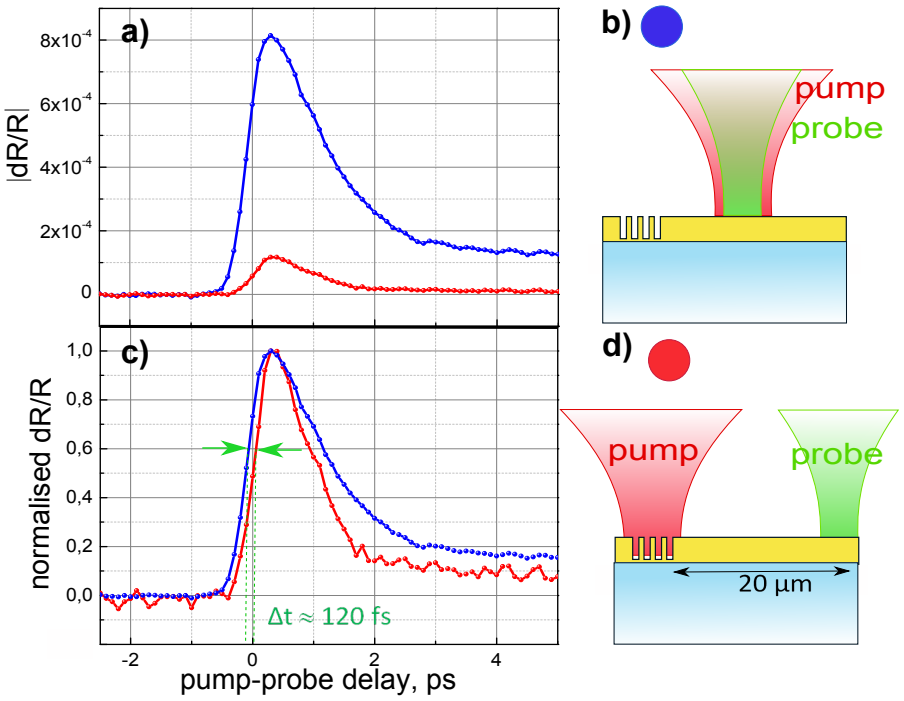

Figure 4.10: *Comparison of the $\Delta R/R$ time-resolved response of the pump excited and plasmon excited hot electrons:* ***(a) blue curve****: relative reflectivity change temporal response of a bare gold film measured in the experimental configuration depicted in* ***(b)****;* ***red curve****: temporal response when of SPP-excited electrons measured in the experiment depicted in* ***(d)****;* ***(c)*** *the curves from* ***(a)*** *normalized. The delayed rise of the red curve is attributed to the time it takes for the SPP to travel the distance of* $20\,\mu$m.

4.4.3.2 Measuring SPP group velocity from point measurements

We performed a second experiment to estimate SPP velocity by time-resolved point measurements.

For this, two comparative studies have been done [Fig. 4.10(c, d)]. For the first one, we spatially overlap the pump and probe beam on gold film (aside from the grating structure) and we record its time-resolved response (Fig. 4.10(a): blue curve). In a second experiment, we focus the pump beam on the grating and focus the probe on the SPP thermal tail at $\approx 20\mu m$ distance away from the grating. Again we record the temporal response at this point [Fig. 4.10(a): red curve]. It is obvious that the amplitude of the reflectivity change is considerably higher when all the energy is absorbed by the metal and we detect the heating

at the same location. On the other hand, when the same power is directed onto the grating, only a fraction of it (25-30%) is converted into plasmons and launched along the interface. Subsequently, this launched energy is absorbed while propagating, and the red curve in [Fig. 4.10(a)] represents what remained after a 20 μm propagation.

An important quantity is brought to light by normalizing the two curves [Fig. 4.10(b)]. Specifically, by comparing the two curves, we observe that the electron absorption process (the rising slope of the dR/R peak) when probing at 20 μm away from the SPP source has, a delayed start with $\approx$ 120 fs compared to the case with pumping and probing at the same location. This delayed rise is attributed to the time taken by the SPP to travel the distance from the point where they are generated (pump location), to the point where their absorption is detected (probe location). In this way we estimate a velocity of v_g=$(1.66 \pm 0.33) \times 10^8$ m/s = $(0.55 \pm 0.11)c$. We should point out that when pumping and probing in the same location, even for various pump fluences, the rising part of the peak has always the same slope and starting point (see, for example Fig. 3.6(a)). In contrast, the electron-phonon relaxation decay is dependent on the injected power.

4.5 Conclusion

In this chapter, we investigated the time-resolved response of hot electrons created by surface plasmons absorption. For a more efficient SPPs generation and a more confined launching SPPs source we have used a metallic sub-λ slits-array.

Imaging the relative reflectivity changes induced by plasmon-excited hot electrons, we could visualize the absorption of SPP wavepackets at different positions with time, as they propagate along the metal interface.

We characterized qualitatively the absorption-mediated SPP signal and estimated the propagation length of the excited SPPs to be $L_{\mathrm{SPP}} = 28 \pm 3\,\mu$m.

From the spatio-temporal study of the SPP wavepackets and hot electron dynamics, we have determined the SPP group velocity of $v_{\mathrm{g}} = (1.2 \pm 0.24) \times 10^8$ m/s and $v_{\mathrm{g}} = (1.66 \pm 0.33) \times 10^8$ m/s, values estimated from reflectance snapshots and point-measurements, respectively.

CHAPTER 5

Plasmon focusing

Until now we have only studied the plasmon propagation in semi-infinite metallic films. The plasmon is only confined beneath the surface of the propagating media. In this final chapter we go even further in guiding structure able to confine plasmonic energy at the end of a tip. This plasmon focusing is accompanied by strong wavelength reduction. As the confinement occurs the energy density increases and thus the absorption. A huge amount of plasmon energy is transmitted to the electron bath.

In this part we demonstrate the possibility to achieve nanofocusing of hot electrons with a laterally tapered metal waveguide (taper) on a dielectric substrate. Thus, it is possible to obtain a nano scale heat source in our plasmonic system.

We further study the temporal evolution of both the hot electron spot heating and relaxation dynamics along the entire taper structure. The time dependent thermal properties of our plasmonic device are studied by performing pump-probe delay dependent reflectance snapshots. In this way we reveal a slowing down of electron thermalization approaching to the tip apex. These effects are explained by the adiabatic plasmon nanofocusing phenomenon and the consequent SPP group velocity reduction

Contents

5.1 Introduction

Important changes have taken place in nanoptics over the past decades, which have been possible mostly because of the use of highly localized plasmon resonances [137–139]. In particular, the possibilities to efficiently deliver energy in the optical and near-infrared spectral regions to nanoscale objects, to concentrate this energy within spatial regions with dimensions as small as a few nanometres, and to manipulate and guide light signals using nanoscale waveguides and optical devices is the key of the rapid development of the subwavelength metal optics. Thus, as a next step in this work, we advance in hot electron manipulation and consider efficient ways to transform plasmons into hot electrons.

In previous chapters we have demonstrated that detection of hot electrons excited by SPP may contain quantitative information on the absorbed energy. Next, we have shown that we are able to follow the temporal evolution of plasmon-generated hot electrons. From the absorption signature, we have estimated the characteristic quantities of the SPP, namely the SPP propagation length L_{SPP} and group velocity v_g, and we obtained values in good agreement with those expected from theory. In this final chapter we present a study of the SPP nanofocusing process and strong field localization in a specially designed focusing metal structure. We image the SPP "concentration" and absorption dynamics in time and space. Through SPP energy conversion to hot electrons we are able to obtain an extreme sub–λ confined hot spot. As we employ femtosecond pulses to launch femtosecond SPP wavepackets, in this case we would obtain a confined heat source on picosecond time scales, opening up the possibility of adding some important additional functionality to plasmonic devices and circuits.

5.2 Localization and nanofocusing of electromagnetic field

5.2.1 Plasmon nanofocusing

One of the remarkable characteristics of SPPs, mentioned and explained in Chapter 1, is their extreme confinement and ability to concentrate light in deep subwavelength volumes. It becomes possible to achieve the concentration, the lo-

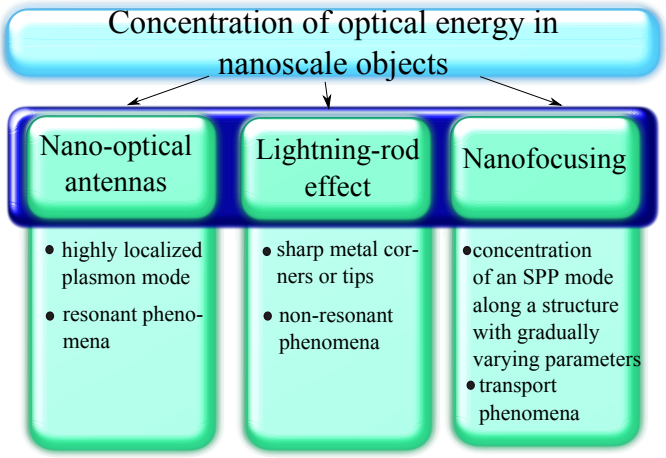

Figure 5.1: *Plasmon-related phenomena responsible for concentration, localization and enhancement of electromagnetic energy within nanoscale spatial regions*

calization and consequent enhancement of optical fields within nanoscale spatial regions by means of three different plasmon-related phenomena: namely, nano-optical antennas, the lightning-rod effect and nanofocusing (see Fig. 5.1.).

Optical antennas are nano-optical resonators, and are represented by metal nanoparticles or nanostructures (e.g., short metal nanowires). These nanostructures support highly localized plasmon modes [140]. Illumination of the optical antenna at a resonant frequency can cause strong resonant enhancement of the localized near field of the supported plasmonic mode. In this way, optical radiation can be coupled into the strongly localized and enhanced local field of the plasmonic mode.

The ***lightning-rod effect*** is a non-resonant (broadband) phenomenon that involves the strong enhancement of the local near field of incident radiation in the vicinity of a sharp metal corner or tip, as a consequence of the high local charge densities present near such structural elements [141, 142].

Plasmon ***nanofocusing*** is the gradual concentration in a nanoscale spatial region of an SPP mode, with a particular polarization and symmetry, as the mode propagates along a tapered plasmonic waveguide with progressively varying parameters [143–146]. This process is not directly related to the interaction of incident radiation with metallic nanostructures, but it is defined as a transport phenomenon in which the gradual energy concentration, field localization and amplitude enhancement of the SPP along the propagation direction takes place.

Therefore, we should distinguish the process of SPP nanofocusing, which is defined as a *transport phenomenon*, from the lightning-rod effect and resonances in nano-optical antennas, which are caused by the localized *interaction of incident radiation with metallic nanostructures*.

5.2.2 SPP nanofocusing configurations

In this section we address specifically the process of SPPs nanofocusing and the way it can be achieved. Following [147], in Fig. 5.2 are listed some typical examples of nanofocusing structures. For every structure, there are corresponding characteristic SPP modes subjected to nanofocusing. The nanofocusing configuration types in Fig. 5.2 have been organized into three groups, according to the arrangement of metal and dielectric media involved.

We can distinguish insulator-metal-insulator (IMI) structures, metal-insulator-metal (MIM) structures, and metal-insulator-insulator (MII) structures[1]. The exemplified structures include: a) tapered metal rods [144, 149, 150], b) metal strip with tapered width and constant thickness [151, 152]; c) cylindrical metal crescent [153]; d)tapered metal films on a dielectric hemisphere [154]; e) metal wedge on a dielectric substrate [155]; f) tapered gaps [143, 156, 157]; g) closely spaced or touching metal spheres [158] or, h) dielectric wedge on a metal substrate [159]. Each of these structures supports certain types of plasmon modes [147]. Theoretically and experimentally, most commonly studied structures are the IMI structures, confirmed also by the bigger variety of the structural designs. The dimensions of the region of SPP concentration in a nanofocusing structure are limited by the SPP wavelength (or by some fraction of it) near the tip of the taper. Thus, nanofocusing can be regarded as diffraction limited by the SPP wavelength near the tip. However, the SPP wavelength near the taper tip can be as small as a few nanometers, which is much smaller than that in vacuum or any known dielectric medium. This is the physical origin of the very strong field localization near the tip.

The taper of the nanofocusing structures listed above, plays a similar role to the converging wavefront of an electromagnetic wave as the situation when it

[1]Hybrid nanofocusing structures have also been demonstrated, combining the features of e.g., IMI and MIM configurations [148].

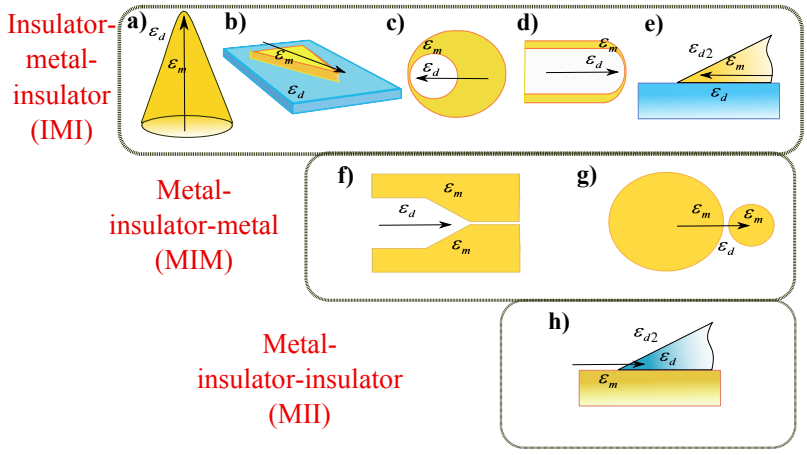

Figure 5.2: *Nanofocusing configurations.* ***Insulator-metal-insulator:a)****tapered metal rods;* ***b)*** *metal strip with tapered width and constant thickness;* ***c)*** *cylindrical metal crescent;* ***d)****tapered metal films on a dielectric hemisphere;* ***e)*** *metal wedge on a dielectric substrate;* ***Metal-insulator-metal: f)*** *tapered gaps;* ***g)*** *closely spaced or touching metal spheres;* ***Metal-insulator-insulator: h)*** *dielectric wedge on a metal substrate.*

passes through a dielectric lens - it gradually concentrates the energy, localizes the field, and enhances the amplitude of the SPP along the propagation direction. However, whereas the diffraction limit of light limits the minimum achievable focal spot size using a dielectric lens to about half the wavelength in the medium, the minimum focal spot size for a nanofocusing structure can be as small as a few nanometers, being limited only by the atomic structure of matter and the non-local electronic response (spatial dispersion). This makes nanofocusing an essential link between diffraction-limited optics and nanoscale structures (including biological objects), nanoelectronic devices and even individual molecules.

Another common characteristic of the SPP modes is their significant dissipation in the guiding metallic structures. As they propagate along a nanofocusing structure in the direction of focusing, SPP localization increases. The SPP dissipation increases with increasing SPP localization. The resulting dissipative energy losses along a nanofocusing structure could exceed 90% [150]. Nevertheless, this does not negate the possibility of strong local field enhancements (up to $\sim 10^3 - 10^4$) for the field amplitude [144, 150] near the tip of nanofocusing structures with sufficiently short tapers. Thus, the local field enhancement along the taper may efficiently compensate for the dissipative reduction of the SPP

amplitude. As a result, even if the significant dissipation of strongly localized SPP modes cannot be compensated or significantly reduced, nanofocusing still remains a viable technique with a broad range of practical applications.

Finally, in addition to the strong localization of optical energy, nanofocusing is typically associated with a significant reduction of both the phase and group velocities of the SPP mode [144, 145]. Thus, in nanofocusing structure, via the transformation and confinement of the SPP modes, a significant group velocity reduction is achieved [143, 153]. For a conical gold taper, by using femtosecond time-domain interferometry, a reduction of the SPP group velocity up to $v_g = 0.2c$ has been predicted and measured [160]. Accordingly, nanofocusing device geometry enable the realization of broadband SPP-based "slow light" applications including broadband absorbers [161] and light harvesting devices [153].

5.2.3 Adiabatic and non-adiabatic nanofocusing

The physical processes that occur during SPP propagation along a tapered metallic waveguide are strongly influenced by how rapidly the structural parameters vary along the waveguide, which are determined by the taper angle γ. For sufficiently small taper angles, the so-called ***adiabatic*** approximation is applicable.

The adiabatic condition states that the variation of the SPP wavelength λ_{SPP}, over *one* SPP wavelength, is small relative to λ_{SPP} wavelength. This approximation assumes that a propagating SPP does not "feel" the taper, so that the SPP characteristics at any point along the taper are determined by the local structural parameters (e.g., the local diameter of a tapered rod). The SPP simply adjusts itself (by becoming increasingly localized) in accordance with the changing local waveguide parameters. Under these conditions, there is negligible reflection and scattering of the SPP mode from the taper, and damping channels other than absorption in the nanofocusing structure are significantly reduced.

In the opposite case, if the taper angle γ is significantly larger than the optimal value imposed by adiabatic condition, the SPP reflection and scattering from the taper increase because of structural ***non-adiabaticity***, so that the magnitude of these effects becomes dominant. Consequently, for linear tapers, there exists an optimal taper angle γ_{opt} that maximizes the field enhancement at the tip. Decreasing the SPP frequency reduces the critical taper angle, mainly because

this increases the absolute value of the real part of the metal permittivity ϵ'. For example, for a tapered gold rod, increasing the vacuum wavelength from 632.8 nm to 1600 nm caused γ_{opt} to decrease from ~ 35° to ~ 8° [162].

5.3 Plasmon modes in a laterally tapered metal waveguide

Every nanofocusing configuration structure relies on shrinking the transverse dimensions of a plasmon mode. Hereafter, we consider the nanofocusing structure shown in Fig. 5.2(b): a laterally tapered metal stripe of constant thickness on a dielectric substrate. In the following we address the plasmon modes possible to be excited in such a structure together with their properties.

A metal film embedded in an asymmetric dielectric environment (e.g. air/ gold/ glass) supports modes localized at different sides [163, 164] which generally have different properties, as sketched in Fig. 5.3(a). On a metal film of infinite lateral extension, two types of SPP modes can be excited:

- ***Asymmetric mode:*** It is the purely bound SPP mode that has most of its field energy localized in the high-index substrate. It is called asymmetric since its transverse electric field has opposite signs at either side of the metal film. The signs of the surface charge at both metal/dielectric interfaces are equal for this mode.

- ***Symmetric mode:*** It is the mode propagating predominantly at the low-index side of the film. It has electric fields with equal signs at both sides of the film, and is therefore called symmetric. Accordingly, the surface charges at both interfaces associated with this mode have opposite signs.

For our following studies, we follow the work of Verhagen *et.al* [151] as a basis. In this work the authors investigated the focusing of SPPs in a tapered Au waveguide in an asymmetric dielectric environment, both experimentally (by detecting the upconversion luminescence intensity from erbium ions implanted in the substrate) and through simulations. They found that strong field confinement and concentration at the taper tip is possible when the asymmetric SPP mode propagating at the substrate side of the metal film is excited . The

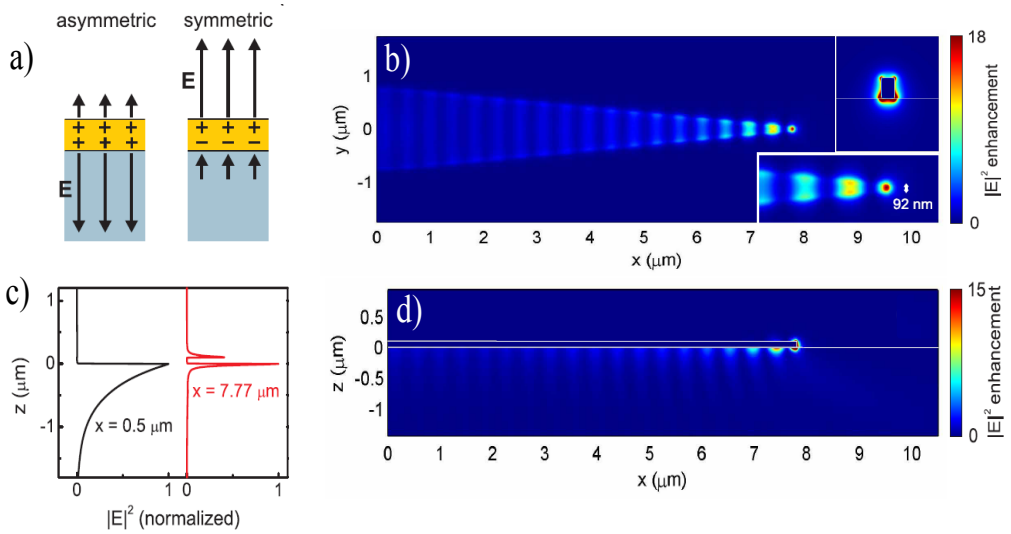

Figure 5.3: *Plasmon modes supported by a laterally tapered metal waveguide in an asymmetric dielectric environment:* ***a)*** *Sketch of the electric field of the two SPP modes in an extended metal film, showing the symmetry of the transverse electric field and the surface charge. the direction of propagation of SPP is normal to the image plane.* ***b)*** *FDTD simulation results of the electric field intensity distribution along a gold* $7.8\,\mu$m *long taper for the horizontal cross section view at* 35 nm *distance inside the substrate and respectively* ***(d)****- the same as in* ***b)*** *but a vertical cross section through the structure;* ***c)*** *Normalized vertical cross sections of* ***d)*** *at the start (*x = $0.5\,\mu$m*), black), and at the end* x = $7.7\,\mu$m *(red curve), showing the increase in vertical confinement and the intensity build up at the air interface. Figure taken from [151].*

propagation and concentration of this mode to the tip was demonstrated and no cutoff waveguide width was observed as the SPPs propagate along the taper. Through simulations they have shown that such concentrating behavior is absent for the leaky SPP mode that propagates predominantly at the air side of the metal, which is also the mode that is usually studied in near-field experiments [165, 166]. The results of the simulations for the bound (gold/substrate) and leaky (gold/air) modes of this work are shown in Fig. 5.3. In Fig. 5.3(b) and (d), the FDTD simulation results of the electric field intensity distribution along a $7.8\,\mu$m Au taper in an asymmetric dielectric environment are reproduced, respectively for the horizontal cross section view at 35 nm in the substrate (b) and vertical cross section view through the structure (d). The simulation results prove that the mode energy is mainly confined at the Au/substrate interface and

it does not experience any cutoff while approaching the tip apex. The insets in Fig. 5.3(b) shows in detail the vertical and horizontal field distributions at the tip end.

Clearly, the field is truly concentrated to nanoscale transverse dimensions, remaining tightly confined to the metal surface. The upper inset also shows that for very narrow widths, a significant intensity builds up at the air side of the metal film. This is further illustrated in Fig. 5.3(c), which shows a cross-section of the field intensity at the beginning of the taper ($x = 0.5\,\mu$m, black curve) and at the taper tip in the plane ($x = 7.7\,\mu$m, red curve), where the Au taper width is only 60 nm.

5.4 Sample design and fabrication

Based on the analysis of the previous experimental and theoretical studies of nanofocusing properties of plasmon modes, we have chosen to design a laterally tapered plasmon nanofocusing structure (throughout this work called "taper"), in which we excite the bound asymmetric mode at the gold/substrate interface.

The designed structure is sketched in Fig. 5.4. Before fabricating the taper, we have accounted for some structural optimization. The metal we use is gold, as we have already acquired knowledge and understanding of the plasmon and hot electron related phenomena and dynamics in this material. The second major cause in choosing gold is the spectral location of the electron transitions from the top of the d-band to Fermi level ($\sim$ 2.4 eV), which is attainable for our available laser source. These electron transition are crucial for our experiment as we probe the conduction hot electron temperature increase which follows the plasmon absorption.

Comparing to the studies of SPPs excited hot electrons in previous chapters, where we have always probed the gold/air interface, for the taper structure we need to probe the gold/substrate interface. In this case, the type of adhesion material used between the metal and the substrate during the process of sample fabrication has a crucial importance. The commonly used adhesion material (also used in the fabrication of previous samples) is titanium. But a Ti-layer at the gold/substrate interface strongly damps the plasmon at this interface. With this in mind, the solution has been found by replacing the Ti with SU-8

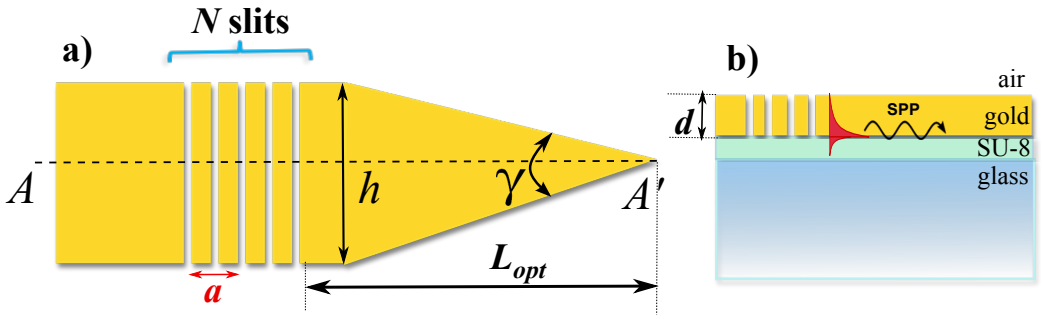

Figure 5.4: *Nanofocusing plasmonic device design:* ***a)*** *Horizontal cross section of the structure indicating the major structural parameters:* a*-grating period,* L_{opt}*-the active length of the tip, considered from the last grating slit,* h *taper-width,* γ*- taper angle.* ***b)*** *vertical cross section along* AA'*, indicating the air/Au/SU-8/glass structure and we mention that we want to excite the SPP at the gold/SU-8 interface. The dimensions of the structure are* L_{opt}*=8, 11, 12* μm*,* $h = 4\,\mu$m*,* $\gamma = 28°$*,* $d = 140\,$nm*,*

polymer. The SU-8 photoresist has a refractive index of $n = 1.57$ in the range of $\lambda = 600 - 800\,$nm, which is close to the one of the glass substrate.

A grating structure has been selected as a plasmon launching source, which couples efficiently the incident far-field radiation into plasmons. Also reasoning in terms of experimental conditions, it would be more convenient to have the pump (exciting the SPPs) and the probe (detecting the SPPs absorption) beams being incident on the structure from opposite sides. This situation allows an independent adjustment of the two beam waists. Considering the above arguments, the optimal configuration is the one in which the pump is incident from the air side on the grating, excite the SPPs at the gold/SU-8 interface, while the probe detects the SPP's excited hot electrons at the latter interface.

Using the aperiodic-Fourier Modal method [103], we have optimized the metal film thickness (140 nm) (an important parameter), the slit width ($w = 200\,$nm), the number of slits ($N = 8$) and the grating period ($a = 485\,$nm) to optimize the SPP excitation efficiency (= 30%) at the pump frequency under normal illumination and for a pump beam diameter of $3\,\mu$m.

Once the SPP mode is excited at the grating structure, it propagates along the taper and gradually gets concentrated. For an efficient mode concentration we also need to account for other structural parameters of the taper-structure. There is an optimal length L_{opt}, an optimal distance from the tip, at which SPP should

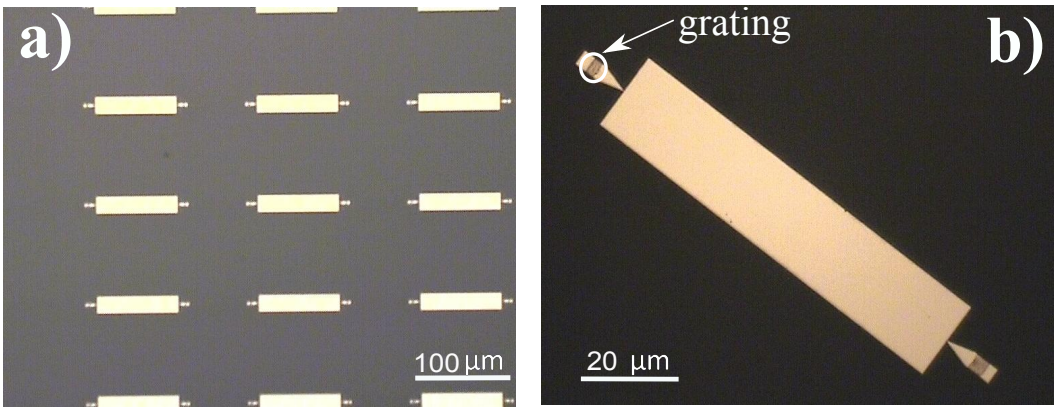

Figure 5.5: *Microscpe images of the fabricated sample:* ***a)*** *Image of a* 4×7 *array of structural elements containing the nanofocusing tapers.* ***b)*** *one element of the array from* ***(a)****. A single element of the fabricated arrays consist of two tapers facing* $20 \times 100\,\mu\text{m}^2$ *gold plate. The darker region in the middle of the taper represents the grating of the period* a = 485nm *and the slits width, forming the grating, being* w = 200 nm*. The gold plate and the taper are separated by gaps of* 20, 30, 40 *and* 50 nm*.*

be generated to maximize the local field enhancement at the tip. Physically, L_{opt} is the distance from the tip of the structure at which the rate of increase of the SPP amplitude is canceled by the rate of the amplitude decay because of dissipation in the metal, as a result of structural energy concentration. If an SPP is generated at a distance $L > L_{\text{opt}}$, dissipation losses will reduce the achievable field enhancement at the tip, whereas if an SPP is generated closer to the tip, the effect of structural energy concentration will not be fully utilized by the structure. In establishing the L_{opt} we took as a reference the plasmon propagation length at this interface. Thus, for a vacuum wavelength of λ_0 = 800 nm, the SPP at the gold/SU-8 interface has an $L_{\text{SPP}} \approx 10\,\mu$m. Accordingly, for the fabrication process has been chosen to be fabricated structure of $L_{\text{opt}} = 8, 11, 12\,\mu$m. However, all the results presented in this work are obtained for the taper structures of $8\,\mu$m and the height of the structure $h = 4\,\mu$m. In this case the taper angle is about $\gamma = 28°$.

The fabricated[2] laterally tapered arrays of 4×7 nanofocusing structures are shown in Fig. 5.5. In this figure, optical microscope images of fabricated structure

[2]The samples have been fabricated by Buntha Ea-Kim at Laboratoire Charles Fabry in Palaiseau, France.

are presented; Fig. 5.5(a) represents the array and Fig. 5.5(b) represents one element of the array. A unit element of the fabricated arrays consist of two tapers facing a $20 \times 100\,\mu m^2$ gold ribbon. The darker region in the middle of the taper represents the grating. The gold plate and the taper are separated by air gaps of 20, 30, 40 and 50 nm. The presence of the gold ribbon is motivated by our interest to also study the energy transfer through nanogaps.

5.5 Results

5.5.1 Experimental description

The experiment we performed is schematically depicted in Fig. 5.6. A pump pulse (800 nm, beam waist $4\,\mu m$, $2\,mJ/cm^2$) is incident onto the grating structure. The period of the grating (a = 485 nm) is chosen such that the TM-polarized light with a wavelength of 800 nm is diffracted to excite the purely bound SPP mode at the high-index side of the tapered waveguide.

In a similar manner as in the experiment described in Chapter 4, the incident light is dominantly reflected or absorbed. A fraction of this incident energy is launched along the metal/substrate interface as surface plasmons. The SPPs propagate along the tapered structure, and along the propagation direction gradually concentrating the energy and increasing the amplitude, while approaching the taper apex. All these processes happen simultaneously with the absorption of the plasmon mode. The absorbed energy heats the metal film. At the time scales which we detect the heating induced by the plasmons, all the energy is stored in the free electron gas.

We detect the reflectivity change, induced by the electronic temperature variation, with the probe pulse (532 nm 100X objective, NA=0.8, beam waist $0.8 - 1\,\mu m$, $1.5\,mJ/cm^2$), which raster scans the gold/SU-8 interface (the side of the Au film where the SPPs are excited). For a better understanding of the complex plasmon focusing process we performed the experiments for two configurations, as sketched in Fig. 5.6:

1. The pump is fixed and incident from the air, while the probe beam is incident from the substrate and is scanning the gold/SU-8 interface [Fig. 5.6 (a)]

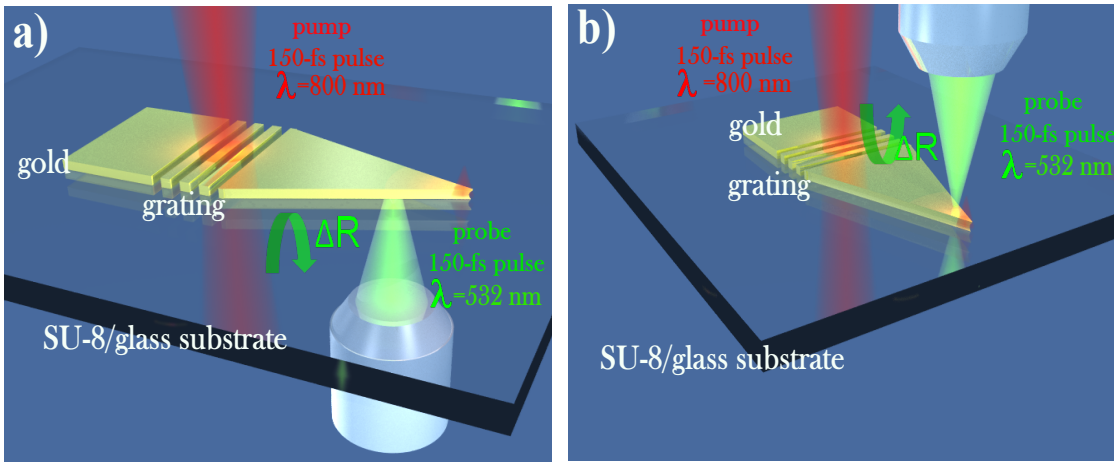

Figure 5.6: *Sketch of the focusing taper-experiment: A first laser pump pulse (λ = 800 nm, 150 fs FWHM) is incident on the array of sub-λ slits on the gold/air interface. A second laser pulse (λ = 532 nm) probes* ***(a)*** *the gold/substrate interface and* ***(b)*** *the gold/air interface and records the reflectance variations ΔR with a controlled delay between the pump and the probe pulses.*

2. The pump is incident from the air, and the probe is scanning the same gold/air side [Fig. 5.6(b)]

In both geometries the pump is meant to excite the same SPP mode at the high-index interface.

5.5.2 Plasmon focusing demonstration

5.5.2.1 Spatial response

In this section we demonstrate the possibility to achieve a localized source of hot electrons with a laterally tapered metal stripe waveguide on a dielectric substrate, through SPP to hot electron conversion at the tip apex.

For this purpose, we use the visualization system to image the taper structure through the substrate. Next, we locate the grating structure on the taper and we focus the pump beam on it. The excited SPPs are subsequently coupled into the laterally tapered waveguide etched in the Au film. To image the SPP field, which is predominantly localized at the substrate side, the probe beam raster scans the sample and records the relative reflectivity changes at a fixed pump-probe delay.

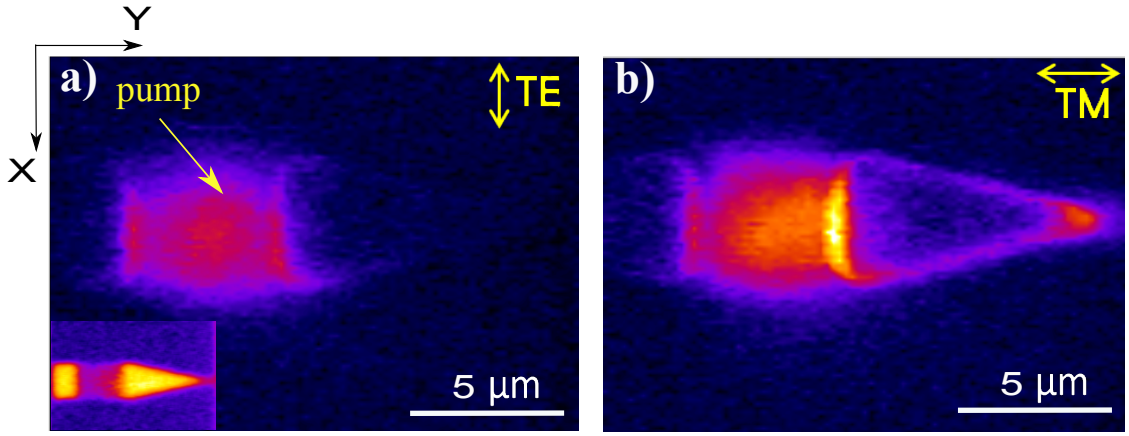

Figure 5.7: *Reflectance snapshots of the taper structure after a pump pulse excitation.* ***(a)*** *Image obtained for TE polarization, when the energy is not coupled to plasmons, so we do not observe any plasmon-absorption signature along the structure.* ***(b)*** *The same structure from* ***(a)*** *but for a TM polarization of the pump beam; The SPP propagation (from left to right) is clearly visible and leads to an intense hot spot at the taper termination. The inset in* ***(a)*** *represents a reflectivity image of the region being imaged, in the absence of any pump, and we can easily locate the taper structure and grating structure as the region with a lower reflectivity.*

We perform these measurements for two polarizations of the incident pump: TM and TE. The presence for TM/absence for TE of the thermal signature represents major evidence for the plasmonic character of the signal we detect.

In Fig. 5.7 snapshots of the reflectivity changes at a ~ 800 fs pump-probe delay for an excitation fluence of 2 mJ/cm^2 are presented. For the taper structure, the maximal reflectivity changes have been detected at the taper apex for ≈ 800 – 900 fs pump-probe delays, whereas , this was detected at a pump-probe delay of ~ 500 fs for the experiments employing slits and grating structures in a semi-infinite gold film. This effect will be analyzed and discussed in the following sections. Another significant difference with previous experiments is that we use about 10 times less incident pump fluence to obtain a rather high electron temperature increase along the taper.

Figure 5.7(a) shows the snapshot when the incident light is TE polarized. The thermal signature in the image, indicated by the arrow, can be recognized as the thermal profile of the excitation spot on the grating structure. To indicate the position of the taper in these figures, the inset in Fig. 5.7(a) shows an image

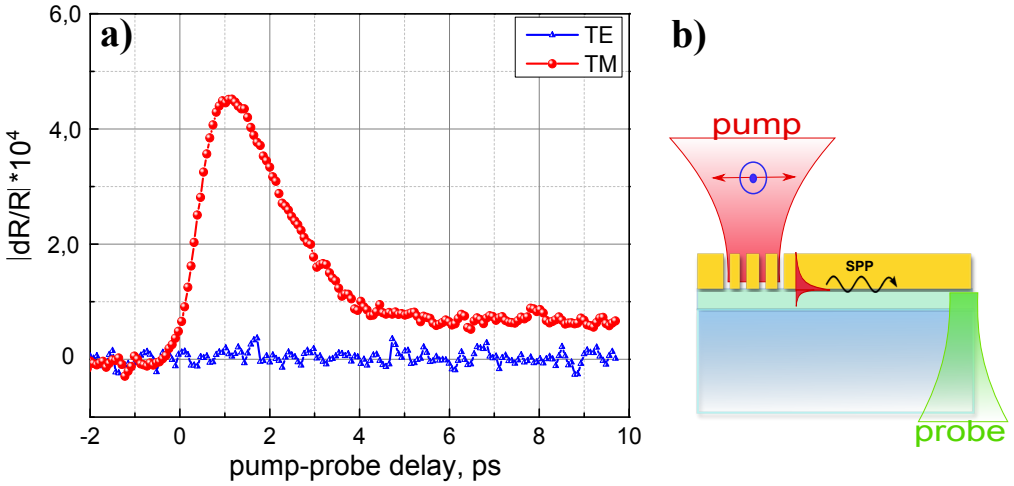

Figure 5.8: *Comparison of the $\Delta R/R$ time-resolved response for TM and TE polarized pump beam:* ***(a)*** *the resolved response when probe is focused onto the hot spot at the tip apex for a TM-polarized pump (red curve) and TE-polarized (blue curve);* ***(b)*** *the sketch of the experiment performed to obtain the curves in* ***(a)****.*

of the same scan area obtained by collecting normal-incident reflected light in the absence of the pump. We observe that for a TE-polarized pump, no heating takes place along the taper. In contrast, when we change the incident light polarization to TM [Fig. 5.7(b)], the SPP propagation (from the left to the right) is clearly visible and leads to an intense hot spot at the taper termination. As a result, a local thermal hot spot is generated, through supposedly SPP to hot electron conversion .

5.5.2.2 Temporal response

Another verification of the hot spot behaviour and origins was performed with temporal measurements. In the first step, when the pump beam is focused onto the grating, we record an image of the antenna. On the image we locate the position of the hot spot, and we center the probe beam on the hot spot (configuration sketched in Fig. 5.8(b)). In this configuration, we record the time-resolved response of the $\Delta R/R$ signal at the tip apex as a function of the pump-probe delay. The resulted response is shown in Fig. 5.8(a) (red curve). We observe that the maximum amplitude, i.e., the maximum electron temperature T_e variation, takes place ~ 1 ps. Next, we change the polarization of the pump from TM to

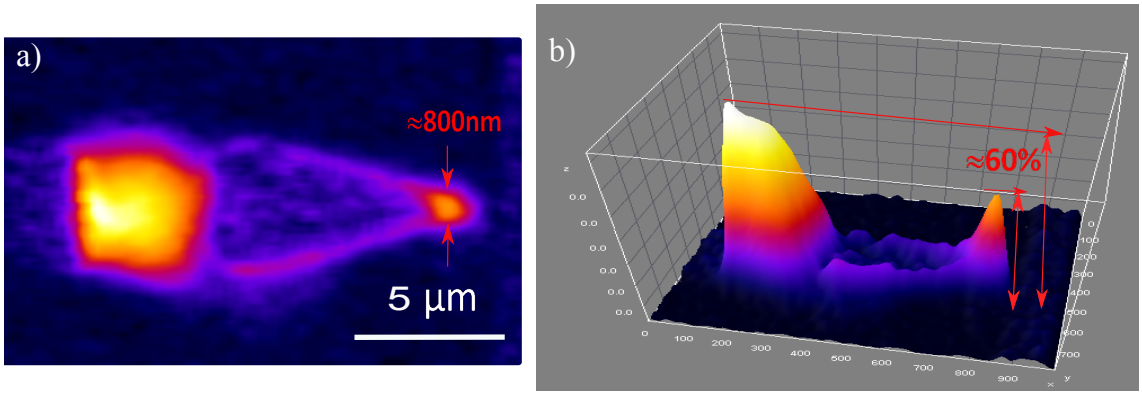

Figure 5.9: *Reflectance snapshots of the taper structure after a pump pulse excitation:* ***(a)*** *the reflectance image taken at a pump-probe delay corresponding to the maximal signal at the taper apex;* ***(b)*** *the 3D profile of the image from* ***(a)****.*

TE (being careful to readjust the pump power before the microscope objective) and we again record the time-resolved response. As expected, there are no excited hot electrons present, which is proven by the experimentally recorded curve (blue) in Fig. 5.8(a).

5.5.2.3 Qualitative hot spot characterization

In Fig. 5.9 we present a thermoreflectance snapshot taken at a pump-probe delay corresponding to the maximal signal at the taper apex. From this image we deduce that the spot of maximum intensity is achieved within the last 800 nm of the taper, where the lateral width of the structure is less than 200 nm. The amplitude of the reflectivity variations in this spot is more than 4 times larger than at the start of the taper and also much larger than the one along the edges of the rest of the taper. The full-width at half-maximum of the created hot spot is ~ 800 nm, which is the diffraction limit of the probe beam. The precise determination for the location of the maximum of the hot spot intensity (with respect to the taper apex) is limited by the spatial resolution of the microscope.

The remarkable observation is that the amplitude of the reflectivity change in the hot spot reaches ≈ 60% (Fig. 5.9(b)) of the reflectivity variations in the grating (we should keep in mind that from all the energy deposited on the grating in the ideal case 30% of it is launched as plasmon along the taper). There are several factors which contribute to the generation of such a high absorption at

the tip apex, in particular:

- The taper length is $8\,\mu$m, smaller than the plasmon propagation length L_{SPP} at this interface, so that the SPP is weakly damped by the propagation along the taper.

- The SPP energy is boosted and accumulated at the taper apex by the slowing down of the plasmon.

- At the tip apex, because of the tight confinement, the plasmon is slowed down and even stopped. As a consequence, most of the energy is absorbed (back-scattering and out-of-plane radiation are very weak). Efficiency as high as 90% for dissipative energy losses has already been reported for nanofocusing structures [150]. Thus, there can be the situation in which almost all plasmon energy is dissipated as heat at the tip apex.

Finally, note that we do not know precisely the reason of the relatively large absorption on the longitudinal edges of the taper. We may invoke an enhanced SPP absorption due to additional surface recombination at grain boundaries [165, 167].

5.5.3 Probing the plasmon at gold/substrate interface

5.5.3.1 Spatial response at the substrate and air interfaces

To gain insight into the behavior of the excited plasmon mode, i.e., the process of focusing, absorption and the resulting hot spot generation, we study also the absorption along the taper structure, but at the gold/air interface. We use the experimental configuration in Fig. 5.6(b), where the pump is incident from the air, but the probe scans in the gold/air interface.

The experimental reflectance snapshot, obtained at this interface (using exactly the same experimental conditions used for recording the image in Fig. 5.9(a)), is shown in Fig. 5.10. In this case, two important observations can be made: first, there is no significant absorption in the taper, including at the longitudinal edges (at least at these time scales); second, although the structure is now probed from the air side, a clear hot spot generation is observed at the apex.

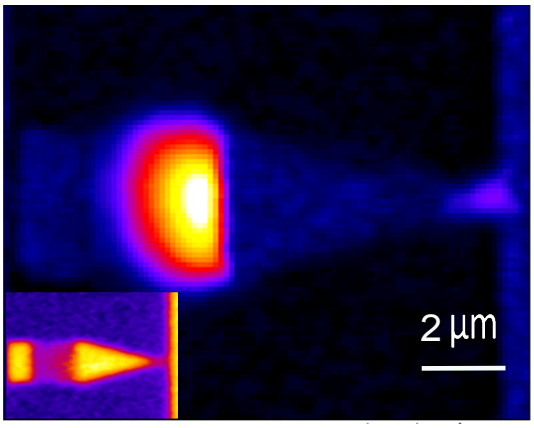

Figure 5.10: *Reflectance snapshot of the taper structure, at the* ***gold/air interface*** *after a pump pulse excitation, taken at a pump-probe delay corresponding to the maximal signal at the taper apex; the inset represents a reflectivity image of the region being imaged, in the absence of the pump-induced excitation, where we can recognize at the right border the beginning of the metal plate.*

This behavior is consistent with the simulations reproduced in Fig. 5.3(b,c,d), i.e., in the case of excitation of the SPP bound mode, most of the energy is localized at the gold/substrate interface (Fig. 5.3(c) vertical cross section at 0.5 μm, black line). However, while approaching the taper apex, the intensity builds up at the air side of the metal film (Fig. 5.3(c), vertical cross section at 7.7 μm, red). We observe a similar tendency for the SPP absorption trace in the recorded reflectance images.

In the experiments presented in Fig. 5.9 and Fig. 5.10, no indication is found that the mode propagating along the taper experiences a cutoff for any particular taper width. As we have mentioned in section 5.3, such a cutoff width was predicted to exist for the leaky SPP modes supported by a tapered waveguide at the air side of the metal film and the bound modes at the substrate side [164]. As a result, this mode could not exhibit focusing along a tapered waveguide. The fact that in the presented results no cutoff behavior is observed, suggests that this is the gold/substrate interface involved in the focusing.

5.5.3.2 Temporal response on both sides

The final comparative analysis of the plasmon-induced reflectivity variations along the taper at the low- and high-index interfaces has been performed by

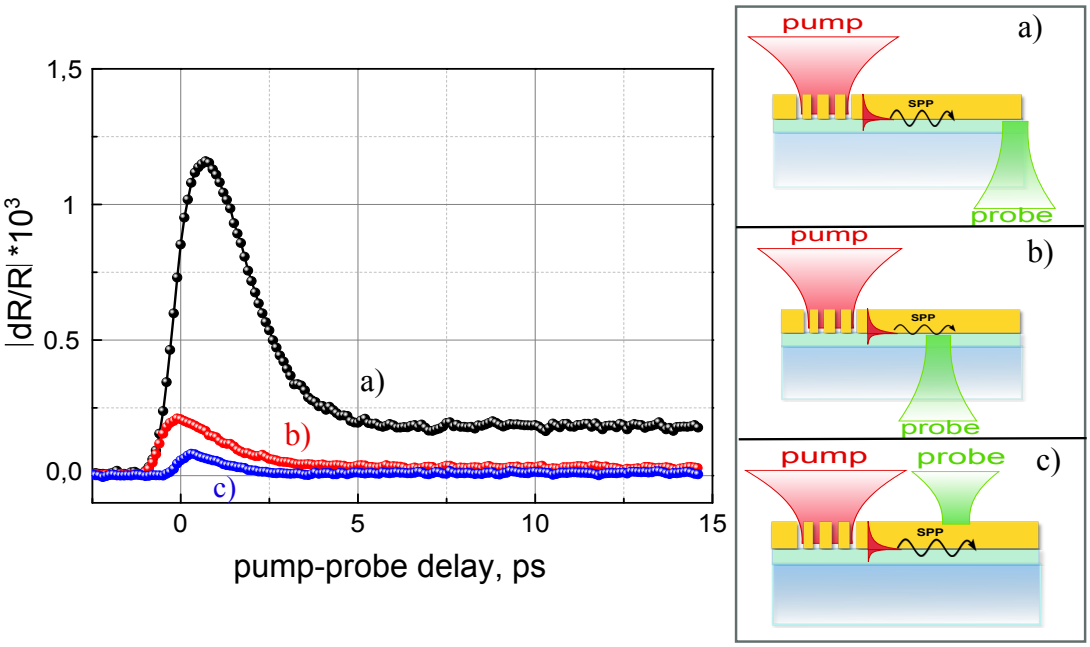

Figure 5.11: *$\Delta R/R$ time-resolved responses as a function of the pump-probe delay for* ***(a)*** *a probe incident on the gold/SU-8 interface and focused onto the hot spot;* ***(b)*** *a probe incident on the gold/SU-8 interface and focused at 4 μm distance from the grating;* ***(c)*** *a probe incident on the gold/air interface and focused at 4 μm distance from grating; In all measurements the pump incident on the grating is kept unchanged.*

employing the time-resolved measurements.

For the same incident pump fluence, we probe the $\Delta R/R$ time-resolved response twice: first, when the probe is incident through the substrate side, on the gold/SU-8 interface, and second, when the probe is incident from the air, on the gold/air interface. Figure 5.11 summarizes the results of this study.

The black curve in Fig. 5.11 is obtained by pumping (7 mJ/cm^2) on the grating and probing the gold/SU-8 interface, at the location of the hot spot at the apex of the taper (see inset (a)). Naturally, the amplitude is significant due to SPP focusing. Next, the red curve is obtained when probing the middle of the taper (at 4 μm distance from the grating), as sketched in the inset (b). In this case, the maximum of the recorded signal, which represents the electron temperature variations due to the absorbed plasmons at *this* location of the structure, is about 6 times smaller than at the position of the hot spot. Finally, the blue curve is measured by probing the reflectivity change at a 4 μm distance from the grating,

but at the gold/air interface now. We detect a relative reflectivity change of an amplitude about 3 times lower than the one detected at the same distance but at the gold/SU-8 interface. The weak hot electron signal disappears completely after 2 ps. All this is consistent with the fact that the grating dominantly excites the SPP mode at the gold/SU-8 interface.

Thus, the nanofocusing is clearly attributed to an SPP that propagates at the high-index side of the gold film.

5.5.4 Plasmon to Hot electron conversion dynamics

5.5.4.1 Hot spot temporal evolution

We have demonstrated that it is possible to obtain a nano scale heat source in the plasmonic taper. In this section we study the relaxation dynamics of the hot electrons along the entire taper structure by performing pump-probe delay dependent reflectance snapshots.

For that purpose, we repeat the procedure described in Chapter 4, i.e., the SPP wavepacket is excited by the pump incident on the grating and probed for different pump-probe delays, and we visualize the induced electron temperature variations at different instants. The recorded snaphots, as well as the delay at which each frame has been taken are presented in Fig. 5.12.

Snapshots in Fig. 5.12 illustrates the process of the plasmon to hot electron energy conversion in time and space. In particular, in a time scale of ~ 400 fs, we observe an increase of reflectivity variations in the grating area together with a heating of longitudinal edges of the taper. For delays in the range of $500 - 800$ fs we notice an accumulation of the energy at the taper apex, the hottest spot being observed between 800 fs – 1 ps. Finally after 1 ps the hot electron relaxation with the lattice takes place. After 1.8 ps, delay corresponding to the last measured frame, the electrons are still hotter than the lattice.

In comparison with the SPP and the hot electron dynamics observed with the grating structure in the previous chapter, (for which the hot electrons are thermalized with the lattice after ≈ 1.2 ps), the hot electrons in the taper apex are still out of the equilibrium at much larger time scales, even after 3 ps (see Fig. 5.11 black curve). This provides direct evidence that we are facing a much larger electronic temperature in the region of SPP focusing. Thus, the more

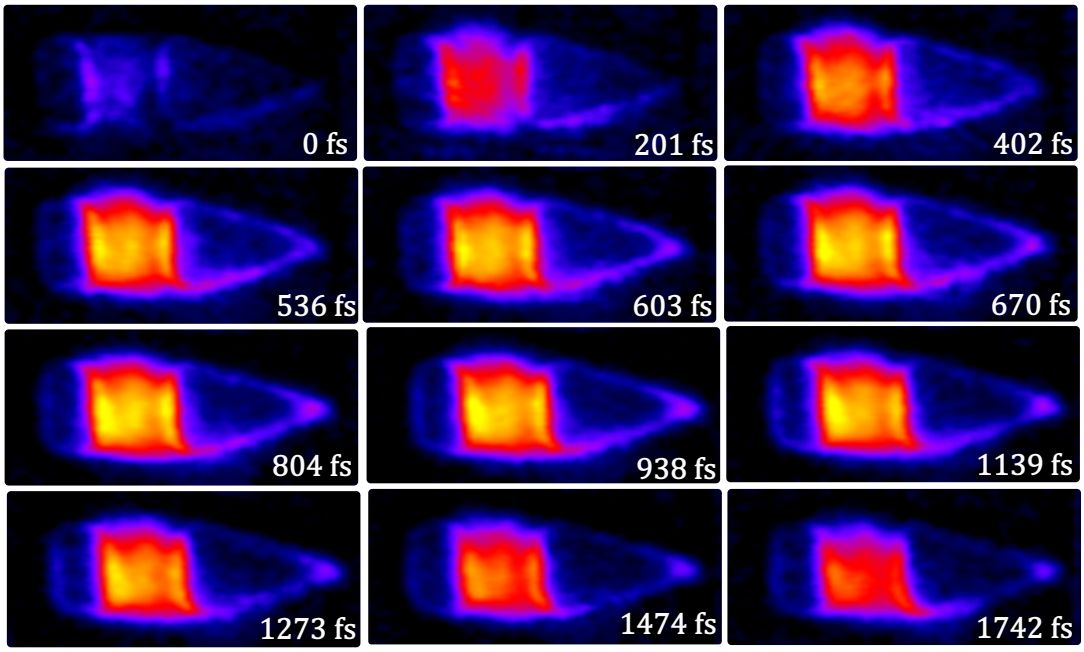

Figure 5.12: *Consecutive reflectance snapshots of the hot electron trace left by propagating SPP along the taper structure, describing the process of the plasmon to hot electron conversion in time and space. The pump-probe delay at which each frame has been taken is indicated in the images. The scan area is* $16 \times 7\,\mu\mathrm{m}^2$.

energy injected into the electron gas, the slower is the system and the longer is the process of electron-phonon relaxation.

For a better interpretation of the information presented in Fig. 5.12 and to obtain a better understanding of what happens with the hot electrons while the plasmon approaches the taper apex, we have extracted from Fig. 5.12, reflectance variation at the upper boudary of the taper (see the white arrow in Fig. 5.13) from the frames (some of them not included in Fig. 5.12) for all temporal delays, an average profile of the border of the taper. The reflectance average lines are organized to form a single map in space and time, as shown in Fig. 5.13. It becomes easier to see that along the taper, the appearance of the heating takes place at about 500 fs, whereas the appearance is additionally delayed by about 300 – 400 fs at the tip apex. While approaching the tip apex the heating process slows down and the maximum is achieved at about 800 – 900 fs.

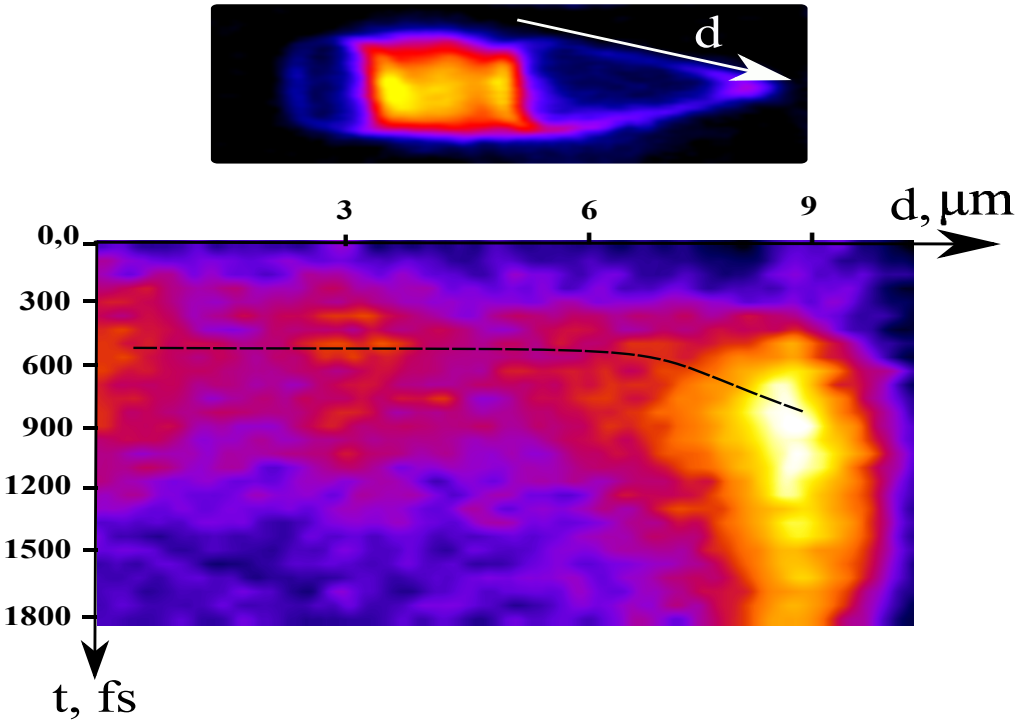

Figure 5.13: *Visualization of the plasmon-to-hot-electron conversion process in time and space. The upper inset shows the spatial location where the reflectance change is observed. The color map reveals that along the taper the maximum of the heating signal takes place at about* 500 fs*, whereas as one approaches the apex an additional delay of about* 300 fs *is observed. The black curve underlines the averaged delay of the maximal heating as a function of the position d along the upper boundary of the taper*

We will study this effect more carefully in the following section by performing point time-resolved measurements along the taper.

5.5.4.2 Pump-probe along taper

For a more precise measurement of the increase in propagation time of SPPs as they approach the apex, we performed time-resolved measurements at several different positions along the taper, see the green dots in the upper panel of Fig. 5.14. In Fig. 5.14(a), we show the $\Delta R/R$ signals as a function of the pump-probe delay. The normalized plots are shown in Fig. 5.14(b).

Clearly, we observe that not only the magnitude of the signal increases as we approach the tip apex, but also the delay at which the $\Delta R/R$ signals reach their maximal increases. Specifically, for the signals recorded at 3.5, 4.5, 5.5

and 6.5 μm separation distances from the grating, the electron temperature is established after 500−600 fs, whereas at 7.5 μm and 8 μm, the maxima are reached for a delay of 850 fs – 1 ps. The effect is stringent for the normalized curves. We should again recall that the region being probed has a 800-nm spatial extent, and that the $\Delta R/R$ signals thus represent a spatial average over the focusing area.

Generally, the rising part of the $\Delta R/R$ signal relates to the instantaneous nonthermal (non-Fermi, see Fig. 1.8) electron distribution change (taking place on a scale of 10 – 20 fs) and the corresponding thermalized hot electron (or Fermi) distribution change (~ 500 fs – 1 ps) [68]. Thus, the measured delayed $\Delta R/R$-rise means that the dynamics and the involved time scales of the constituent processes (creation of the nonthermal electrons and their thermalization to a Fermi distribution) are different in the hot spot comparing to processes along the taper. As described by Del Fatti *et al.* for larger energy injection into the electron gas, the induced large smearing of the electron distribution around Fermi level E_F significantly weakens the electron electron-scattering blocking effect. Thus, a faster electron internal thermalization was calculated and in very good agreement with the experimental results previously reported for gold [71]. However, our measurements reveal a slower internal electron thermalization at the tip apex, although the deposited plasmon energy is considerably larger at this location.

We do not exactly know the physical origin of the longer rising time observed at the tip apex. Indeed, a first possibility could be a slowdown of the SPP at the apex. In this hypothesis, the electron-hole pairs are generated with a temporal delay and the relaxation in the electron bath is also delayed, giving the observed increase of the rising time. Since a significant slowdown occurs for taper widths smaller than 20 nm, we infer that significant velocity decreases mainly occur on a 30 nm distance at the tip apex. Thus a delay of t = 300 fs on such a small propagation distance corresponds to a group velocity reduction of ~ 1000. A second possibility would be a modification of the internal electronic thermalization process itself due to confinement at the tip apex. However, internal electron thermalization dynamics is affected for metal volumes bellow 10nm and leads to a faster internal equilibrium. Thus, they may not stand at the origin of the longer rising time observed at the tip apex.

Most probably, the SPP slowdown overlaps in time with electron thermal-

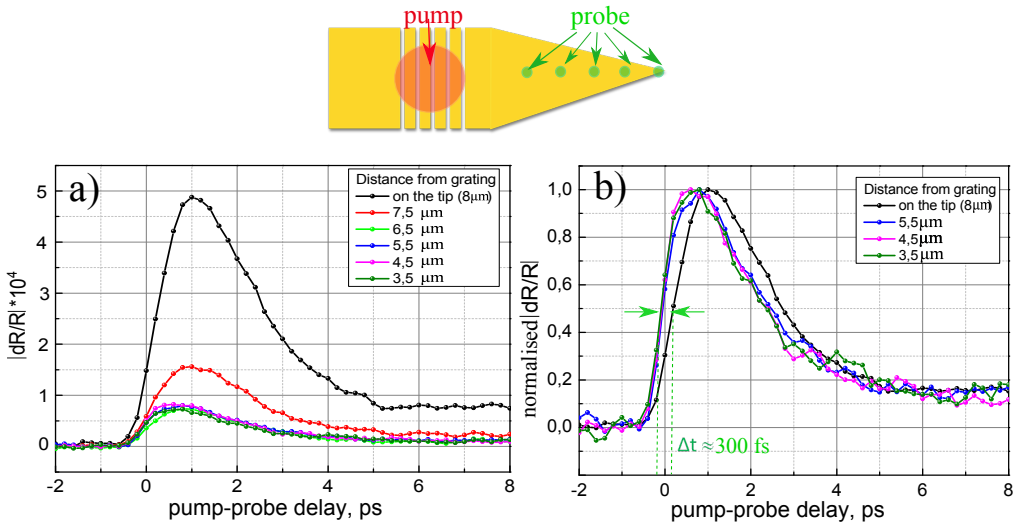

Figure 5.14: *Point time-resolved measurements along the taper: upper panel: scheme of the performed experiment;* ***(a)*** $\Delta R/R$ *as a function of the pump-probe delay, for a probe fixed respectively at the tip apex (i.e.,* $8\,\mu$m *from grating),* 7.5, 6.5, 5.5, 4.5 *and* $3.5\,\mu$m *separation from grating.* ***(b)*** *The normalized* $\Delta R/R$ *as a function of the pump-probe delay from* ***(a)*** *for a probe fixed respectively at the tip apex,* 5.5, 4.5 *and* $3.5\,\mu$m *separation from grating.*

ization at certain time-scales, and it is difficult to estimate quantitatively their respective contributions in delaying the electron thermalization.

5.5.4.3 Tunneling energy transfer between the tip and film

Finally, we have studied the possibility of an energy transfer between the taper apex and the gold ribbon. The separation distance between the taper apex and ribbon varies between 10 and 60 nm. The energy transfer can take place through a SPP-mediated electromagnetic transfer between the SPP taper mode and the SPP modes of the ribbon.

To detect an eventual transfer, we employ the experimental configuration sketched in Fig. 5.6(a) and we image not only the taper structure, but also the adjacent gold ribbon. In Fig. 5.15, three consecutive snapshots of the SPP absorption and electron temperature variation along the taper structure separated by a 40 nm gap from a $20 \times 100\,\mu$m^2 gold ribbon are presented. The imaged area contains a part of the taper and $\approx 5\,\mu$m of Au film. The thermoreflectance maps are taken respectively at 1.3, 2, and 3.3 ps pump-probe delay. Whereas the hot

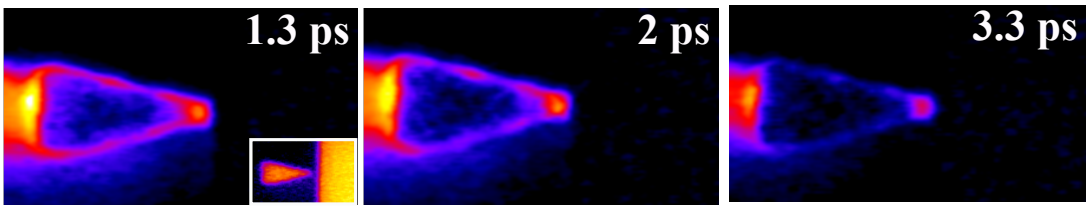

Figure 5.15: *Consecutive reflectance snapshots of the hot electron trace left by SPP in the structure. The latter is composed of the taper and a* $20 \times 100\,\mu\text{m}^2$ *gold ribbon, which are separated by a narrow* 40 nm *air gap (see the inset in the left image). No reflectance change is detected in the ribbon. The pump-probe delay of each frame is indicated in the images. The scan area is* $16 \times 7\,\mu\text{m}^2$*. The left inset represents a reflectivity image of the region being imaged, in the absence of any pump-induced excitation.*

electron temperature variation, at the tip apex, is rather high around 1.3 ps, at later delays electron-phonon generation and subsequent relaxation already starts. The measured images give no indication of any detectable energy transfer neither at short time scales (i.e., electron heating, the image at 1.3 ps), nor at longer temporal scales (phonon generation, i.e., image at 3.3 ps).

The slow hot electron relaxation in the region of the hot spot is also remarkable, which is clearly intense enough even after 3.3 ps temporal delay. The second observation is the high degree of confinement of the hot spot in time.

5.6 Conclusion

To conclude, we have advanced the comprehension of the mechanism regarding guiding and nanofocusing in complex SPP nanofocusing taper-geometry, as well as shown how such nanofocusing can be achieved. By employing femtoseconds pulsed excitation we are able to generate a local heat source at picosecond time scale near the apex of the plasmonic tip.

The demonstrated taper-structure couples far-field light from an external source and guides it to the tip-apex, together with an energy concentration, mode localization, and increase in the dissipated losses as heat. The thermal profile recorded at time scales when the energy is stored in the hot electron gas, may significantly differ from the thermal profile at steady state. Thus, at steady state the thermal profile of the plasmonic device is considerably broadened compared

with the dimensions of the heat source due to the electron diffusion and phonon transport in the metal. Thus, the plasmonic taper can be used for the generation of an on-chip heat source with nanometric dimensions under a femtosecond pulsed illumination.

Through thermoreflectance imaging, as well as through point-measurements we observed a longer electron temperature rising time at the taper apex. This effect is attributed to a reduction of the SPP group velocity. However, as we do not directly detect the SPP intensity, but through hot electrons, the detected effect may be caused by an interplay of v_g reduction and more complex nonthermal-electron associated processes.

Conclusion

In this work we measured and studied the heat dissipated by surface plasmons in plasmonic structures. We developed and employed femtosecond pump-probe thermoreflectance to detect the electronic temperature variations of the SPP-excited hot electron gas. The hot electrons dynamics inside metals is detected by the dielectric permittivity changes leading to reflectivity variations.

Thus, by probing the hot electron gas, we imaged the local heat source (caused by SPP dissipation) with a weak broadening thanks to our femtosecond time resolution. By imaging absorption around a nanoslit at the surface of metal film, we revealed an anomalous behavior. Absorption is actually remaining constant over a large range of several tens of wavelengths. In this area of constant absorption, the dissipated heat is weaker than the heat deposited by the plasmon launched at the surface. This phenomenon appears only for noble metals at near-infrared wavelengths ($\lambda > 800\,\mathrm{nm}$) was demonstrated to be an intrinsic property, which is likely to be observed for any sub-wavelength aperture geometries.

In a next step, we characterized qualitatively the hot electrons-mediated SPP signal and estimated the propagation length of the excited SPPs to be $L_{\mathrm{SPP}} = 28 \pm 3\,\mu\mathrm{m}$. From the spatio-temporal study of the launched SPP pulses and hot electron dynamics we have determined the thermal wave associated to SPP group velocity of $v_{\mathrm{g}} = (1.66 \pm 0.33) \times 10^8\,\mathrm{m/s}$.

Finally, we demonstrated generation of a sub-micrometer hot spot at picosecond time scale near the apex of a plasmonic nanofocusing taper. Through thermoreflectance imaging, as well as through point-measurements, we observed a longer electron temperature rising time at the taper apex. This effect is attributed both to a reduction of the SPP group velocity and to more complex nonthermal-electron associated processes.

There is much yet to be explored. In particular, a more detailed study, both experimental and theoretical, of the observed delayed hot electron generation at

the plasmon focusing tip is needed. In addition to these results, on-going work we are currently involved in concerns the quantitative transformation of $\Delta R/R$ values into variation of electronic temperature. Thus, a thermoreflectance map could be "rescaled" and presented in values of ΔT_e.

As a future perspective regarding the experimental set-up we wish to improve it in order that it corresponds better to our needs. In particular, we would like to enhance the probing spatial resolution. A solution would be the integration of an atomic force microscope (AFM) head on the inverted microscope (used in the experimental bench). In this way, probing with an AFM tip would make us capable of imaging electronic temperature variations in plasmonic devices with nanometrical spatial resolution.

Bibliography

[1] G. Baffou and R. Quidant, "Thermo-plasmonics: Using metallic nanostructures as nano-sources of heat," *Laser and Photonics Reviews*, vol. 7, no. 2, pp. 171–187, 2013.

[2] O. Lozan, M. Perrin, B. Ea-Kim, J. M. Rampnoux, S. Dilhaire, and P. Lalanne, "Anomalous light absorption around subwavelength apertures in metal films," *Physical Review Letters*, vol. 112, no. 19, 2014.

[3] B. M. `http://www.britishmuseum.org`.

[4] H. Raether, *Surface plasmons on smooth and rough surfaces and on gratings*. Berlin: Springer Verlag, 1988.

[5] J. Homola, "Surface plasmon resonance sensors for detection of chemical and biological species," *Chemical Reviews*, vol. 108, no. 2, pp. 462–493, 2008.

[6] K. R. Catchpole and A. Polman, "Plasmonic solar cells," *Optics Express*, vol. 16, no. 26, pp. 21793–21800, 2008.

[7] L. Novotny and B. Hecht, *Principles of Nano-Optics*. UK: Cambrigde University Press, 2006.

[8] S. Maier, *Plasmonics: Fundamentals and Applications*. New York: Springer, 2007.

[9] M. Brongersma and P. Kik, *Surface Plasmon Nanophotonics*. Springer, 2007.

[10] P. Drude, "Zur elektronentheorie der metalle," *Annalen der Physik*, vol. 306, no. 3, pp. 566–613, 1900.

[11] P. Drude, "Zur elektronentheorie der metalle; ii. teil. galvanomagnetische und thermomagnetische effecte," *Annalen der Physik*, vol. 308, no. 11, pp. 369–402, 1900.

[12] N. W. Ashcroft and N. D. Mermin, *Solid State Physics*. Saunders, 1976.

[13] H. Raether, *Excitation of Plasmons and Interband Transitions by Electrons*. Berlin: Springer, 1980.

[14] P. B. Johnson and R. W. Christy, "Optical constants of the noble metals," *Physical Review B*, vol. 6, no. 12, pp. 4370–4379, 1972.

[15] C. Sönnichsen, *Plasmons in metal nanostructures*. PhD thesis, Fakultät für Physik der Ludwig-Maximilians-Universität München, 2001.

[16] R. H. Ritchie, "Plasma losses by fast electrons in thin films," *Physical Review*, vol. 106, no. 5, pp. 874–881, 1957.

[17] C. J. Powell and J. B. Swan, "Origin of the characteristic electron energy losses in magnesium," *Physical Review*, vol. 116, no. 1, pp. 81–83, 1959.

[18] F. H. L. Koppens, D. E. Chang, and F. J. García De Abajo, "Graphene plasmonics: A platform for strong light-matter interactions," *Nano Letters*, vol. 11, no. 8, pp. 3370–3377, 2011.

[19] F. J. García de Abajo, "Graphene plasmonics: Challenges and opportunities," *ACS Photonics*, vol. 1, no. 3, pp. 135–152, 2014.

[20] T. Lewowski, "Photoelectron spectroscopy of thin discontinuous silver films deposited onto a sapphire substrate, near the percolation threshold," *Thin Solid Films*, vol. 259, no. 1, pp. 53–58, 1995.

[21] H. Wei and H. Eilers, "From silver nanoparticles to thin films: Evolution of microstructure and electrical conduction on glass substrates," *Journal of Physics and Chemistry of Solids*, vol. 70, no. 2, pp. 459–465, 2009.

[22] G. G. Nenninger, P. Tobiška, J. Homola, and S. S. Yee, "Long-range surface plasmons for high-resolution surface plasmon resonance sensors," *Sensors and Actuators, B: Chemical*, vol. 74, no. 1-3, pp. 145–151, 2001.

[23] P. Berini, R. Charbonneau, and N. Lahoud, "Long-range surface plasmons on ultrathin membranes," *Nano Letters*, vol. 7, no. 5, pp. 1376–1380, 2007.

[24] E. Kretschmann and H. Raether, "Radiative decay of nonradiative surface plasmons excited by light," *Z. Naturforsch*, vol. A, no. 23, pp. 2135–2136, 1968.

[25] A. Otto, "Excitation of nonradiative surface plasma waves in silver by the method of frustrated total reflection," *Zeitschrift für Physik*, vol. 216, no. 4, pp. 398–410, 1968.

[26] B. Liedberg, C. Nylander, and I. Lunström, "Surface plasmon resonance for gas detection and biosensing," *Sensors and Actuators*, vol. 4, no. C, pp. 299–304, 1983.

[27] R. J. Green, R. A. Frazier, K. M. Shakesheff, M. C. Davies, C. J. Roberts, and S. J. B. Tendler, "Surface plasmon resonance analysis of dynamic biological interactions with biomaterials," *Biomaterials*, vol. 21, no. 18, pp. 1823–1835, 2000.

[28] B. Hecht, H. Bielefeldt, L. Novotny, Y. Inouye, and D. W. Pohl, "Local excitation, scattering, and interference of surface plasmons," *Physical Review Letters*, vol. 77, no. 9, pp. 1889–1892, 1996.

[29] U. Kreibig and M. Vollmer, *Optical Properties of Metal Clusters*, vol. 25 of *Springer Series in Material Science*. Berlin: Springer, 1995.

[30] A. Bouhelier, G. Colas des Francs, and J. Grandidier, "Imaging surface plasmons," in *Plasmonics* (S. Enoch and N. Bonod, eds.), vol. 167, pp. 225–268, Springer Series in Optical Sciences, 2012.

[31] M. Specht, J. D. Pedarnig, W. M. Heckl, and T. W. Hänsch, "Scanning plasmon near-field microscope," *Physical Review Letters*, vol. 68, no. 4, pp. 476–479, 1992.

[32] M. Sandtke, R. J. P. Engelen, H. Schoenmaker, I. Attema, H. Dekker, I. Cerjak, J. P. Korterik, F. B. Segerink, and L. Kuipers, "Novel instrument for surface plasmon polariton tracking in space and time," *Review of Scientific Instruments*, vol. 79, no. 1, 2008.

[33] P. Dawson, F. De Fornel, and J. P. Goudonnet, "Imaging of surface plasmon propagation and edge interaction using a photon scanning tunneling microscope," *Physical Review Letters*, vol. 72, no. 18, pp. 2927–2930, 1994.

[34] V. S. Volkov, S. I. Bozhevolnyi, S. G. Rodrigo, L. Martín-Moreno, F. J. García-Vidal, E. Devaux, and T. W. Ebbesen, "Nanofocusing with channel plasmon polaritons," *Nano Letters*, vol. 9, no. 3, pp. 1278–1282, 2009.

[35] J. C. Weeber, M. U. González, A. L. Baudrion, and A. Dereux, "Surface plasmon routing along right angle bent metal strips," *Applied Physics Letters*, vol. 87, no. 22, pp. 1–3, 2005. Cited By :65.

[36] A. Bouhelier and G. P. Wiederrecht, "Surface plasmon rainbow jets," *Optics Letters*, vol. 30, no. 8, pp. 884–886, 2005.

[37] H. J. Simon and J. K. Guha, "Directional surface plasmon scattering from silver films," *Optics Communications*, vol. 18, no. 3, pp. 391–394, 1976.

[38] H. Ditlbacher, J. R. Krenn, G. Schider, A. Leitner, and F. R. Aussenegg, "Two-dimensional optics with surface plasmon polaritons," *Applied Physics Letters*, vol. 81, no. 10, pp. 1762–1764, 2002.

[39] Z. Wang, H. Wei, D. Pan, and H. Xu, "Controlling the radiation direction of propagating surface plasmons on silver nanowires," *Laser and Photonics Reviews*, vol. 8, no. 4, pp. 596–601, 2014.

[40] H. Ditlbacher, J. R. Krenn, N. Felidj, B. Lamprecht, G. Schider, M. Salerno, A. Leitner, and F. R. Aussenegg, "Fluorescence imaging of surface plasmon fields," *Applied Physics Letters*, vol. 80, no. 3, pp. 404–406, 2002.

[41] J. Grandidier, G. C. Des Francs, S. Massenot, A. Bouhelier, L. Markey, J. C. Weeber, C. Finot, and A. Dereux, "Gain-assisted propagation in a plasmonic waveguide at telecom wavelength," *Nano Letters*, vol. 9, no. 8, pp. 2935–2939, 2009.

[42] H. Wei, S. Zhang, X. Tian, and H. Xu, "Highly tunable propagating surface plasmons on supported silver nanowires," *Proceedings of the National Academy of Sciences of the United States of America*, vol. 110, no. 12, pp. 4494–4499, 2013. Cited By :23.

[43] J. J. Mock, D. R. Smith, and S. Schultz, "Local refractive index dependence of plasmon resonance spectra from individual nanoparticles," *Nano Letters*, vol. 3, no. 4, pp. 485–491, 2003.

[44] W. A. Murray and W. L. Barnes, "Plasmonic materials," *Advanced Materials*, vol. 19, no. 22, pp. 3771–3782, 2007.

[45] N. Yamamoto, K. Araya, and F. J. García de Abajo, "Photon emission from silver particles induced by a high-energy electron beam," *Physical Review B - Condensed Matter and Materials Physics*, vol. 64, no. 20, pp. 2054191–2054199, 2001.

[46] E. J. R. Vesseur, R. De Waele, M. Kuttge, and A. Polman, "Direct observation of plasmonic modes in au nanowires using high-resolution cathodoluminescence spectroscopy," *Nano Letters*, vol. 7, no. 9, pp. 2843–2846, 2007.

[47] J. S. Huang, J. Kern, P. Geisler, P. Weinmann, M. Kamp, A. Forchel, P. Biagioni, and B. Hecht, "Mode imaging and selection in strongly coupled nanoantennas," *Nano Letters*, vol. 10, no. 6, pp. 2105–2110, 2010.

[48] P. Ghenuche, S. Cherukulappurath, T. H. Taminiau, N. F. Van Hulst, and R. Quidant, "Spectroscopic mode mapping of resonant plasmon nanoantennas," *Physical Review Letters*, vol. 101, no. 11, 2008.

[49] C. Lemke, T. Leibner, S. Jauernik, A. Klick, J. Fiutowski, J. Kjelstrup-Hansen, H. G. Rubahn, and M. Bauer, "Mapping surface plasmon polariton propagation via counter-propagating light pulses," *Optics Express*, vol. 20, no. 12, pp. 12877–12884, 2012.

[50] A. Kubo, N. Pontius, and H. Petek, "Femtosecond microscopy of surface plasmon polariton wave packet evolution at the silver/vacuum interface," *Nano Letters*, vol. 7, no. 2, pp. 470–475, 2007.

[51] J. Nelayah, M. Kociak, O. Stéphan, F. J. G. De Abajo, M. Tencé, L. Henrard, D. Taverna, I. Pastoriza-Santos, L. M. Liz-Marzán, and C. Colliex, "Mapping surface plasmons on a single metallic nanoparticle," *Nature Physics*, vol. 3, no. 5, pp. 348–353, 2007.

[52] M. Bosman, V. J. Keast, M. Watanabe, A. I. Maaroof, and M. B. Cortie, "Mapping surface plasmons at the nanometre scale with an electron beam," *Nanotechnology*, vol. 18, no. 16, 2007.

[53] C. Hubert, A. Rumyantseva, G. Lerondel, J. Grand, S. Kostcheev, L. Billot, A. Vial, R. Bachelot, P. Royer, S. H. Chang, S. K. Gray, G. P. Wiederrecht, and G. C. Schatz, "Near-field photochemical imaging of noble metal nanostructures," *Nano Letters*, vol. 5, no. 4, pp. 615–619, 2005.

[54] J. Boneberg, J. König-Birk, H. J. Münzer, P. Leiderer, K. L. Shuford, and G. C. Schatz, "Optical near-fields of triangular nanostructures," *Applied Physics A: Materials Science and Processing*, vol. 89, no. 2, pp. 299–303, 2007.

[55] F. Ladstädter, U. Hohenester, P. Puschnig, and C. Ambrosch-Draxl, "First-principles calculation of hot-electron scattering in metals," *Physical Review B - Condensed Matter and Materials Physics*, vol. 70, no. 23, pp. 1–10, 2004.

[56] H. Ehrenreich and H. R. Philipp, "Optical properties of ag and cu," *Physical Review*, vol. 128, no. 4, pp. 1622–1629, 1962.

[57] D. E. Aspnes, E. Kinsbron, and D. D. Bacon, "Optical properties of au: Sample effects," *Physical Review B*, vol. 21, no. 8, pp. 3290–3299, 1980.

[58] B. R. Cooper, H. Ehrenreich, and H. R. Philipp, "Optical properties of noble metals. ii," *Physical Review*, vol. 138, no. 2A, pp. A494–A507, 1965.

[59] R. Rosei and D. W. Lynch, "Thermomodulation spectra of al, au, and cu," *Physical Review B*, vol. 5, no. 10, pp. 3883–3894, 1972.

[60] R. Rosei, F. Antonangeli, and U. M. Grassano, "d bands position and width in gold from very low temperature thermomodulation measurements," *Surface Science*, vol. 37, no. C, pp. 689–699, 1973.

[61] R. Rosei, "Temperature modulation of the optical transitions involving the fermi surface in ag: Theory," *Physical Review B*, vol. 10, no. 2, pp. 474–483, 1974.

[62] R. Rosei, C. H. Culp, and J. H. Weaver, "Temperature modulation of the optical transitions involving the fermi surface in ag: Experimental," *Physical Review B*, vol. 10, no. 2, pp. 484–489, 1974.

[63] M. Guerrisi, R. Rosei, and P. Winsemius, "Splitting of the interband absorption edge in au," *Physical Review B*, vol. 12, no. 2, pp. 557–563, 1975.

[64] M. Cardona, "Optical properties and band structure of srtio3 and batio3," *Physical Review*, vol. 140, no. 2A, pp. A651–A655, 1965.

[65] G. L. Eesley, "Observation of nonequilibrium electron heating in copper," *Physical Review Letters*, vol. 51, no. 23, pp. 2140–2143, 1983.

[66] R. W. Schoenlein, W. Z. Lin, J. G. Fujimoto, and G. L. Eesley, "Femtosecond studies of nonequilibrium electronic processes in metals," *Physical Review Letters*, vol. 58, no. 16, pp. 1680–1683, 1987.

[67] F. Wooten, *Optical properties of Solids*. New York: Academic Press, 1972.

[68] C. K. Sun, F. Vallée, L. H. Acioli, E. P. Ippen, and J. G. Fujimoto, "Femtosecond-tunable measurement of electron thermalization in gold," *Physical Review B*, vol. 50, no. 20, pp. 15337–15348, 1994.

[69] W. J. Scouler, "Temperature-modulated reflectance of gold from 2 to 10 ev," *Physical Review Letters*, vol. 18, no. 12, pp. 445–448, 1967.

[70] R. H. M. Groeneveld, R. Sprik, and A. Lagendijk, "Femtosecond spectroscopy of electron-electron and electron-phonon energy relaxation in ag and au," *Physical Review B*, vol. 51, no. 17, pp. 11433–11445, 1995.

[71] C. K. Sun, F. Vallée, L. Acioli, E. P. Ippen, and J. G. Fujimoto, "Femtosecond investigation of electron thermalization in gold," *Physical Review B*, vol. 48, no. 16, pp. 12365–12368, 1993.

[72] S. I. Anisimov, B. L. Kapeliovich, and P. T. L., "Electron emission from metal surfaces exposed to ultrashort laser pulses," *Zh. Eksp. Teor. Fiz*, vol. 66, pp. 776–781, 1974.

[73] D. E. Spence, P. N. Kean, and W. Sibbett, "60-fsec pulse generation from a self-mode-locked ti:sapphire laser," *Optics Letters*, vol. 16, no. 1, pp. 42–44, 1991. Opt. Lett.

[74] P. Antoine, A. L'Huillier, and M. Lewenstein, "Attosecond pulse trains using high-order harmonics," *Physical Review Letters*, vol. 77, no. 7, pp. 1234–1237, 1996.

[75] D. H. Sutter, G. Steinmeyer, L. Gallmann, N. Matuschek, F. Morier-Genoud, U. Keller, V. Scheuer, G. Angelow, and T. Tschudi, "Semiconductor saturable-absorber mirror assisted kerr-lens mode-locked ti:sapphire laser producing pulses in the two-cycle regime," *Optics Letters*, vol. 24, no. 9, pp. 631–633, 1999. Opt. Lett.

[76] S. Pedersen, J. L. Herek, and A. H. Zewail, "The validity of the 'diradical' hypothesis: Direct femtosecond studies of the transition-state structures," *Science*, vol. 266, no. 5189, pp. 1359–1364, 1994.

[77] E. P. Ippen and C. V. Shank, "Techniques for measurement," *Topics in Applied Physics*, vol. 18, 1977.

[78] G. Calbris, *Dynamique thermique et vibrationnelle de nanoparticules d'or et Au@SiO2 en régime femtoseconde, effet de la nanostructuration.* PhD thesis, Université Bordeaux I, 2010.

[79] S. D. Brorson, J. G. Fujimoto, and E. P. Ippen, "Femtosecond electronic heat-transport dynamics in thin gold films," *Physical Review Letters*, vol. 59, no. 17, pp. 1962–1965, 1987.

[80] W. Ho, "Single-molecule chemistry," *Journal of Chemical Physics*, vol. 117, no. 24, pp. 11033–11061, 2002.

[81] K. Konig, "Multiphoton microscopy in life sciences," *Journal of Microscopy*, vol. 200, no. 2, pp. 83–104, 2000.

[82] A. Volkmer, "Vibrational imaging and microspectroscopies based on coherent anti-stokes raman scattering microscopy," *Journal of Physics D: Applied Physics*, vol. 38, no. 5, pp. R59–R81, 2005.

[83] E. P. Ippen and C. V. Shank, *Ultrashort Light Pulses : Picosecond Techniques and Applications*. Springer, 1977.

[84] M. A. Van Dijk, A. L. Tchebotareva, M. Orrit, M. Lippitz, S. Berciaud, D. Lasne, L. Cognet, and B. Lounis, "Absorption and scattering microscopy of single metal nanoparticles," *Physical Chemistry Chemical Physics*, vol. 8, no. 30, pp. 3486–3495, 2006.

[85] P. E. Raad, P. Komarov, and M. G. Burzo, "Thermo-reflectance thermography for submicron temperature measurements," *Electronics Cooling*, vol. 14, 2008.

[86] `http://www.coherent.com/downloads/Mira900Brochure.pdf`.

[87] `http://www.coherent.com/downloads/RegA_9000_9050_DS.pdf`.

[88] `http://www.coherent.com/downloads/OPA9400_DS.pdf`.

[89] `http://www.thinksrs.com/products/SR810830.htm`.

[90] `http://search.newport.com/?q=*&x2=sku&q2XML350`.

[91] `http://www.newport.com/Fast-Steering-Mirrors/847119/1033/info.aspx`.

[92] T. W. Ebbesen, H. J. Lezec, H. F. Ghaemi, T. Thio, and P. A. Wolff, "Extraordinary optical transmission through sub-wavelenght hole arrays," *Nature*, vol. 391, no. 6668, pp. 667–669, 1998.

[93] H. A. Bethe, "Theory of diffraction by small holes," *Physical Review*, vol. 66, no. 7-8, pp. 163–182, 1944.

[94] C. Genet and T. W. Ebbesen, "Light in tiny holes," *Nature*, vol. 445, no. 7123, pp. 39–46, 2007.

[95] H. J. Levene, J. Korlach, S. W. Turner, M. Foquet, H. G. Craighead, and W. W. Webb, "Zero-mode waveguides for single-molecule analysis at high concentrations," *Science*, vol. 299, no. 5607, pp. 682–686, 2003.

[96] H. Rigneault, J. Capoulade, J. Dintinger, J. Wenger, N. Bonod, E. Popov, T. W. Ebbesen, and P. F. Lenne, "Enhancement of single-molecule fluorescence detection in subwavelength apertures," *Physical Review Letters*, vol. 95, no. 11, 2005.

[97] G. Zheng, X. Cui, and C. Yang, "Surface-wave-enabled darkfield aperture for background suppression during weak signal detection," *Proceedings of the National Academy of Sciences of the United States of America*, vol. 107, no. 20, pp. 9043–9048, 2010.

[98] F. J. García-Vidal, E. Moreno, J. A. Porto, and L. Martín-Moreno, "Transmission of light through a single rectangular hole," *Physical Review Letters*, vol. 95, no. 10, p. 103901, 2005. PRL.

[99] Y. Takakura, "Optical resonance in a narrow slit in a thick metallic screen," *Physical Review Letters*, vol. 86, no. 24, pp. 5601–5603, 2001. PRL.

[100] H. J. Lezec, A. Degiron, E. Devaux, R. A. Linke, L. Martin-Moreno, F. J. Garcia-Vidal, and T. W. Ebbesen, "Beaming light from a subwavelength aperture," *Science*, vol. 297, no. 5582, pp. 820–822, 2002.

[101] L. Yin, V. K. Vlasko-Vlasov, A. Rydh, J. Pearson, U. Welp, S. H. Chang, S. K. Gray, G. C. Schatz, D. B. Brown, and C. W. Kimball, "Surface plasmons at single nanoholes in au films," *Applied Physics Letters*, vol. 85, no. 3, pp. 467–469, 2004.

[102] M. Born and E. Wolf, *Principle of Optics*. New York: MacMillan, 6th ed., 1964.

[103] E. Silberstein, P. Lalanne, J. P. Hugonin, and Q. Cao, "Use of grating theories in integrated optics," *Journal of the Optical Society of America A: Optics and Image Science, and Vision*, vol. 18, no. 11, pp. 2865–2875, 2001.

[104] J. P. Hugonin and P. Lalanne, "Perfectly matched layers as nonlinear coordinate transforms: A generalized formalization," *Journal of the Optical Society of America A: Optics and Image Science, and Vision*, vol. 22, no. 9, pp. 1844–1849, 2005.

[105] M. Besbes, J. P. Hugonin, P. Lalanne, S. van Haver, O. T. A. Janssen, A. M. Nugrowati, M. Xu, S. F. Pereira, H. P. Urbach, A. S. van de Nes, P. Bienstman, G. Granet, A. Moreau, S. Helfert, M. Sukharev, T. Seideman, F. I. Baida, B. Guizal, and D. Van Labeke, "Numerical analysis of a slit-groove diffraction problem," *Journal of the European Optical Society*, vol. 2, 2007.

[106] M. G. Moharam, E. B. Grann, D. A. Pommet, and T. K. Gaylor, "Formulation for stable and efficient implementation of the rigorous coupled-wave analysis of binary gratings," *Journal of the Optical Society of America A: Optics and Image Science, and Vision*, vol. 12, no. 5, pp. 1068–1076, 1995.

[107] E. D. Palik, *Handbook of Optical Constants of Solids Part II.* New York,: Academic Press, 1985.

[108] L. Aigouy, P. Lalanne, J. P. Hugonin, G. Julié, V. Mathet, and M. Mortier, "Near-field analysis of surface waves launched at nanoslit apertures," *Physical Review Letters*, vol. 98, no. 15, 2007.

[109] H. Liu and P. Lalanne, "Comprehensive microscopic model of the extraordinary optical transmission," *Journal of the Optical Society of America A*, vol. 27, no. 12, pp. 2542–2550, 2010.

[110] P. Lalanne, J. P. Hugonin, H. T. Liu, and B. Wang, "A microscopic view of the electromagnetic properties of sub-λ metallic surfaces," *Surface Science Reports*, vol. 64, no. 10, pp. 453–469, 2009.

[111] F. Van Beijnum, C. Rétif, C. B. Smiet, H. Liu, P. Lalanne, and M. P. Van Exter, "Quasi-cylindrical wave contribution in experiments on extraordinary optical transmission," *Nature*, vol. 492, no. 7429, pp. 411–414, 2012.

[112] A. Yu Nikitin, S. G. Rodrigo, F. J. García-Vidal, and L. Martín-Moreno, "In the diffraction shadow: Norton waves versus surface plasmon polaritons in the optical region," *New Journal of Physics*, vol. 11, 2009.

[113] M. Van Exter and A. Lagendijk, "Ultrashort surface-plasmon and phonon dynamics," *Physical Review Letters*, vol. 60, no. 1, pp. 49–52, 1988.

[114] H. Inouye, K. Tanaka, I. Tanahashi, and K. Hirao, "Ultrafast dynamics of nonequilibrium electrons in a gold nanoparticle system," *Physical Review B - Condensed Matter and Materials Physics*, vol. 57, no. 18, pp. 11334–11340, 1998.

[115] J. Hohlfeld, S. S. Wellershoff, J. Güdde, U. Conrad, V. Jähnke, and E. Matthias, "Electron and lattice dynamics following optical excitation of metals," *Chemical Physics*, vol. 251, no. 1-3, pp. 237–258, 2000.

[116] B. Rethfeld, A. Kaiser, M. Vicanek, and G. Simon, "Ultrafast dynamics of nonequilibrium electrons in metals under femtosecond laser irradiation," *Physical Review B - Condensed Matter and Materials Physics*, vol. 65, no. 21, pp. 2143031–21430311, 2002.

[117] S. S. Wellershoff, J. Hohlfeld, J. Güdde, and E. Matthias, "The role of electron-phonon coupling in femtosecond laser damage of metals," *Applied Physics A: Materials Science and Processing*, vol. 69, no. 7, pp. S99–S107, 1999.

[118] T. Bian, B. Dong, and Y. Zhang, "Polarization independent extraordinary transmission through a subwavelength slit," *Optics Communications*, vol. 285, no. 6, pp. 1523–1527, 2012.

[119] Y. C. Jun, K. C. Y. Huang, and M. L. Brongersma, "Plasmonic beaming and active control over fluorescent emission," *Nature Communications*, vol. 2, no. 1, 2011.

[120] P. Lalanne, J. P. Hugonin, and J. C. Rodier, "Theory of surface plasmon generation at nanoslit apertures," *Physical Review Letters*, vol. 95, no. 26, 2005.

[121] H. W. Kihm, K. G. Lee, D. S. Kim, J. H. Kang, and Q. H. Park, "Control of surface plasmon generation efficiency by slit-width tuning," *Applied Physics Letters*, vol. 92, no. 5, 2008.

[122] M. S. Tame, K. R. McEnery, S. K. Özdemir, J. Lee, S. A. Maier, and M. S. Kim, "Quantum plasmonics," *Nature Physics*, vol. 9, no. 6, pp. 329–340, 2013.

[123] G. Baffou, R. Quidant, and F. J. García De Abajo, "Nanoscale control of optical heating in complex plasmonic systems," *ACS Nano*, vol. 4, no. 2, pp. 709–716, 2010.

[124] R. W. Wood, "On a remarkable case of uneven distribution of light in a diffraction grating spectrum," *Proceedings of the Physical Society of London*, vol. 18, no. 1, p. 269, 1902.

[125] L. Rayleigh, "Iii. note on the remarkable case of diffraction spectra described by prof. wood," *Philosophical Magazine Series 6*, vol. 14, no. 79, pp. 60–65, 1907.

[126] J. Strong, "Effect of evaporated films on energy distribution in grating spectra," *Physical Review*, vol. 49, no. 4, pp. 291–296, 1936.

[127] U. Fano, "The theory of anomalous diffraction gratings and of quasi-stationary waves on metallic surfaces (sommerfeld's waves)," *Journal of the Optical Society of America*, vol. 31, no. 3, pp. 213–222, 1941. J. Opt. Soc. Am.

[128] I. P. Radko, S. I. Bozhevolnyi, G. Brucoli, L. Martín-Moreno, F. J. García-Vidal, and A. Boltasseva, "Efficiency of local surface plasmon polariton excitation on ridges," *Physical Review B - Condensed Matter and Materials Physics*, vol. 78, no. 11, 2008.

[129] E. Devaux, T. W. Ebbesen, J. C. Weeber, and A. Dereux, "Launching and decoupling surface plasmons via micro-gratings," *Applied Physics Letters*, vol. 83, no. 24, pp. 4936–4938, 2003.

[130] H. L. Offerhaus, B. Van Den Bergen, M. Escalante, F. B. Segerink, J. P. Korterik, and N. F. Van Hulst, "Creating focused plasmons by noncollinear phasematching on functional gratings," *Nano Letters*, vol. 5, no. 11, pp. 2144–2148, 2005.

[131] Y. Y. Teng and E. A. Stern, "Plasma radiation from metal grating surfaces," *Physical Review Letters*, vol. 19, no. 9, pp. 511–514, 1967.

[132] S. Park, G. Lee, S. H. Song, C. H. Oh, and P. S. Kim, "Resonant coupling of surface plasmons to radiation modes by use of dielectric gratings," *Optics Letters*, vol. 28, no. 20, pp. 1870–1872, 2003.

[133] J. Moreland, A. Adams, and P. K. Hansma, "Efficiency of light emission from surface plasmons," *Physical Review B*, vol. 25, no. 4, pp. 2297–2300, 1982.

[134] A. Giannattasio, S. Wedge, and W. L. Barnes, "Role of surface profiles in surface plasmon-polariton-mediated emission of light through a thin metal film," *Journal of Modern Optics*, vol. 53, no. 4, pp. 429–436, 2006.

[135] M. Kuttge, E. J. R. Vesseur, J. Verhoeven, H. J. Lezec, H. A. Atwater, and A. Polman, "Loss mechanisms of surface plasmon polaritons on gold probed by cathodoluminescence imaging spectroscopy," *Applied Physics Letters*, vol. 93, no. 11, 2008.

[136] V. V. Temnov, U. Woggon, J. Dintinger, E. Devaux, and T. W. Ebbesen, "Surface plasmon interferometry: Measuring group velocity of surface plasmons," *Optics Letters*, vol. 32, no. 10, pp. 1235–1237, 2007.

[137] D. M. Koller, A. Hohenau, H. Ditlbacher, N. Galler, F. Reil, F. R. Aussenegg, A. Leitner, E. J. W. List, and J. R. Krenn, "Organic plasmon-emitting diode," *Nature Photonics*, vol. 2, no. 11, pp. 684–687, 2008.

[138] J. A. Schuller, E. S. Barnard, W. Cai, Y. C. Jun, J. S. White, and M. L. Brongersma, "Plasmonics for extreme light concentration and manipulation," *Nature Materials*, vol. 9, no. 3, pp. 193–204, 2010.

[139] D. K. Gramotnev and S. I. Bozhevolnyi, "Plasmonics beyond the diffraction limit," *Nature Photonics*, vol. 4, no. 2, pp. 83–91, 2010.

[140] L. Novotny and N. Van Hulst, "Antennas for light," *Nature Photonics*, vol. 5, no. 2, pp. 83–90, 2011.

[141] L. Novotny, R. X. Bian, and X. Sunney Xie, "Theory of nanometric optical tweezers," *Physical Review Letters*, vol. 79, no. 4, pp. 645–648, 1997.

[142] P. Verma, T. Ichimura, T. A. Yano, Y. Saito, and S. Kawata, "Nano-imaging through tip-enhanced raman spectroscopy: Stepping beyond the classical limits," *Laser and Photonics Reviews*, vol. 4, no. 4, pp. 548–561, 2010.

[143] K. V. Nerkararyan, "Superfocusing of a surface polariton in a wedge-like structure," *Physics Letters, Section A: General, Atomic and Solid State Physics*, vol. 237, no. 1-2, pp. 103–105, 1997.

[144] M. I. Stockman, "Nanofocusing of optical energy in tapered plasmonic waveguides," *Physical Review Letters*, vol. 93, no. 13, pp. 137404–1–137404–4, 2004.

[145] D. K. Gramotnev, "Adiabatic nanofocusing of plasmons by sharp metallic grooves: Geometrical optics approach," *Journal of Applied Physics*, vol. 98, no. 10, 2005.

[146] S. Berweger, J. M. Atkin, R. L. Olmon, and M. B. Raschke, "Light on the tip of a needle: Plasmonic nanofocusing for spectroscopy on the nanoscale," *Journal of Physical Chemistry Letters*, vol. 3, no. 7, pp. 945–952, 2012.

[147] D. K. Gramotnev and S. I. Bozhevolnyi, "Nanofocusing of electromagnetic radiation," *Nature Photonics*, vol. 8, no. 1, pp. 13–22, 2014.

[148] K. Li, M. I. Stockman, and D. J. Bergman, "Self-similar chain of metal nanospheres as an efficient nanolens," *Physical Review Letters*, vol. 91, no. 22, pp. 227402/1–227402/4, 2003.

[149] A. J. Babadjanyan, N. L. Margaryan, and K. V. Nerkararyan, "Superfocusing of surface polaritons in the conical structure," *Journal of Applied Physics*, vol. 87, no. 8, pp. 3785–3788, 2000.

[150] D. K. Gramotnev and M. W. Vogel, "Ultimate capabilities of sharp metal tips for plasmon nanofocusing, near-field trapping and sensing," *Physics Letters, Section A: General, Atomic and Solid State Physics*, vol. 375, no. 39, pp. 3464–3468, 2011.

[151] E. Verhagen, A. Polman, and L. Kuipers, "Nanofocusing in laterally tapered plasmonic waveguides," *Optics Express*, vol. 16, no. 1, pp. 45–57, 2008.

[152] E. Verhagen, M. Spasenović, A. Polman, and L. Kuipers, "Nanowire plasmon excitation by adiabatic mode transformation," *Physical Review Letters*, vol. 102, no. 20, 2009.

[153] A. Aubry, D. Y. Lei, A. I. Fernández-Domínguez, Y. Sonnefraud, S. A. Maier, and J. B. Pendry, "Plasmonic light-harvesting devices over the whole visible spectrum," *Nano Letters*, vol. 10, no. 7, pp. 2574–2579, 2010.

[154] D. R. Mason, D. K. Gramotnev, and K. S. Kim, "Plasmon nanofocusing in a dielectric hemisphere covered in tapered metal film," *Optics Express*, vol. 20, no. 12, pp. 12866–12876, 2012.

[155] K. C. Vernon, D. K. Gramotnev, and D. F. P. Pile, "Adiabatic nanofocusing of plasmons by a sharp metal wedge on a dielectric substrate," *Journal of Applied Physics*, vol. 101, no. 10, 2007.

[156] D. F. P. Pile and D. K. Gramotnev, "Adiabatic and nonadiabatic nanofocusing of plasmons by tapered gap plasmon waveguides," *Applied Physics Letters*, vol. 89, no. 4, 2006.

[157] T. Sondergaard, S. I. Bozhevolnyi, J. Beermann, S. M. Novikov, E. Devaux, and T. W. Ebbesen, "Resonant plasmon nanofocusing by closed tapered gaps," *Nano Letters*, vol. 10, no. 1, pp. 291–295, 2010.

[158] A. I. Fernández-Domínguez, S. A. Maier, and J. B. Pendry, "Collection and concentration of light by touching spheres: A transformation optics approach," *Physical Review Letters*, vol. 105, no. 26, 2010.

[159] E. Verhagen, L. Kuipers, and A. Polman, "Plasmonic nanofocusing in a dielectric wedge," *Nano Letters*, vol. 10, no. 9, pp. 3665–3669, 2010.

[160] V. Kravtsov, J. M. Atkin, and M. B. Raschke, "Group delay and dispersion in adiabatic plasmonic nanofocusing," *Optics Letters*, vol. 38, no. 8, pp. 1322–1324, 2013.

[161] T. Sondergaard, S. M. Novikov, T. Holmgaard, R. L. Eriksen, J. Beermann, Z. Han, K. Pedersen, and S. I. Bozhevolnyi, "Plasmonic black gold by adiabatic nanofocusing and absorption of light in ultra-sharp convex grooves," *Nature Communications*, vol. 3, 2012.

[162] M. W. Vogel and D. K. Gramotnev, "Optimization of plasmon nanofocusing in tapered metal rods," *Journal of Nanophotonics*, vol. 2, no. 1, 2008.

[163] J. J. Burke, G. I. Stegeman, and T. Tamir, "Surface-polariton-like waves guided by thin, lossy metal films," *Physical Review B*, vol. 33, no. 8, pp. 5186–5201, 1986.

[164] R. Zia, M. D. Selker, and M. L. Brongersma, "Leaky and bound modes of surface plasmon waveguides," *Physical Review B - Condensed Matter and Materials Physics*, vol. 71, no. 16, 2005.

[165] J. C. Weeber, J. R. Krenn, A. Dereux, B. Lamprecht, Y. Lacroute, and J. P. Goudonnet, "Near-field observation of surface plasmon polariton propagation on thin metal stripes," *Physical Review B - Condensed Matter and Materials Physics*, vol. 64, no. 4, pp. 454111–454119, 2001.

[166] L. Yin, V. K. Vlasko-Vlasov, J. Pearson, J. M. Hiller, J. Hua, U. Welp, D. E. Brown, and C. W. Kimball, "Subwavelength focusing and guiding of surface plasmons," *Nano Letters*, vol. 5, no. 7, pp. 1399–1402, 2005.

[167] E. Verhagen, L. Kuipers, and A. Polman, "Enhanced nonlinear optical effects with a tapered plasmonic waveguide," *Nano Letters*, vol. 7, no. 2, pp. 334–337, 2007.